X-RAY INDUCED PHOTOREDUCTION OF REDOX ACTIVE METAL IONS

A Thesis Submitted to the College of
Graduate and Postdoctoral Studies
In Partial Fulfillment of the Requirements
For the Degree of Doctor of Philosophy
In the Department of Geological Sciences
University of Saskatchewan
Saskatoon

By
KURT HENRY NIENABER

PERMISSION TO USE STATEMENT

In presenting this thesis in partial fulfillment of the requirements for a postgraduate degree from the University of Saskatchewan, I agree that the Libraries of this University may make it freely available for inspection. I further agree that permission for copying of this thesis in any manner, in whole or in part, for scholarly purposes may be granted by the professor or professors who supervised my thesis work or, in their absence, by the Head of the Department or the Dean of the College in which my thesis work was done. It is understood that any copying or publication or use of this thesis or parts thereof for financial gain shall not be allowed without my written permission. It is also understood that due recognition shall be given to me and to the University of Saskatchewan in any scholarly use which may be made of any material in my thesis.

Requests for permission to copy or to make other use of material in this thesis in whole or part should be addressed to:

Chair of the Geological Sciences Graduate Program

Geology Building

University of Saskatchewan

114 Science Place

Saskatoon, Saskatchewan S7N 5E2 Canada

OR

Dean
College of Graduate and Postdoctoral Studies
University of Saskatchewan
116 Thorvaldson Building, 110 Science Place
Saskatoon, Saskatchewan S7N 5C9 Canada

ABSTRACT

The use of synchrotron light sources has provided insights into structure, function, and mechanism of numerous proteins and enzymes. The fields of macromolecular crystallography and (MX) X-ray absorption spectroscopy (XAS) in particular have developed and grown with the use of synchrotrons, and cryoprotection has been an invaluable tool in making advances in these fields. Cryoprotectants have been employed to mitigate damage to biological samples caused by ice crystal formation during the flash cooling process. In addition, cryoprotectants are useful by allowing cryogenic temperatures to be utilized thereby reducing thermal vibrations in XAS experiments, and thermal stress on crystals used in MX experiments.

X-ray induced photochemistry is an increasingly encountered problem for XAS experiments given the use of powerful synchrotron light sources with increased photon flux. As photon flux has increased, there has been a corresponding increase in X-ray induced photoxidation and photoreduction artifacts observed in XAS experiments. Increases in flux density have also been shown to have a negative impact on active site structure determination in MX experiments.

Initial XAS studies of the prion protein (PrP) octarepeat region (OR) with Cu(II) revealed changes in the near edge region of the X-ray absorption spectra. After as little as one sweep of OR peptide bound to Cu(II), changes in the near edge region of the spectrum showed the loss of Cu(II) and an increase of Cu(I). Analysis revealed the complete loss of Cu(II) in situ and formation of Cu(I) bound to the PrP OR upon longer exposure to X-rays. To examine this phenomenon, samples of 2 mM CuCl2 with various cryoprotectants commonly used in XAS and protein crystal experiments were used in order to delineate the cause of the observed photoreduction.

The preliminary result indicated that glycerol was the causative agent in exacerbating the X-ray induced photo-reduction. A series of experiments was then designed to examine the

effects of glycerol concentration, copper concentration, and flux density on photoreduction rates. Results of these experiments show a linear relationship between the rate of photo-reduction and the X-ray flux density.

Having observed photoreduction in aqueous copper samples, experiments were designed and carried out to exploit this phenomenon to produce chemically interesting mercury species. Given the previously observed relative stability of mercury at lower flux density values, the creation of Hg(0) species proved intriguing and relatively simple compared to other methodologies.

Reports of peripheral sources of electrons contributing to photoreduction in experiments proved an intriguing addition to the photoreduction studies reported herein. Having studied photoreduction exacerbated by common cryoprotectants, studies were carried out with additional sources of electrons to observe any contributions made to photoreduction, including those present in common buffers used in both crystallographic and X-ray absorption spectroscopy experiments.

Following examination of the increase in the rate of photoreduction with the presence of common cryoprotectants, experiments were designed and carried out to ameliorate the effects of photoreduction. Ketone groups have been long known to be excellent scavengers of free radicals and were examined to observe their presumptive protective effect on X-ray induced photoreduction.

ACKNOWLEDGEMENTS

The completion of this thesis could not have happened without the support of numerous people. I would like to thank my supervisor Dr. Graham George, Dr. Ingrid Pickering, the members of my committee, and the Department of Geological Sciences.

I would also like to thank my fellow lab members, past and present, for their support, experimental assistance, and camaraderie. Dr. Julien Cotelesage, Dr. Jake Pushie, and Dr. Susan Nezhati were all integral to my success in this endeavor. The rest of my fellow grad students have made this journey fun and have helped me immensely in completing this dissertation.

Data collected in this thesis were collected at the Stanford Synchrotron Radiation Lightsource. A special thanks to Drs. Matt Latimer and Erik Nelson. Complete facility acknowledgements are included in the individual chapters.

I would like to acknowledge the support I received from the Gene Expression and Mapping Using Synchrotron Light (GEMS) Research Group, including a special thank you to Dr. Helen Nichol for her support. I would also like to acknowledge the support of the Canadian Institutes of Health Research – Training Grant in Health Research Using Synchrotron Techniques (CIHR-THRUST).

I would like to thank my amazing family and dear friends. I would not be here without you.

DEDICATION

I dedicate my dissertation to all those I've lost, but more importantly, to those I've gained completing this work. I never could have accomplished this without the support of my incredible wife and kids. I love you all so much. Big one squish.

TABLE OF CONTENTS

LIST OF TABLES

LIST OF FIGURES

LIST OF ABBREVIATIONS

°C	degrees Celsius
µM	micromolar
Å	angstrom
APS	Advanced Photon Source
Ar	argon
As	arsenic
ATP	adenosine triphosphate
Au	gold
C	Coulomb
Ca	calcium
CAD	Canadian dollar
Cα	alpha-carbon
$CH_3O•$	methoxy radical
CH_3OH	methanol
Cl	chlorine
cm	centimetres
Co	cobalt
COSMO	Conductor-like Screening Model
CSM	continuum solvation model
Cu	copper
$•CH_2OH$	methylene hydroxide radical
DTPA	diethylenetriaminepentaacetic acid
e^-	electron
e_{aq}^-	solvated electron
EDTA	ethylenediaminetetraacetic acid
EPR	electron paramagnetic resonance
eV	electron Volt
EXAFS	Extended X-ray Absorption Fine Structure
F	fluorine
Fe	iron

FEL	free-electron laser
fs	femtosecond
g	gram
GGA	generalized gradient approximation
Ge	germanium
H^+	hydrogen ion
H_2O	water
H_2O^+	photoexcited water
H_2O_2	hydrogen peroxide
H_3O^+	hydronium ion
He	helium
Hg	mercury
HO	hydroxide
HO^-	hydroxy anion
hr	hour
K	kelvin
k_{eff}	effective rate constant
kJ	kilojoule
Kr	krypton
LCLS	Linac Coherent Light Source
LDA	local density approximation
Mg	magnesium
MGy	megagray
min	minutes
mm	millimetre
mM	millimolar
Mo	molybdenum
mol	moles
MX	macromolecular crystallography
N	nitrogen
NH_3	ammonia

O	oxygen
PCA	principle component analysis
PBE	Perdew-Burke-Ernzerhof
PEG	polyethylene glycol
Pt	platinum
RSH	thiol
s	second
Si	silicon
SSRL	Stanford Synchrotron Radiation Lightsource
V	vanadium
v/v	volume/volume percent
XAS	X-ray absorption spectroscopy
Xe	xenon

1. Introduction

1.1 Photochemistry

Photochemistry is the area of chemistry studying the effects of light. Usually light is taken to mean electromagnetic radiation in the visible and ultraviolet, approximately 700 to 100 nm. A distinction can be made between photophysical processes and photochemical changes. Photophysical processes lead through changes in energy and electronic structure to a regeneration of the same molecular species that existed prior to photon absorption.[1] Photochemical changes produce new molecular entities. Both processes are important to consider with regards to photodamage, as photophysical events can be observed during X-ray absorption spectroscopy (XAS) experiments, and photochemical changes can often be overlooked, especially in the field of macromolecular crystallography (MX).[2, 3] Herein, the focus of this thesis is on X-rays, and specifically the photochemistry involved with the exposure of aqueous samples to X-rays.

Photochemical reactions feature absorption of a photon by a molecule leading to an electronically excited state, which is the starting point for reaction steps going forward. This is a molecular species whose electrons are not in the lowest energy configuration. In this electronically excited state, an electron will occupy a higher-energy orbital and the overall energy is higher for the molecule. Electronically excited states can be produced using a variety of methods, including ionizing radiation, electric discharge, or chemical reaction. However, the most convenient and commonplace method is via absorption of a visible light or ultraviolet photon. Electromagnetic radiation at these wavelengths, and lower like X-rays, has enough energy to convert a ground state molecule or atom into a higher energy state.

There are two “laws” of photochemistry which guide the principles of investigation into the subject. The first is the Grotthuss-Draper law that states the amount of chemical action induced by light is proportional to the amount of light absorbed. The second is the Stark-Einstein law, which states that the number of primary processes produced is equal to the number of photons absorbed. Photochemistry, then, is concerned with reactions of electronically excited states and the corresponding ground states that affect the nature of photochemical reactions. The energy difference between excited and ground states opens a wide range of reactions based on thermodynamic grounds.[4]

One further difference between ground and excited states, especially for chemical reactions, is the electron-donating and electron-accepting abilities of these states. The excited state molecules are better at both acceptance and donation of an electron.[1] A measure of the electron-donating ability of a species is its ionization potential, the minimum amount of energy required to remove an electron completely from the species. Because of the difference in electron-donor and electron-acceptor properties, excited states have different redox properties from their related ground states.

In examining whether a photochemical reaction will occur, it is important to consider the Grotthuss-Draper law and specifically whether a photon will have sufficient energy to penetrate a sample in order to be absorbed. Lower energy photons do not pass through samples as easily as high energy photons. Interestingly, this means that higher energy photons do not deposit as much energy into a sample, meaning the absorbed dose is reduced, as lower energy photons.

As opposed to a thermal reaction, where heat is applied in an indiscriminate manner to all the constituent substrates; light, in a photochemical reaction, can be supplied selectively to just one species in the mixture. This is accomplished by choosing the appropriate exciting wavelength based on the absorption characteristics of all the species present. It is also important to note that, unlike thermal reactions, photochemical reactions can be conducted at lower temperatures, even nearing absolute zero.

Radiation chemistry is the chemistry of the effects of high energy particles and radiation, including radioactive particles and photons generated from synchrotron sources. In 1895, Roentgen reported exposure of a covered photographic plate to invisible, highly penetrative rays, X-rays.[5] Later in that same year, Becquerel conducted a series of experiments based on Roentgen's discovery, to discover possible natural sources of these penetrating rays. He reported, in 1896, that a photographic plate was fogged by the rays from uranium mineral pitchblende, just like X-rays.[6] Not long after, in 1898, the Curies were able to report the isolation of polonium and radium, both possessing the same characteristics of the uranium mineral, both being major constituents of the mineral.[7] The two biggest differences between radiation chemistry and photochemistry are; in photochemical reactions, only certain molecules and atoms may be affected by light of a particular wavelength, whereas all parts of

any molecular are susceptible to the effect of high energy radiation. Furthermore, primary ionization characteristics of radiation chemistry produce chemical effects essentially different from those products in photochemical processes.[8]

The initial physical event of radiation chemistry or photochemistry processes is the transfer of energy causing ionizations or excitations in water molecules. In biological systems, energy transfer to water molecules is most common, but cellular macromolecules like proteins and DNA can also be directly involved. Direct ionization of water produces a radical ion and a free electron. The time scale for creation of these species is on the order of 10^{-16} seconds. The electron is captured via dipole interactions by the surrounding water, thus becoming a solvated election. The radical ion of water can split into a hydrogen ion and a hydroxyl radical. Excess energy from the excited water molecule can be dissipated by bond breakage to produce both hydrogen and hydroxyl radicals. These chemically reactive species produce highly reactive HO• and H• radicals.

Trapped radicals, arising via the photolysis of water and hydrogen peroxide, have been used to study aliphatic alcohols.[9] In these studies, it has been determined that solvated electrons are responsible for free radical chemistry resulting in the radical tautomers of the alcohols.

The resultant radical may be centered on any of the carbons in the aliphatic chain via hydrogen abstraction by the hydroxyl radical. The other possibility is the radical centering on the alcohol oxygen, again via hydrogen abstraction, or via tautomerization from the aliphatic chain. Centering of the radical on the oxygen is energetically favourable although carbon centered radicals can be observed via electron paramagnetic resonance, EPR.[10]

Early work looking at irradiated ice, specifically single ice crystals, were successful in showing X-ray induced photolysis leading to hydroxyl radical formation at 77°K.[11] This work, along with other studies,[12,][13] has provided the base to build our understanding of X-ray induced photolysis and hydroxyl radical damage, even at cryogenic temperatures. EPR studies of hydroxyl radicals trapped in ice have also been carried out on lithium metals in ethylamine liquid, producing a colourful solution of trapped electrons.[14] These studies confirm that radical trapping at metal centres can arise via irradiation. These structural changes, arising from irradiation induced radical formation, show that studying metal-ligand

interactions can be problematic, and ensuring that conclusions arising from such methodologies are accurate is of paramount importance.

The presence of hydroxyl radicals can lead to photooxidation in aqueous samples, along with breakdown products like hydrogen peroxide. The presence of solvated electrons in solution can lead to photoreduction. In early work, the solvated electron has been described as a mobile cavity structure, approximately 2.5 Å in radius.[15] Later investigations have shown that solvated electrons can be grouped into two categories, those weakly bound at a surface interface, and those more strongly bound within the bulk solvent.[16] These bulk solvated electrons are highly reactive and can reduce metals, long chain polypeptides, and hydroxyl groups amongst many others.[17]

Transition metal photoreduction appears far more commonly than photooxidation, although the latter is certainly observable, even in biological tissue samples.[18] Photoreduction can be observed in simple ice crystals, more complex but still relatively simple mixtures of metals and peptides, and protein crystal structures.[19, 20] As an example of photoreduction in protein crystal structures being problematic, for the enzyme sulfite oxidase there is only one reported crystal structure of an oxidized enzyme, that of a mutant possessing modified redox properties for which chemical reduction requires binding of a ligand at the metal site.[21]

This thesis focuses on photochemistry, and specifically photoreduction, of samples chosen to be relevant to biological XAS and MX experiments. The relatively high energies used in XAS experiments easily exceed the chemical bonding energies found in biological samples and systems. Because of the desire to emulate sample conditions found in XAS and MX experiments, cryoprotectants were examined. Cryoprotectants are commonly added to frozen samples to reduce ice crystals that can cause damage to macromolecules in the samples. Ice crystals can also cause diffraction of incident X-rays. These diffracted photons can cause overloads in X-ray detectors, taking them out of the linear response range, making it impossible to collect data.

1.2 Metalloproteins

A metalloprotein is a protein containing a metal ion as a cofactor and it is estimated that one quarter to one third of all proteins require that metal cofactor to function.[22] Metalloproteins can be separated into families, with roughly 11% containing zinc, and an additional 11% containing other transition metal ions.[23] Zinc metalloproteins often serve a structural role, such as the zinc-finger domain located in numerous DNA and RNA binding proteins.[24] Transition metal ion enzymes carry out chemically challenging reactions. The elements in the d-block have an electronic structure that allows them to form two or more different oxidation states. Many transition metals in the d-block participate in redox reactions and are thus useful in metalloproteins that participate in electron transfers.

In an example of metal having both a structural and redox active role, copper binding to the prion protein, PrP, demonstrates the importance of metal binding in nature. In PrP, copper binding to the histidine-rich octarepeat region can be complex, but generally Cu^{2+} is bound by four histidine side chains [25]. If chemically reduced to Cu^{+}, binding in the prion protein octarepeat region is observed to change to a diagonal complex with only two histidines. All XAS results regarding the PrP peptide and copper binding are found in Figure 1.1.

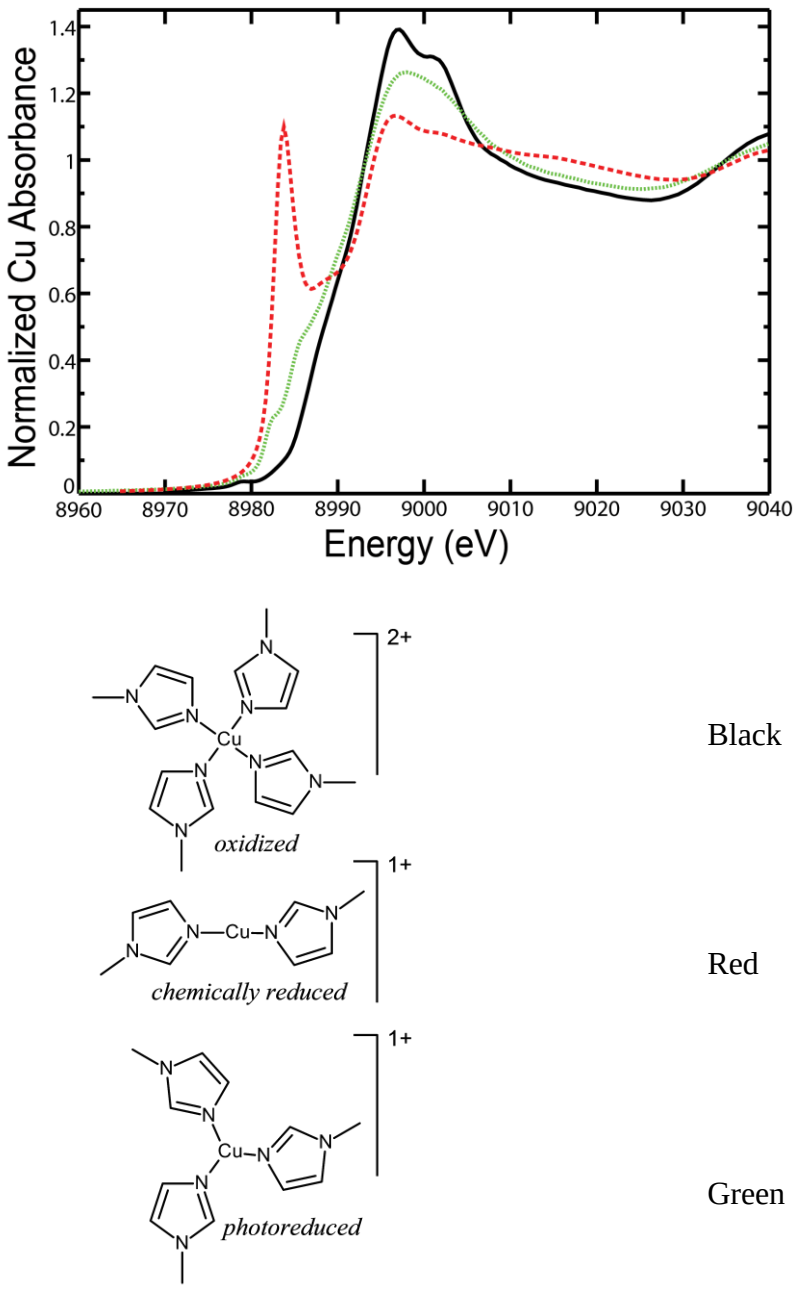

Figure 1.1 XAS spectra of PrP bound to copper. The black spectra represent the Cu^{2+} Ac-(PHGGGWGQ)4-NH2 peptide, non-photoreduced. The green spectra show the Cu^{2+} Ac-(PHGGGWGQ)4-NH peptide, photoreduced, single scan after 6h in the beam. The red spectra show Cu^{+} Ac-(PHGGGWGQ)4-NH2, chemically reduced with 20x excess of sodium ascorbate. The corresponding structures are labeled accordingly.

A further example of the importance of metalloenzymes is that of the nitrogenase enzymes which convert atmospheric nitrogen to ammonia.[26] In this family of enzymes, an iron containing protein functions as a reductase, transferring electrons from donors like flavodoxin and ferredoxin to a molybdenum-iron protein. Following the reduction of the MoFe protein, the metal centre acts as the site for nitrogen fixation, converting N_2 to $2\times NH_3$. This is a key part of the biological nitrogen cycle as "fixed" nitrogen is required for all life as nitrogen is a vital component of very many biomolecules.

1.3 Photoreduction

Photoreduction is the process of chemical reduction under the influence of radiant light. These photons may be in the ultraviolet to X-ray energy range, but of particular interest for these works is X-ray chemistry. Photochemistry, whether reduction or oxidation, is undesirable for any examination of a metal containing system where the goal of the experiment is to observe the metal or element of interest in its natural state. Metalloenzymes frequently perform redox reactions so the examination of metal in the native oxidation state is critical.

The exact mechanism of photoreduction is complex; however, a good place to start examination of this phenomenon is the photolysis of water. Ionizing radiation and the decomposition of water has been well studied.[27][28] The main decomposition species are hydrated electrons (e_{eq}^-), hydroxyl radicals (HO•), hydrogen radicals, and photoexcited water cations.

$$H_2O + h\nu \rightarrow H_2O^+ + e_{aq}^- \quad (1.1)$$

$$H_2O^+ \rightarrow H^+ + HO\bullet \quad (1.2)$$

With regards to photoreduction, the solvated electrons and hydroxyl radicals are the most relevant products of photolysis. [29] As discussed by Mesu *et al.*,[30] hydrated electrons were identified as the primary reductant in different small molecule Cu^{2+} species dissolved in water.

The photolysis of water can occur with photon energies of visible light and higher, so it also possible to observe photoreduction occuring in X-ray experiments arising from reactive species generated during photolysis. Even under cryogenic temperatures, 80 - 85 K for protein crystallography, 10-12 K for X-ray absorption spectroscopy, photoreduction can be observed.[31] In an experiment to examine the oxidation state of iron in the heme site of cytochrome *c* peroxidase, Latimer *et al.* show that Fe^{3+} can be reduced to Fe^{2+} in as little as 60 minutes of beam exposure.[32] Indeed, as Datta *et al.* described, even engineering an enzyme, in their case B_{12}-dependent methionine synthase, to specifically avoid photolysis of a methyl-cobalt bond was insufficient to avoid photodamage during data collection.[33] The photoreduction of cobalt in free and protein bound B_{12} factors via X-rays is more fully discussed in Champloy *et al.*.[34] Interestingly, when Cu^{2+} is bound to the PrP peptide in XAS samples then photoreduced, the result is a three-coordinate copper with histidine side chains moving slightly away, as would be expected for a reduced metal-ligand bond.

In addition to exposure time, the photon flux density, herein defined as photons/s/mm^2, also plays a role in photoreduction. George, *et al.* (2012) discuss the importance of limiting X-ray exposure.[35] As discussed further in Section 2.1, XAS experiments yield X-ray fluorescence of interest and unwanted scatter not originating from the sample. The fluorescence photons, or signal, are of interest for obtaining the structural information during the XAS experiment, while the scattered X-rays are noise and can obfuscate the signal of interest. While it is important to balance signal to noise and X-ray exposure, it is also important to point out that the rate of photoreduction is appoximately proportional to flux density.

As discussed by George, *et al.* (2012), synchrotron X-ray sources are moving to increased beam intensities, increasing the possibility of photochemistry in future experiments. Future upgrades to the Advanced Photon Source (APS) in the United States, and the completion of the MAX-IV facility in Sweden, have brought flux densities to unprecedented levels. New

beamlines are constantly being designed and upgraded to maximize flux densities and are thus more likely to induce photochemistry in samples being examined.

1.4 Thesis Objectives

Photoreduction was observed to occur in PrP samples binding Cu^{2+} with glycerol present as a cryoprotectant. Experimentation showed that the addition of glycerol alone was sufficient to induce a marked increase in the rate of photoreduction. These observations led to a more complete investigation of the photoreduction phenomenon. The goal of this thesis was to observe, quantify, and explain photoreduction as observed in copper samples. A kinetic model was developed and used to accomplish this objective. Once a mechanism for photoreduction was postulated and tested, it became another goal of the thesis to examine factors contributing to the proposed mechanism of photoreduction including sources of extra electrons, photochemical products of water interacting with cryoprotectants, and photoreduction ameliorating factors like ketone functional groups.

The intentional photoreduction of iron, and resultant near edge analysis, has been discussed previously.[36] In the case of thyl (RS•) radicals, they are not observed except via production using photochemistry[37]. Knowing this, a series of experiments to probe the nature of Hg(0), an otherwise rare chemical species, became another thesis objective.

Through XAS experimentation, a thorough examination of variables, and careful and considered data analysis, the work presented in this thesis outlines the development of a method to measure the rate of photoreduction in Cu^{2+} containing samples.

REFERENCES

1) Barltrop, A.; Coyle, J. D. Principles of Photochemistry, **1978**

2) Grossweiner, L. I.; Usui, Y. The role of the hydrated electron in photoreduction of cystine in the presence of indole. *J. Photochem. Photobiol.* **1970**, *11*(1), 53–56.

3) Kisker, C.; Schindelin, H.; Pacheco, A.; Rajagopalan, K. V.; Enemark, J. H.; Rees, D. C.; Molecular basis of sulfite oxidase deficiency from the structure of sulfite oxidase. *Cell*, **1997**, *91*(7), 973–983.

4) Wardman, P. The importance of radiation chemistry to radiation and free radical biology. *Br. J. Radiol.* **2009**, *82*, 89–104.

5) Roentgen, W. C.; Ueber eine neue Art von Strahlen. Vorläufige Mitteilung. *Aus den Sitzungsberichten der Würzburger Physik. medic.* **1895,** 137–147.

6) Becquerel, H. J. On the rays emitted by phosphorescence. *Compt. Rend. Acad. Sci.* **1896**, *122*, 420–421.

7) Curie, M.; Curie, P.; Bemont, G. Sur une nouvelle substance fortement radio-active contenue dans la pechblende. *Compt. Rend. Acad. Sci.* **1898**, *127*, 1215–1218.

8) Eyring, H.; Hirschfelder, J. O.; Taylor, H. S. The theoretical treatment of chemical reactions produced by ionization processes Part I. The ortho-para hydrogen conversion by alpha-particles. *J. Chem. Phys*. **1936**, *4*, 479–491.

9) Gibson, J. F.; Symons, M. C. R.; Townsend, M. G. Unstable intermediates. Part II. Photolysis of hydrogen peroxide in solid: Some reactions of hydroxyl radicals. *J. Chem. Soc.* **1959**, 269–276.

10) Asmus, K. D.; Mockel, H.; Henglein, A. Pulse radiolytic study of the site of OH· radical attack on aliphatic alcohols in aqueous solution. *J. Phys. Chem.* **1973**, *77*(10), 1218–1221.

11) Box, H. C.; Lilga, K. T.; Budzinski, E. E; Derr, R. Hydroxyl radicals in X-Irradiated single crystals of ice. *J. Chem. Phys.* **1969**, *50*, 5422–5423.

12) Gunter, T. E. Electron paramagnetic studies of the radiolysis of H_20 in the solid state. *J. Chem. Phys.* **1967**, *46*(10), 3818–3829.

13) Garrett, B.; Dixon, D.; Camaioni, D. M.; Chipman, D.; Johnson, M.; Jonah, C.; Kimmel, G.; Miller, J.; Rescigno, T.; Rossky, P.; Xantheas, S.; Colson, S.; Laufer, A.; Ray, D.;

Barbara, P.; Bartels, D.; Becker, K.; Bowen, K.; Bradforth, S.; Zwier, T. Role of water in electron-initiated processes and radical chemistry: Issue and scientific advances. *Chem. Rev.* **2005**, *105* (1), 355–390.
14) Martyn, C.; Symons, R.; Taiwo, F. A. Solvated electrons: electron paramagnetic studies of solutions of lithium in ethylamine*. *J. Chem. Soc., Dalton Trans.* **1998**, 1395–1396.
15) Kevan, L. Solvated electron structure in glassy matrixes. *Acc. Chem. Res.* **1981**, *14*(5), 138–145.
16) Abel, B.; Buck, U.; Sobolewski, A. L.; Domcke, W. On the nature and signatures of the solvated electron in water. *Phys. Chem. Chem. Phys*. **2012**, *14*, 22–34.
17) Levina, A.; Armstrong, R. S.; Lay, P. A. Three-dimensional structure determination using multiple-scattering analysis of XAFS: applications to metalloproteins and coordination chemistry. *Coord. Chem. Rev*. **2005**, *249*, 141–160.
18) Hackett, M. J.; Smith, S. E.; Paterson, P. G.; Nichol, H.; Pickering, I. J.; George, G. N. X-Ray Absorption Spectroscopy at the Sulfur K-Edge: A New Tool to Investigate the Biochemical Mechanisms of Neurodegeneration. *ACS Chem. Neurosci.* **2012**, *3*, 178–185.
19) Grossweiner, L. I.; Usui, Y. The role of the hydrated electron in photoreduction of cystine in the presence of indole. *J. Photochem. Photobiol.* **1970**, *11*(1), 53–56.
20) Kisker, C.; Schindelin, H.; Pacheco, A.; Rajagopalan, K. V.; Enemark, J. H.; Rees, D. C.; Molecular basis of sulfite oxidase deficiency from the structure of sulfite oxidase. *Cell*, **1997**, *91*(7), 973–983.
21) Qiu, J. A.; Wilson, H. L.; Pushie, M. J.; Kisker, C.; George, G. N.; Rajagopalan, K. V. The Structures of the C185S and C185A mutants of sulfite oxidase reveal rearrangement of the active site. *Biochemistry*, **2010**, *49*(18), 3989–4000.
22) Waldron, K. J.; Robinson, N. J. How do bacterial cells ensure that metalloproteins get the correct metal? *Nat. Rev. Microbiol.* **2009**, *7*(1), 25–35.
23) Pushie, M. J.; Cotelesage, J. J.; George, G. N. Molybdenum and tungsten oxygen transferases – structural and functional diversity within a common active site motif. *Metallomics*, **2014**, *6*, 15–24.

24) Miller, J.; McLachlan, A. D.; Klug, A. Repetitive zinc-binding domains in the protein transcription factor IIIA from *Zenopus* oocytes. *The EMBO Journal*, **1985**, *4*(6), 1609–1614.

25) McDonald, A.; Pushie, M. J.; Millhauser, G. L.; George, G. N. New insights into metal interactions with the prion protein: EXAFS analysis and structure calculations of copper binding to a single octarepeat from the prion protein. *J. Phys. Chem. B.* **2013**, *117*, 13822–13841.

26) Howard, J. B.; Rees, D. C. How many metals does it take to fix N_2? A mechanistic overview of biological nitrogen fixation. *Proc. Natl. Acad. Sci. USA*, **2006**, *103*, 17088–17093.

27) Gunter, T. E. Electron Paramagnetic Studies of the Radiolysis of H_20 in the Solid State. *J. Chem. Phys.* **1967**, *46*(10), 3818–3829.

28) El Omar, A. K.; Schmidhammer, U.; Jeunesse, P.; Larbre, J. P.; Lin, M.; Muroya, Y. Time-dependent radiolytic yield of OH radical studied by picosecond pulse radiolysis. *J. Phys. Chem. A.* **2011**, *115*(44), 12212–12216.

29) Marsalek, O.; Uhlig, F.; VandeVondele, J.; Jungwirth, P. Structure, dynamics, and reactivity of hydrate electrons by *ab initio* molecular dymnamics. *Acc. Chem. Res.* **2012**, *45*(1), 23–32.

30) Mesu, J. G.; Beale, A. M.; de Groot, F. M.; Weckhuysen, B. M. Probing the influence of X-rays on aqueous copper solutions using time-resolved in situ combined video/X-ray absorption near-edge/ultraviolet visible spectroscopy. *J. Phys. Chem. B.* **2006**, *110*(35), 17671–17677.

31) George, G. N.; Pickering, I. J.; Kisker, C. X-ray absorption spectroscopy of chicken sulfite oxidase crystals. *Inorg. Chem.* **1999**, *38*(10), 2539–2540.

32) Latimer, M. J.; Ito, K., McPhillips, S. E.; Hedman, B. Integrate instrumentation for combined polarized single-crystal XAS and diffraction data acquisition for biological applications. *J. Synchrotron Radiat.* **2005**, *12(Pt 1)*, 23–27.

33) Datta, S.; Koutmos, M.; Pattridge, K.; Ludwig, M.; Matthews, R. A disulfide-stabilized conformer of methionine synthase reveals an unexpected role for the histidine ligand of the cobalamin cofactor. *Proc. Nat. Acad. Sci.* **2008**, *105*(11), 4115–4120.

34) Champloy, F.; Gruber, K.; Jogi, G.; Kratky, C. XAS spectroscopy reveals X-ray-induced photoreduction of free and protein-bound B12 cofactors. *J. Synchrotron Radiat.* **2000**, *7*, 267–273.

35) George, G. N.; Pickering, I. J.; Pushie, M. J.; Nienaber, K. H.; Hackett, M. J.; Ascone, I.; Hedman, B.; Hodgson, K. O.; Aitken, J. B.; Levina, A.; Glover, C.; Lay, P. A. X-ray-induced photo-chemistry and X-ray absorption spectroscopy of biological samples. *J. Synchrotron Radiat.* **2012**, *19(Pt 6)*, 875–886.

36) George, S. J.; Fu, J.; Guo, Y.; Drury, O. B.; Friedrich, S.; Rauchfuss, T.; Volkers, P. I.; Peters, J. C.; Scott, V.; Brown, S. D.; Thomas, C. M.; Cramer, S. P. X-ray photochemistry in iron complexes from Fe(0) to Fe(IV) – Can a bug become a feature? *Inorganica Chim. Acta*, **2008**, *361*, 1157–1165.

37) Sneeden, E; Hackett, M. J.; Cotelesage, J. J. H; Prince, R. C.; Barney, M.; Goto, K.; Block, E.; Pickering, I. J.; George, G. N. Photochemically-generated thiyl free radicals observed by X-ray absorption spectroscopy. *J. Am. Chem. Soc.* **2017**, *139*(33), 11519–11526.

2. X-ray Absorption Spectroscopy

2.1 Theory

X-rays passing through matter will interact in three different manners; photoelectric absorption, Compton[1] (incoherent) scattering, and Rayleigh[2] (coherent) scattering. Absorption is predominant at lower energies, below 25 keV, whereas scattering predominates over higher energy X-rays. The absorption coefficient (the relationship between incident and transmitted beam intensity) is given by:

$$\mu(E)x = ln\frac{I_0}{I} \tag{2.1}$$

where μ is the absorption coefficient, x is the sample thickness, and I_0 and I are the incident and transmitted X-ray intensities respectively. X-ray absorption decreases with energy except when the core electron binding energy is matched by the incident X-ray energy. In those cases, the X-rays are absorbed and a core electron is ejected. This ejection increases the absorption coefficient sharply and is called an absorption edge. These absorption edges are named K, L, M etc. based on the principal quantum number. Every element has unique electron binding energies and thus unique a unique K-edge, L-edge, etc. By tuning the wavelength of the incident X-ray beam to specifically sweep over those energies, X-ray absorption spectra can be collected for each element of interest.

X-ray absorption spectra are usually split into 2 parts: the region adjacent to the absorption edge, known as the near edge, and the extended X-ray absorption fine structure (EXAFS) region.[3] The near edge refers to the region leading up to the absorption edge and continues for around 50 eV past when the EXAFS structure dominates the spectra. Analysis of the near edge can provide information about coordination environment, subtle geometric distortions of the coordination environment, and oxidation state. The near edge features are dominated by transitions by the core electrons to bound states. These include dipole and quadrupole allowed transitions dictated by selection rules.

$$\Delta l = \pm 1 \qquad \text{Dipole} \qquad (2.2)$$

$$\Delta l = \pm 2 \qquad \text{Quadrupole} \qquad (2.3)$$

Near-edge spectra are dominated by $\Delta l = \pm 1$ dipole-allowed transitions, which in the case of K-edges of first transition metal ions, will have a lot of 1s→4p character. Transition metal ions having 3d vacancies also show dipole-forbidden, but weak quadrupole-allowed $\Delta l = \pm 2$ 1s→3d transitions, which can gain dipole-allowed intensity in non-centrosymmetric environments by a mixture of 4p levels. The studies described herein focus on Cu^{2+} and Cu^{+}, and our discussion will therefore focus on the spectra of these metal ions. The near-edge spectra of Cu^{2+} and Cu^{+} complexes differ in a few respects. Cu^{2+} is formally $3d^9$ and spectra thus show a 1s→3d transition as the lowest energy transition in the K near-edge spectra. For Cu^{+} K-edge spectra 1s→4p transitions are the lowest in energy and the spectra overall are shifted to lower energy when compared to Cu^{2+}.

These near edge transitions can give information about the backscattering atoms bound to the absorber atom. The bound atoms, hard or soft ligands, and the electronic environment will shift the amount of energy required to eject a core electron, and thus shift the near edge spectra to lower or higher energies accordingly.

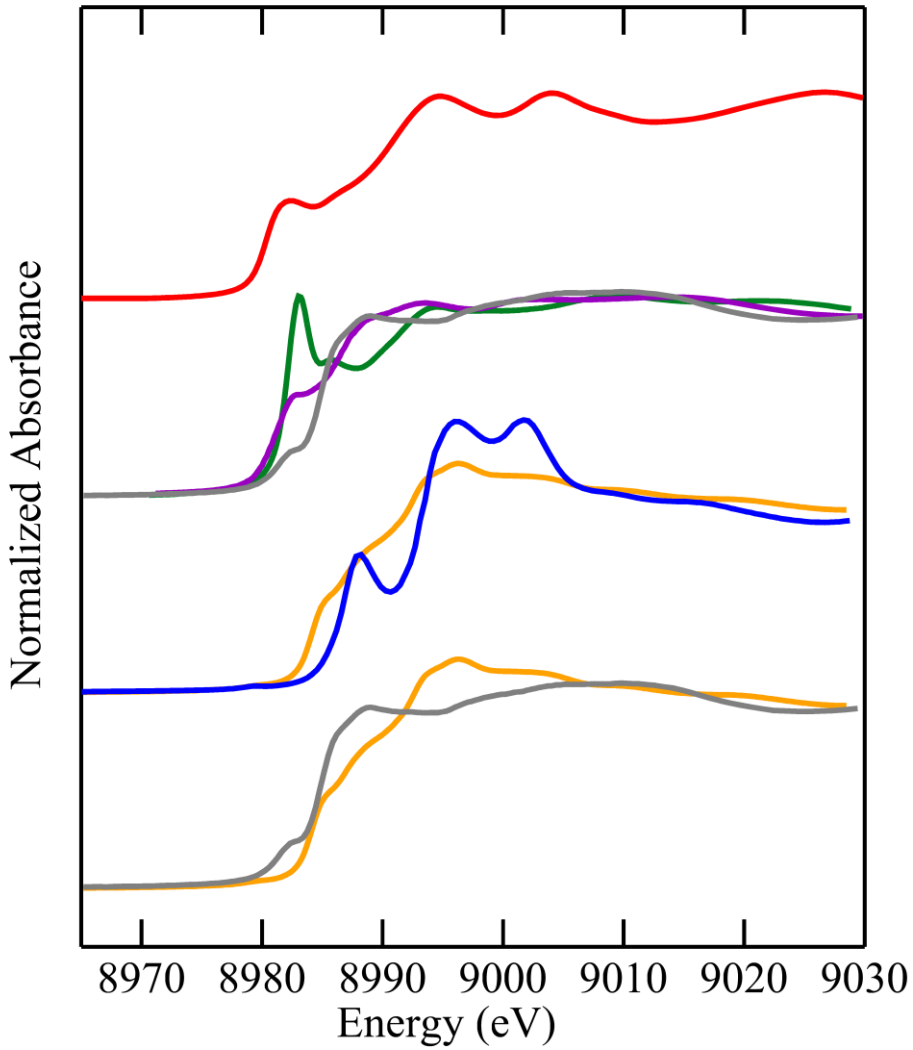

Figure 2.1 Examples of copper near edge changes with different ligands. The top trace in red shows Cu foil or Cu(0). The next traces down show Cu(I) bound to two (grey), three(purple), and four(green) sulphurs. The third trace from the top shows Cu(II) bound to four imidazole moieties (nitrogen ligand)(shown in blue) and bound to four sulphurs (shown in orange). The bottom traces show the differences in near edge spectra arising from differences in oxidation state. The blue trace shows Cu(I) bound to four sulphurs while the Cu(II) bound to four sulphurs is shown in orange.

The EXAFS is a modulation of the X-ray absorption which arises from backscattering of emitted photoelectrons by nearby atoms. With suitable analysis the EXAFS can provide structural information concerning atoms nearby the absorber atom, up to approximately 5 Å enveloping the absorbing atom. Accurate bond distances (within 0.02 Å) can be obtained via analysis of EXAFS oscillations but the resolution of EXAFS is relatively poor as given by Equation 2.4:

$$\Delta R = \frac{\pi}{2k} \tag{2.4}$$

where ΔR is the total difference in bond length between two different backscattering atoms from the central absorbing atom, for a single scattering path, and k is defined as:

$$k = \left(\frac{2\pi}{\lambda_e}\right) = \sqrt{\frac{2m_e}{\hbar^2}(E - E_0)} \tag{2.5}$$

where λ_e is the de Broglie wavelength; m_e is the electron rest mass, E is the incident X-ray energy, and E_0 is the absorption edge threshold energy (the energy required to eject an electron from the core just to the continuum and no further).

The EXAFS equation describes the wave form of the photoelectron path from the central absorbing atom and the surrounding backscattering atoms as follows:

$$\chi(k) = S_0^2 \sum_i \frac{N_i S_i(k) f_1(k)}{kR_1{}^2} e^{-2R_i/\lambda_i(k)} e^{-2\sigma_i^2 k^2} \sin[2kR_i + \phi_i(k) + \delta_c(k)] \tag{2.6}$$

The variables of the EXAFS equation are defined as: N_i = coordination number for atom type i, R_i = absorber-backscatterer distance for atom type i, σ_i^2 = mean-square deviation in R_i (the Debye-Waller factor)[4,5], S_0^2 = total amplitude reduction factor, $S_i(k)$ = amplitude reduction function, $\lambda(k)$ = photoelectron mean free path function, $A_i(k)$ = EXAFS total amplitude function, $\varphi_i(k)$ = EXAFS total phase shift function, and k = photoelectron wave vector defined in Equation 2.5.

In this form, the parameters usually refined via least squares fit are coordination number, interatomic distance, Debye-Waller factor, and ΔE_0, the energy offset or threshold energy where the EXAFS oscillations start. The functions sensitive to chemical changes are $A_i(k)$, the total amplitude, $\varphi_i(k)$, the total phase, and $\lambda_i(k)$, the mean free path functions. In modern EXAFS analysis these parameters are typically computed using *ab initio* methods.

REFERENCES

1) Compton, A. H. A Quantum theory of the scattering of X-rays by light elements, *Phys. Rev*. **1923**, *21* (5), 483–502.

2) Strutt, J.W. XV. On the light from the sky, its polarization and colour, *London, Edinburgh, Dublin Phil. Mag. J. Sci*. **1871**, *41* (271), 107–120.

3) Sayers D.E., Lytle F.W., Stern E.A. Point scattering theory of X-ray K absorption fine structure. *Adv. X-ray Anal*. **1970**, *13*, 248–271.

4) Debye, P. Interferenz von Röntgenstrahlen und Wärmebewegung. *Annalen der Physik*, **1913**, *348* (1), 49–92.

5) Waller, I. Zur Frage der Einwirkung der Wärmebewegung auf die interferenz von Röntgenstrahlen, *Zeitschrift für Physik A*, **1923**, *17* (1), 398–408.

3. Methods

3.1 Photoreduction Experiments

All XAS measurements were made at Stanford Synchrotron Radiation Lightsource (SSRL) with the SPEAR3 storage ring containing 400 or 500 mA at 3.0 GeV. Beamline 7-3 is equipped with a rhodium-coated vertical collimating mirror upstream of the Si(220) monochromator. All of the earlier measurements in this thesis employed this mirror, but due to thermal damage from the increased current in SPEAR, this mirror was not utilized for later measurements. Harmonic rejection was accomplished by setting the cut-off angle of the mirrors to 12 keV for copper experiments and 15 keV for mercury experiments. Incident and transmitted X-rays were monitored using gas ionization chambers and X-ray absorption was measured as the Cu Kα fluorescence excitation spectrum using an array of 30 germanium detectors (Canberra Ltd. Meriden, CT, USA). During data acquisition samples were maintained at a temperature of approximately 10 K using an Oxford Instruments CF1204 helium cryostat.

Individual scans were collected using X-ray fluorescence on SSRL XAS beamline 7-3 and were designed to be as fast as possible while maintaining adequate signal to noise for normalization and background subtraction. XAS scans generally consist of three discrete segments, a pre-edge segment with large steps in energy (i.e. 10 eV), an edge segment with fine steps over the absorption edge to capture any details, and a post-edge segment which captures the post-edge region, which may include the EXAFS oscillations. The coarse point-spacing in the pre-edge region meant that the scan progressed to the structured part of the spectrum quickly. On beamline 7-3 there is an overhead on motor moves of 0.25 sec., and count times per point were 0.5 sec., with a monochromator settle time of 0.1 sec., to ensure mechanical settling post monochromator move, resulting in a total time per data point of 0.85 sec. The monochromator was moved to first energy point in the scan before data collection began so ~1 min. was required to reach the detailed part of the near-edge spectrum, representing the shortest irradiation time observed. The time per scan was calculated from the time-date stamp recorded for creation of each data file.

All photoreduction experiments were carried out for a varying number of sweeps until successive spectra overlapped representing a complete conversion to Cu^{+}. The near edge features of replicate samples are identical in appearance when the photoreduction process is complete. For experiments involving beam attenuation, varying thicknesses of aluminum were inserted into the X-ray flight path upstream of the sample chamber.

Because of the necessity of collecting the pre-edge, the structured part of the spectrum took 59.5 seconds to reach so that the first data point is at just under 1 minute. The scan takes 5.43 minutes so successive points are 4.4 min. apart, or 5.4, 9.8, 14.2, 18.6 min., and so-on. As depicted in Figure 3.1, the changes in the spectra due to photoreduction of initial Cu^{2+} to Cu^{+} were observed and near edge spectra were fitted using as linear combinations of the first sweep and last sweeps.

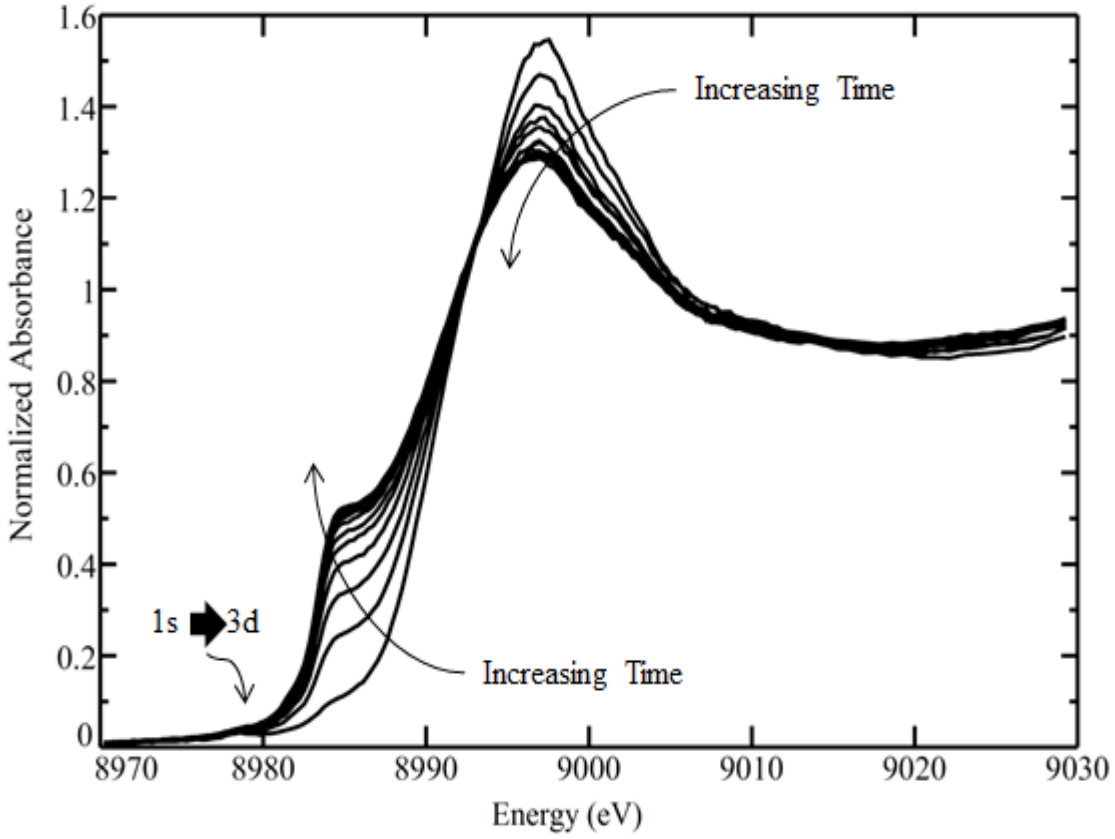

Figure 3.1 Example of a typical photoreduction experiment of an aqueous solution of 2mM $CuCl_2$ in the presence of 25% v/v glycerol. The 12 sweeps were collected over a period of 61 minutes.

3.2 Kinetic Model and Data Fitting

Considering the analysis of the kinetics of set of time dependant data employing the end members of the data set to derive kinetic information. During the experiment the photon flux will be essentially constant, and we assume that any photochemistry involving water and cryoprotectant has reached a kinetic steady state, so that the solution concentrations of hydrated electrons and hydroxyl radicals will be constant. Under such conditions the photochemical conversion of Cu^{2+} to Cu^{+} will be expected to be a pseudo-first order reaction, of the type $A \rightarrow B$, where $[A]$ and $[B]$ represent the concentrations of Cu^{2+} and Cu^{+}, respectively. In our analyses, X-ray absorption spectra are normalized to the edge-jump, so that all features are represented as a fraction of the total copper. Thus, as that sample is initially all Cu^{2+}, with a concentration $[A]_0$ for pseudo-first order kinetics we can write:

$$[A] = [A]_0 e^{-kt} \tag{3.1}$$

$$[B] = [A]_0 (1 - e^{-kt})$$

Given that:

$$[A]_0 = [A] + [B] \tag{3.2}$$

The fraction of Cu^{2+}, x_t, is simply given by:

$$\frac{[A]}{[A]+[B]} = e^{-kt} \tag{3.3}$$

We wish to determine the rate constant, k, through fitting of a kinetic series of spectra consisting of n spectra, to the end members, recorded at times t_1 and t_n. The spectra at these times will in most cases be mostly, but not entirely, those of the reactant and product. In what follows we assume that there are no significant changes in the structured region (i.e. the chemically specific region) of the spectra during individual scans.

We then fit S_t, the general spectrum at t to a linear combination of S_{t1} and S_{tn}. The data set is the timed series starting at the first time t_1 with a spectrum S_{t1} through the spectrum at time t, S_t to the spectrum at the n'th point S_{tn}. If x_t is the fraction of Cu^{2+} at time t then:

$$S_t = x_t S_{t1} + (1 - x_t) S_{tn} \tag{3.4}$$

In terms of true spectra of A and B:

$$S_t = S_B + (S_A - S_B)\exp(-kt)$$
$$\exp(-kt) = x_t(\exp(-kt_1) - \exp(-kt_n)) \tag{3.5}$$

$$x_t = \frac{\exp(-kt)}{\exp(-kt_1) - \exp(-kt_n)} \tag{3.6}$$

Where $\{\exp(-kt_1) - \exp(-kt_n)\}$ will be a constant c for a particular experiment, with c always having a value between 0 and 1 and under the ideal conditions $S_{t1} = S_A$ and $S_{tn} = S_B$, c = 1. The spectra of a time series were fit to a linear combination of the end members using the exafspak[1] program datfit to give x_t as seen in Figure 3.2. The curves of x_t versus t were fit using the built-in fitter in GNUPLOT[2] to give values of k and c, with the general equation for all lines:

$$x_t = \frac{exp(-kt)}{c} \tag{3.7}$$

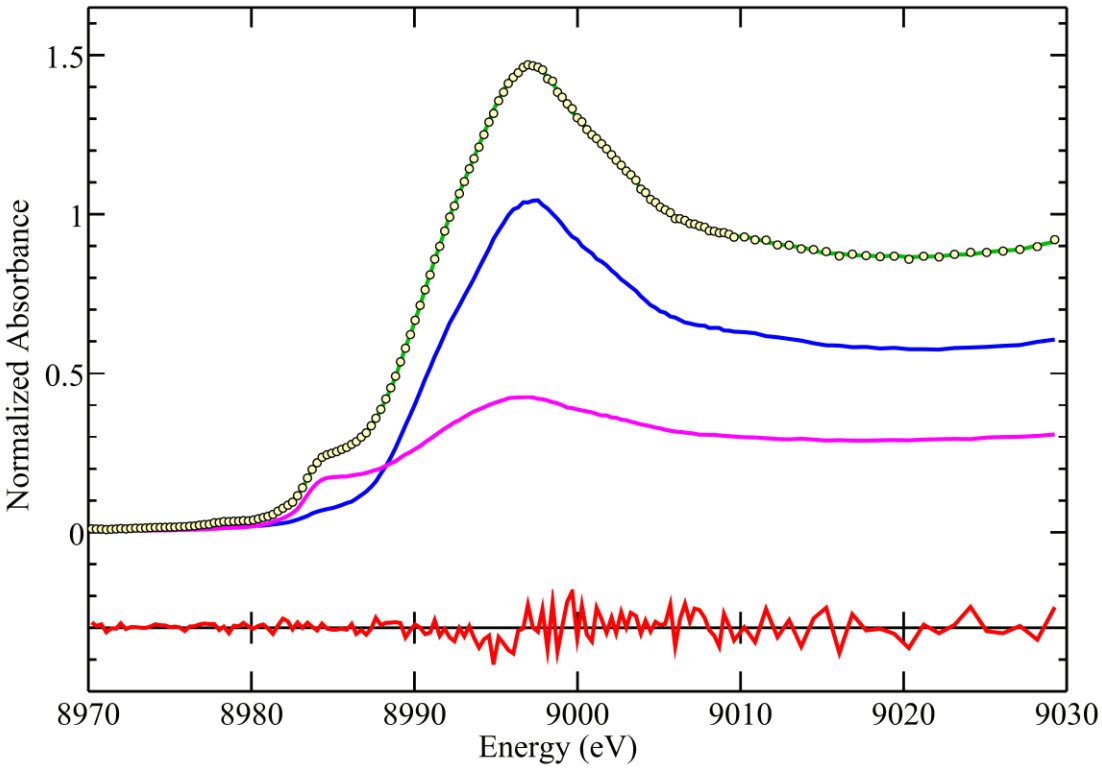

Figure 3.2 Example fitting from a 2 mM $CuCl_2$ + 25% glycerol sample using DATFIT. The points show the sweep to be fitted, and the green line shows the best linear combination fit of the first (blue) and last (magenta) sweeps. The residual is shown as the red line offset below the other lines and scaled up by a factor of 10.

Because spectra are typically normalized with the edge-jump, giving a per-copper absorption, the effective pseudo-first order rate constants are expressed in units of only min^{-1}. A plot of ln [normalized Cu^{2+}] vs time, as seen in Figure 3.3, gives rise to a straight line with a slope of k_{eff}, the effective rate constant in min^{-1}. True rate constants, with units of $mol \cdot min^{-1}$ can be derived from these by simply multiplying by the copper concentration.

3.3 Density Functional Theory Calculations

DFT is now very well established as the gold standard for many quantum chemistry calculations. When employed properly, DFT can produce optimized geometries of structures, especially useful for EXAFS calculations involving systems with many backscattering atoms and multiple scattering paths. Transition state structures can also be a useful calculation provided by density functional theory. Transition state geometry optimized structures, along with transition state energies, can be obtained from DFT calculations allowing for possible mechanisms to be tested. DFT computed reaction enthalpies are also useful for determining both likely and unlikely reactions. There are several highly efficient and reliable implementations for this technique. Density functional theory enables computation of total energies under general conditions, used for both structure prediction and for calculation of thermodynamic properties. It provides an excellent balance between accuracy and computational cost, and, using modern computer hardware, calculations involving thousands of electrons are practical.

Standard DFT calculations do have some limitations. For example, dispersion effects are not accounted for by basic density functional theory calculations. Standard DFT calculations are known to have difficulty producing correct results for stacking interactions and hydrogen bonding. More modern modified Generalized Gradient Approximation (mGGA) functionals M11-L is an mGGA based functional that is good for transition metals and non-covalent interactions. A recent review has also shown the M11-L is the most accurate functional when accounting for self-interaction errors, as most GGAs underestimate those errors.[4]

The electron density distribution dictates the energy state, and the movement of all electrons can be summarized from this electron density. Density functional methods then rely solely on electron density and not all of the intrinsic details of electron movement.

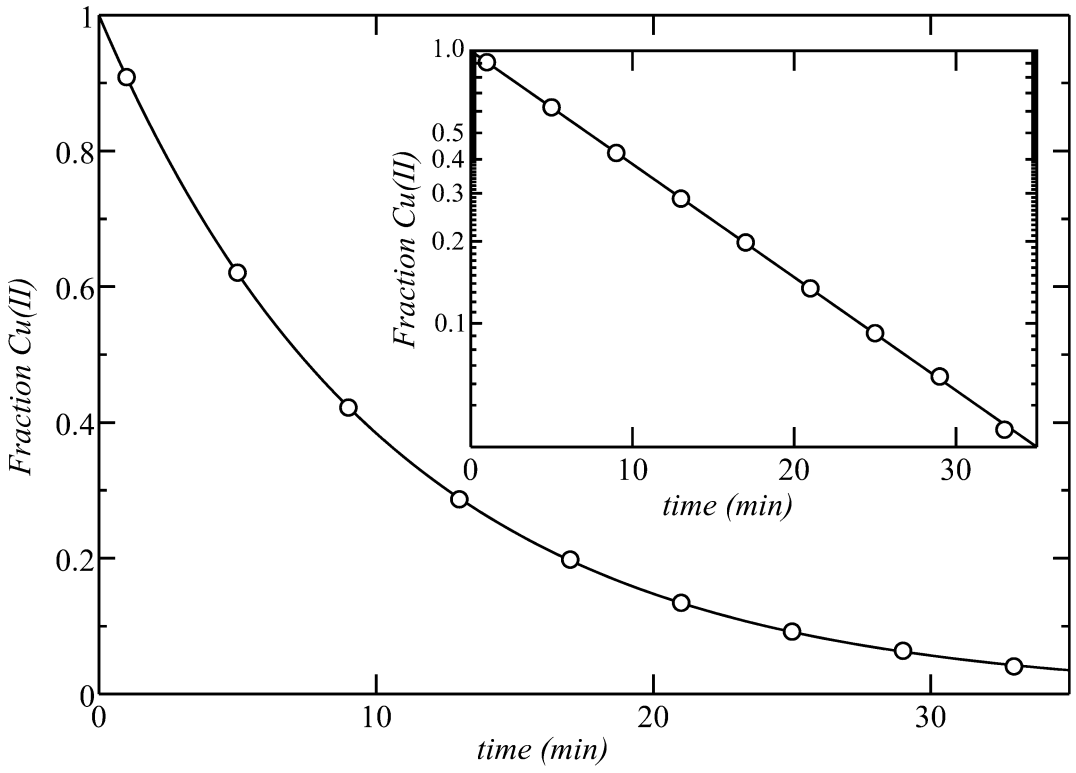

Figure 3.3 Example kinetic data, x_t vs t, for a 2 mM $CuCl_2$ + 25% glycerol sample. The fraction of Cu^{2+} at a time of 1 minute was determined as described by fitting the data using Equation 12 in GNUPLOT. The corresponding best fit line shown here was used to determine $k_{eff,}$ the effective rate constant, for each sample. The inset shows the data and the fit plotted on a $\log_{10}$ scale, illustrating the pseudo first-order kinetics.

The electron distribution of a system of atoms is not sufficient to extract the energy of said electronic system. There are numerous methods to calculate the energy of the desired system of electrons. Most of these methods, functionals, separate the energy into discrete parts. Some of them may be known exactly, such as energy of electron - nuclei interaction. Some, however, are not, such as energy of electron-electron interaction.

Another possible way to conduct these calculations is to include members dependent on electron density gradient, to acknowledge that electron density in a molecule varies from point to point. This is known as the Generalized Gradient Approximation (GGA) approach. The mGGA includes exact exchange and GGA corrections in addition to Local Density Approximation (LDA) electron-electron and electron-nuclei energy.

As such, the Generalized Gradient Approximation (GGA) and the Perdew-Burke-Ernzerhof (PBE) functionals were employed. As discussed in Section 6.8.1, the use of these functionals provides reasonably accurate results with lower demands on computer memory resources. DMol^3 permits minima and geometry searches, including or excluding geometry constraints, as well as properties of the configuration of the electrons. DFT geometry optimizations were carried out using DMol^3 and Biovia Materials Studio Version 2017 R2[3, 4] using the meta-GGA approximation employing the M11-L functional both for the potential and for the energy.[5] Greater variational freedom is obtained by providing larger basis sets. Generation of an entire second set of functions results in doubling the basis set size; this is referred to as a double-numerical (DN) set. DMol^3 double numerical basis sets can include polarization functions for all atoms with all-electron relativistic core treatments. Environmental effects were modeled using the Conductor-like Screening Model (COSMO)[6] in DMol^3, with a dielectric value representing water with 25% glycerol ($\varepsilon = 69.53$). COSMO is a continuum solvation model (CSM)[7] where the solute molecule forms a cavity within the dielectric continuum of permittivity, ε, that represents the solvent. An electrostatic COSMO potential is present in every SCF cycle. By incorporating solvent effects within the SCF cycles gives the COSMO scheme a computational advantage. DMol^3/COSMO orbitals are obtained via variational scheme meaning that accurate analytic gradients can be obtained in relation to the solute atoms and their coordinates. In summary, a cavity surface is made to begin the DMol^3/COSMO calculation. The electrostatic COSMO potential is calculated using the

electric screening charges present when electrons repel each other, opening a small positive charge. An iterative process of calculation of these potentials results in a final solution. In addition to the DMol^3/COSMO electrostatic energy, geometries may also be calculated in these iterations. Once complete, the cavity surface can be recalculated, and the optimization can continue until criteria for the convergence are met.

3.4 Photoreduction Samples

All photoreduction samples were prepared using materials obtained from Sigma-Aldrich and all values listed are final concentrations in the samples. For a control, a 2 mM $CuCl_2$ + 25% glycerol v/v sample was run with every data set collected.

All photoreduction samples were run as described in Section 3.1. and analyzed as described in Section 3.2.

3.5 Photon Flux Calculations from Ion Chamber Readings

The following assumes that a gas ionization chamber detector is being operated in the so-called plateau region. When an X-ray photon is absorbed by a gas, it results in ejection of one or more photoelectrons from the gas atom (e.g. He, Ar, Kr) or molecule (e.g. N_2). These photoelectrons will collide with other gas atoms, causing the ejection of additional lower-energy photoelectrons. Ejection of electrons leaves core holes which are filled by decay of outer electrons with concomitant emission of X-ray fluorescence (which may be absorbed by other gas atoms) or by Auger electron emission. One of the advantages of these complex processes is that each incident X-ray photon produces charge carriers (electrons and positive ions) and the number of these is proportional to the energy of the incident X-ray photon. The energy that it takes to produce an electron-ion pair E_{ion} depends upon the ion chamber gas, and for N_2 $E_{ion} \approx 36$ eV, so that absorption of one X-ray photon of 9000 eV by N_2 will produce 250 charge carriers. Gas ionization chamber detectors have parallel plates across which a high voltage (the sweeping voltage) is maintained, and the presence of charge carriers gives rise to a current flow between the plates, which in turn feeds a current-to-

voltage amplifier and is registered as a voltage. Typically, the sensitivity in volts per ampere or gain (the reciprocal of the sensitivity) is adjusted to give a voltage in a convenient range, for example 0.1 to 4.9 V.

The number of charges registered in one second can be calculated from the current flowing in the ion chamber (the voltage divided by the gain) using the elementary charge q_e (1.602×10^{-19} C). Thus, absorption of a single photon at 9000 eV by N_2 will produce a current of $I = (E/E_{ion}) \cdot q_e = 250\times1.602\times10^{-19} \approx 4\times10^{-17}$ Amperes, and the number of photons registered (absorbed) in the ion chamber can be simply calculated by

$$N_{absorbed} = \left(\frac{E_{ion}}{E}\right)\frac{I}{q_e} \tag{3.5}$$

Ideally, a gas ionization chamber detector will absorb perhaps a few percent of the incident photons, leaving most of the X-rays available for the experiment itself. Thus, to estimate the photon flux the absorption of the ion chamber gas must also be calculated. The fraction of photons absorbed by an ion chamber of path-length *x* is given by

$$\frac{N_{absorbed}}{N_{incident}} = [1 - exp(-\mu(E)x)] \tag{3.6}$$

where $\mu(E)$ is the absorption coefficient of the gas filling the ion chamber, which is given by $\mu(E) = \sigma(E)_{tot}\rho$ where $\sigma(E)_{tot}$ is the total elemental X-ray cross-section (available from the McMaster tables[8]) and ρ is the density of the gas. Thus, the incident photon flux in photons·second^{-1} can be calculated from

$$N_{incident} = \left(\frac{E_{ion}}{E}\right)\frac{I}{q_e[1 - exp(-\sigma(E)_{tot}\rho x)]} \tag{3.7}$$

In practice, for accurate calculations a scaling correction using the sum of the photoelectric cross-section and the incoherent X-ray cross-section$\left(\sigma(E)_{pe} + \sigma(E)_{incoh}\right)$, divided by the total X-ray cross-section $\sigma(E)_{tot}$ (all of which are available from the McMaster tables[1]) should be factored in to the expression.

Photon fluxes can be conveniently calculated from ion chamber output readings using the exafspak program photon, which takes five arguments:

```
$ photon
$ photon <eV> <volts> <gain> <length> <gas>
$ photon 9000 2.1 5E5 15 N2
      0.132482E+13 photons/sec
```

Where the length of the ion chamber **<length>** is specified in cm.

REFERENCES

1) George, G. N. **2000**, http://www-ssrl.slac.stanford.edu/exafspak.html

2) Williams, T.; Kelley, C.; Gnuplot 4.5: an interactive plotting program, **2011**, URL http://gnuplot.info. (Last accessed: 2019 October 28)

4) Peverati, R.; Truhlar, D. G. Performance of the M11-L density functional for bandgaps and lattice constants of unary and binary semiconductors. *J. Chem. Phys.* **2012**, *136* (13), 117–124.

5) Delley, B. An all-electron numerical method for solving the local density functional for polyatomic molecules. *J. Chem. Phys*. **1990**, *92*, 508–517.

6) Delley, B. From molecules to solids with the $DMol^3$ approach. *J. Chem. Phys*. **2000**, *113*, 7756–7764.

7) Peverati, R.; Truhlar, D. G. M11-L: A local density functional that provides improved accuracy for electronic structure calculations in chemistry and physics. *J. Phys. Chem. Lett*. **2012**, *3*, 117–124.

8) Klamt, A.; Schüürmann, G. COSMO: a new approach to dielectric screening in solvents with explicit expressions for the screening energy and its gradient. *J. Chem. Soc., Perkin Trans.* **1993**, *2*, 799–805.

9) Tomasi, J.; Persico, M. Molecular Interactions in Solution: An Overview of methods based on continuous distributions of the solvent. *Chem. Rev*. **1994,** *94* (7), 2027–2094.

10) McMaster, W. H.; Del Grande, N. K.; Mallett, J. H.; Hubbell, J. H. Compilation of X-Ray cross sections. Lawrence Livermore National Laboratory Report UCRL-50174, Sec II, Rev.1 **1969**.

4. Cryoprotectants Exacerbate X-ray Induced Photoreduction

4.1 Preface

Based on observations made collecting XAS data on Cu^{2+} bound to a prion protein peptide, a study was undertaken to examine the phenomenon of X-ray induced photoreduction. After careful analysis, a series of photoreduction experiments were designed based on the original peptide samples. The initial set of photoreduction experiments were run with $CuCl_2$ and various common cryoprotectants, including glycerol. As photolysis of water is the primary source of oxidizing and reducing species, experiments were also carried out to examine the effects of photon flux on the rate of photoreduction.

4.2 Manuscript Author Contributions

This chapter was published in *The Journal of Physical Chemistry Letters* and was reformatted to follow the guidelines for a manuscript style thesis.

Kurt H. Nienaber, M. Jake Pushie, Julien J. H. Cotelesage, Ingrid J. Pickering, and Graham N. George. Cryoprotectants Severely Exacerbate X-ray-Induced Photoreduction (**2018**) The Journal of Physical Chemistry Letters, *9*(3), 540-544

Kurt H. Nienaber took primary responsibility for experimental design, sample preparation, data collection and analysis, and manuscript drafting. M. Jake Pushie and Julien J. H. Cotelesage assisted in data collection and analysis. Ingrid J. Pickering aided in experimental setup and manuscript editing. Graham N. George assisted in experimental design, manuscript drafting and editing.

4.3 Acknowledgements

This work was supported by Discovery Grants from the Natural Sciences and Engineering Research Council of Canada (NSERC, IJP and GNG), an Innovation and Science Fund of Saskatchewan (IJP), a Canada Foundation for Innovation John Evans Leader's Fund award

(IJP) and by Canada Research Chairs (IJP and GNG). KHN was funded by the Gene Expression Mapping using Synchrotron Light group grant from the Saskatchewan Health Research Foundation (Nichol, group leader) and was a Fellow in the Canadian Institutes of Health Research-Training grant in Health Research Using Synchrotron Techniques (THRUST). Use of the Stanford Synchrotron Radiation Lightsource, SLAC National Accelerator Laboratory, is supported by the U.S. Department of Energy, Office of Science, Office of Basic Energy Sciences under Contract No. DE-AC02-76SF00515. The SSRL Structural Molecular Biology Program is supported by the DOE Office of Biological and Environmental Research, and by the National Institutes of Health, National Institute of General Medical Sciences (including P41GM103393). The contents of this publication are solely the responsibility of the authors and do not necessarily represent the official views of NIGMS or NIH.

4.4 Abstract

Approximately 11% of enzymes contain a transition metal ion that is essential for catalytic function. Such metalloenzymes catalyze much of the most chemically challenging and biologically essential chemistry carried out by life. X-ray based methods, predominantly macromolecular crystallography (MX) and also X-ray absorption spectroscopy (XAS), have proved essential for determining structures of transition metal ion-containing active sites in order to deduce enzyme catalytic mechanisms. However, X-ray irradiation can induce change in both oxidation state and structure of the metal, which is problematic in structure determination. We present an XAS study of whether cryoprotectants such as polyethyleneglycol (PEG) or glycerol, routinely added to MX or XAS samples to improve data quality, affect photoreduction. Our data demonstrate a remarkable 10-fold exacerbation in rate of photoreduction of Cu(II) to Cu(I) when alcohol or ether cryoprotectants are present. Our results suggest that widespread use of cryoprotectants may increase potential for erroneous structures.

4.5 Introduction

Since its first use in 1976,[1] synchrotron radiation has become well established as the primary source of X-rays for macromolecular crystallography (MX) structure determination.[2] More than 70% of all structures in the protein structure data bank were determined using synchrotron radiation as the primary source,[3] with recent structures approaching 100%. X-ray absorption spectroscopy (XAS) complements MX by determining local radial structural information on samples without the need for crystallization. XAS is even more dependent upon synchrotron radiation than MX, with synchrotron radiation providing the only practical X-ray source for most XAS applications.

While the well-established field of radiation chemistry has been known since the pioneering works of Becquerel and Curie, in recent years, due to the remarkable increase in brightness of synchrotron radiation sources, X-ray-induced photochemical changes in samples are of growing concern.[4] In particular, transition metal ions within metalloproteins tend to be highly susceptible to X-ray induced photoreduction.[4] Indeed, the redox active nature of metalloprotein active sites, a property closely related to their function, often results in the transition metal ions being prone to photoreduction. With MX the extent of photoreduction can often go undetected, whereas with XAS the near-edge portion of the spectrum is sensitive to electronic structure such that photoreduction of metal sites can often be observed directly through progressive changes in successive individual spectra.[4]

Alcohols and ethers are very widely used in preparation of both MX and XAS metalloprotein samples. Cryoprotectants such as the polyether polyethyleneglycol (PEG) are routinely added to MX samples to protect delicate protein crystals from damage upon freezing. For XAS, glassing agents such as glycerol (propane-1,2,3-triol) are often added to prevent spectroscopic artifacts arising from X-ray diffraction by crystalline ice. Herein we show that alcohol and ether based cryoprotectants are directly responsible for a remarkable exacerbation of sample photoreduction occurring through irradiation with X-rays. We used Cu K-edge XAS, a sensitive probe of Cu oxidation state, to monitor photoreduction of a simple model system, aqueous Cu(II), with the X-ray beam both inducing photochemistry and deducing its rate through repeat spectra.

4.6 Materials and Methods

4.6.1 Experimental Procedures

Cu K-edge XAS measurements were carried out at the Stanford Synchrotron Radiation Lightsource (SSRL) using the structural molecular biology XAS beam line 7-3 because this beamline was designed to specifically cater for solution samples of biological molecules, especially those that are prone to X-ray induced photochemistry. Harmonic rejection was accomplished by setting the mirror pitch to give an energy cutoff of 12 keV. Incident and transmitted X-rays were monitored using nitrogen-filled gas ionization chambers employing a sweeping voltage of 1,600 V, and X-ray absorption was measured as the primary fluorescence excitation spectrum using an array of 30 germanium detectors [5] (Canberra Ltd. Meriden, CT, USA). All reagents were purchased from Sigma-Aldrich (Oakville, ON) and were of the highest quality available. Solution samples, prepared by dissolving anhydrous $CuCl_2$ in deionized water, were loaded into 2 mm path-length poly-acetal cuvettes closed with a mylar tape window and were frozen by immersion into a partly-frozen isopentane slurry at a temperature of ~140 K. Samples were transported and stored at liquid nitrogen temperatures until data acquisition. During XAS measurements, samples were maintained at a temperature of 10 K using a helium flow cryostat (Oxford instruments, Abingdon, UK). Data were collected using the XAS Collect data acquisition software.[6] The XAS scan rate was chosen to be rapid relative to the rate of observed changes, while still having adequate signal to noise with sufficient data range for normalization and background removal. The time of each scan was taken to be the time stamp of the point at the onset of the structured region of the near-edge spectrum at around 8983 eV, 1 min. after the experimental scans were started, with the time to complete the scan taking an additional 4 min. Data reduction and analysis employed the exafspak[7] suite of computer programs and was carried out as previously described.[8] The incident beam intensity was varied by inserting aluminum metal filters of appropriate thickness. Electron paramagnetic resonance (EPR) spectra were measured on samples contained in XAS cuvettes before and after exposure to the X-ray beam, using an RE1X spectrometer (JEOL, Peabody, MA, USA) spectrometer located near to the beamline.

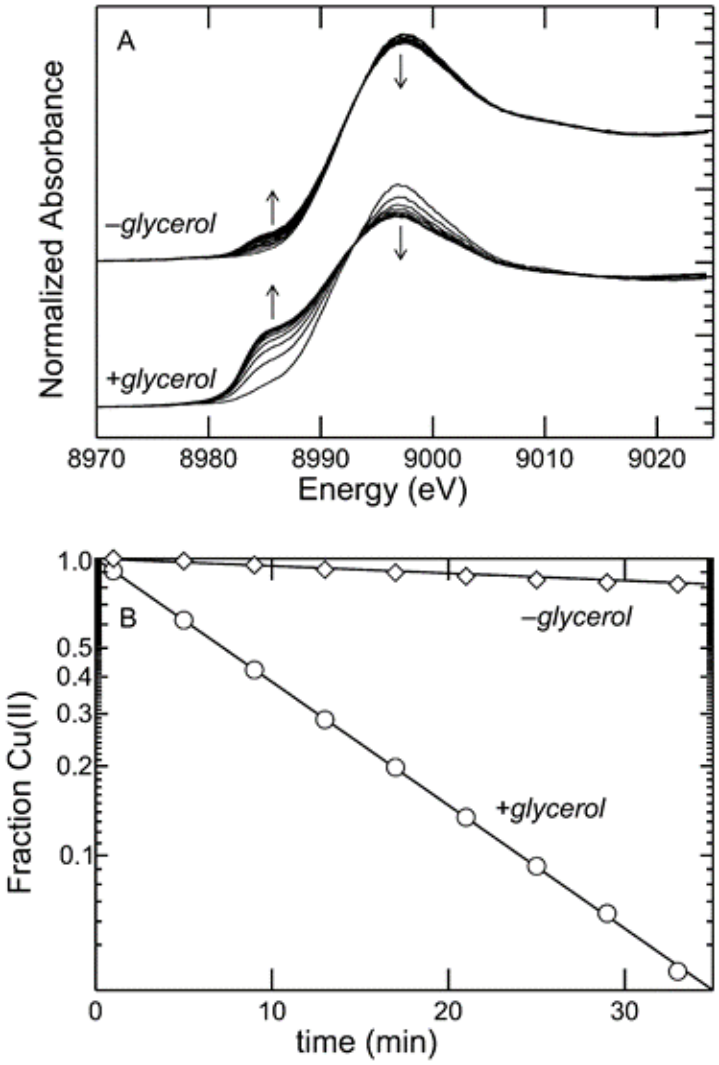

Figure 4.1 Effects of glycerol upon the kinetics of X-ray induced Cu(II) photoreduction. A. Comparison of sequential Cu K-edge X-ray absorption near-edge spectra of 2 mM $CuCl_2$ showing progressive changes in the spectra with time with and without glycerol. Arrows indicate the direction of the changes with time. B. Kinetic analysis of the data from Figure 4.1A, showing pseudo first-order rates according to $\frac{[\mathrm{Cu(II)}]}{[\mathrm{Cu}]} = e^{-k_{eff}t}$ where k_{eff} is the pseudo first-order rate constant, t is time and [Cu(II)] and [Cu] are the concentrations of oxidized and total copper, respectively.

4.7 Results and Discussion

Figure 4.1 A shows the progression of X-ray-induced changes in the X-ray absorption spectrum (XAS) of an aqueous solution of $CuCl_2$ with and without 25% v/v glycerol. XAS can readily distinguish the spectra of Cu(II) and Cu(I) species,[9] and the progressive photo-reduction from the initial Cu(II) to Cu(I) is clearly apparent. The Cu(II) form shows spectroscopic features typical of an effectively square planar coordination, characterized by an intense feature on top of the rising part of the edge at 8997 eV, attributable to 1s→4p transitions,[10] and a very weak feature at 8978.7 eV arising from a 1s→3d transition. The Cu(I) form in contrast is characteristic of trigonal planar coordination[9] with a lower intensity at 8997 eV and a pronounced shoulder at 8985 eV which is due to a $1s \rightarrow 4p_z$ transition.[8] The data shown in Figure 4.1 clearly indicate that the rate of photoreduction is markedly increased in the presence of glycerol (Table 4.1). Analysis of the kinetics in the presence and absence of glycerol is shown in Figure 4.1 B. Spectra in the two time series were fit to a linear combination of the two end members, specifically the first sweep of the glycerol-free series corresponding to a nearly pure Cu(II) spectrum, and the last sweep of the glycerol series corresponding to a nearly pure photoreduced Cu(I) species. The analysis shows pseudo first-order kinetics, with effective first-order rate constants k_{eff} of 0.4 and 5.7 hr^{-1} ($t_{½}$=104 and 7.3 min) in the absence and presence of glycerol, respectively; a more than 10-fold increase in the rate of photoreduction due to the presence of glycerol. The possible role of photoelectrons arising from Cu K-edge excitation was investigated by irradiating two different samples for 20 min. one below (8900 eV) and one above (8997 eV) the absorption edge, and then examining the extent of photoreduction by scanning an XAS sweep. No significant differences were observed, indicating that, as expected for a dilute solution, photoelectrons generated by Cu K-edge excitation play only a subtle role.

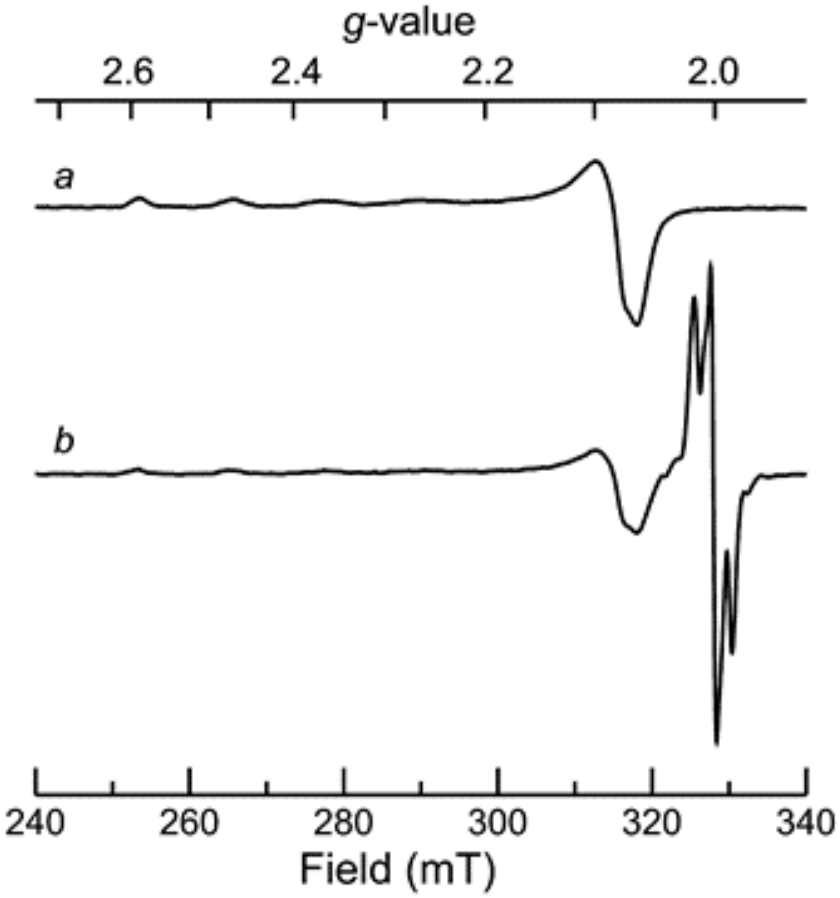

Figure 4.2 Electron Paramagnetic Resonance (EPR) spectra of the sample of Figure 4.1 before and after X-ray irradiation. *a*: Spectrum of 2 mM Cu(II) in the presence of 25% v/v glycerol before X-ray irradiation, a typical Cu(II) EPR spectrum. *b*: Spectrum following X-ray irradiation through collection of the data of Figure 4.1. The Cu(II) EPR signal is decreased in intensity; an additional anisotropic EPR signal at $g \approx 2.0$, characteristic of a free radical, can be seen.

Figure 4.2 shows the EPR spectra of the sample of Figure 4.1 before and after irradiation with X-rays. The characteristic S=½ EPR signal of $3d^9$ Cu(II) observed in the pre-irradiation sample is substantially decreased in the post-irradiation sample, consistent with conversion to EPR-silent $3d^{10}$ Cu(I). Residual Cu(II) EPR signal in the irradiated sample is most likely from the approximately 50% of the total sample within the cuvette that was not illuminated by the X-ray beam. An additional large free radical signal at g≈2 observed in the irradiated sample is also observed in EPR of irradiated empty cuvettes and is attributable, at least in part, to irradiated plastic. The decrease in Cu(II) EPR signal intensity confirms our XAS results showing photoreduction of Cu(II) to Cu(I).

As expected for pseudo first-order kinetics the value for k_{eff} was essentially independent of the initial concentration of Cu(II) in solution (Table 4.2). Similarly to glycerol, enhancements in the rate of photoreduction were observed with the alternative cryoprotectants, PEG and ethanediol (Table 4.1), with magnitudes in the order PEG < glycerol < ethanediol. Systematic attenuation of the X-ray beam (Table 4.2) showed that k_{eff} was directly proportional to the photon flux density, expressed as photons$\cdot s^{-1}\cdot mm^{-2}$. The exacerbation of photoreduction of Cu(II) is not dependent upon any prospective coordination of the metal ion by the cryoprotectant because we observe that the effects are not abrogated when Cu(II) ethylenediaminetetraacetic acid (EDTA) is employed (data not shown).

Photolysis in samples containing water is relatively well understood,[11, 12, 13] the major products being solvated electrons (e^-_{aq}) and hydroxyl radicals (OH•), which are generated according to eqn. (1) and (2),[12, 14] along with other minor species including hydrogen peroxide. Among these products, solvated electrons are likely most relevant to photoreduction.[14, 16]

Our samples also contain an appreciable fraction (ca. 25% v/v) of alcohol or ether, and, at least in the case of alcohols radiolysis of these compounds can also form solvated electrons.[17] For simplicity the present discussion is restricted to water.

$$H_2O + h\nu \rightarrow H_2O^+ + e^-_{aq} \quad (4.1)$$

$$H_2O^+ \rightarrow H^+ + HO\bullet \quad (4.2)$$

Table 4.1 Effect of cryoprotectant type on the kinetics of Cu(II) photoreduction in aqueous solution[a]

Cryoprotectant	k_{eff} (hr^{-1})[b]
None	0.40(2)
glycerol	5.7(1)
PEG 6000	3.4(1)
ethanediol	6.4(1)

[a] For these experiments, estimated flux density is 4.57×10^{11} photons·s^{-1}·mm^{-2}, Cu concentration was 2 mM (final) and cryoprotectants were added to 25% v/v final concentration.

[b] Pseudo first-order rate constant. Estimated standard deviations in the last digits of the values are given in parentheses.

Hydroxyl radicals act as oxidizing agents while the hydrated electrons are potent reductants; both are highly reactive. Both also are highly mobile,[18] even in frozen solution, and can spontaneously recombine in the reverse reactions to reform water and heat.[14] The alcohol-based cryoprotectants studied here are well known hydroxyl radical scavengers;[19] the hydroxyl radical is thought to react by abstracting carbon-bound hydrogen to form water and carbon-centered radicals as major products, which are regarded as reducing species.[20] Vicinal diols, such as most alcohol-based cryoprotectants, are thought to be particularly effective hydroxyl radical scavengers due to elimination of additional water:[21]

$$HO\bullet + CH_3OH \rightarrow \bullet CH_2OH + H_2O \qquad (4.3)$$

Ethers are also known to react readily with hydroxyl radicals, through hydrogen abstraction through C–H bond breakage and formation of carbon-centered free radicals.[22, 23] The presence of these highly effective hydroxyl radical scavengers thus is expected to remove oxidizing equivalents by sequestering hydroxyl radicals, leaving an excess of hydrated electrons. As previously discussed,[4,12] hydrated electrons are extremely potent and highly mobile reductants, which would be available to reduce the Cu(II) in our experiments, or other redox-active components that may be present in other samples. Additionally, the products of hydroxyl radical scavenging are also potent reductants,[20, 24, 25] and may also directly reduce Cu(II) in our experiments.

Kinetic data on the rate of production of hydrated electrons is not observable from our experiments but other work has shown this to be on the picosecond or shorter timescale: the reactions of eq. 4.1 and 4.2 are expected to proceed very rapidly indeed,[13] and the reaction of hydroxyl radicals with cryoprotectants is also expected to be fast relative to the timescales of our experiment.[26] In agreement with these expectations, our data on varying the photon flux density suggest that the production and breakdown of hydrated electrons has reached a kinetic steady-state, with only a minor perturbation caused by the photoreduction of Cu(II) in the sample. Thus, under steady-state conditions varying the photon flux density will be

reflected by a change in the steady-state level of hydrated electrons, with k_{eff} being proportional to the flux density, as indeed we observe (Table 4.2).

The implications of these results are important for a large number of studies. The use of poly-ether cryoprotectants in protein crystallography is extremely widespread, with polyols having broad use in XAS as glassing agents. Photoreduction also appears to be prevalent and, as discussed above, often goes unnoticed by experimenters.[4] In some cases, such as the XAS of Cu(II)-bound amyloid β, the only published XAS data appears to be of partly or wholly photoreduced samples.[27] Moreover, as we have previously noted, photoreduction and chemical reduction of metal sites in proteins may result in different structures. Thus, for prion peptide samples with copper bound, we have shown that Cu(II) has the expected four-coordinate square-planar type geometry, and that chemical reduction with ascorbate gives a linear digonal Cu(I) site, whereas XAS of X-ray photoreduced samples is only consistent with three-coordinate approximately trigonal-planar Cu(I) geometry.[28] Similarly, X-ray irradiation of Fe(III) *met*-myoglobin with the high photon flux densities of a modern XAS beamline gives a metastable photoreduced Fe(II) site that is distinct from normal deoxy Fe(II) myoglobin. [4] In this case substantial photoreduction to the metastable Fe(II) state occurred ahead of the first XAS sweep reaching the structured part of the spectrum which was only detectable by comparison with XAS data from a lower flux-density beamline.[4]

Table 4.2 Effect of copper concentration and photon flux density on the kinetics of Cu(II) photoreduction in aqueous solutions

Cu-concentration[b]		Flux density[c]	
mM	k_{eff} (hr^{-1})[d]	photons· $s^{1}·m^{-2}$	k_{eff} (hr^{-1})[d]
0.25	5.8(1)	3.97×10^{11}	4.9(1)
0.5	5.7(1)	2.02×10^{11}	2.5(1)
2.0	5.7(1)	0.97×10^{11}	1.5(1)

[a] All experiments were done in the presence of 25% v/v glycerol.

[b] Estimated flux density was 4.57×10^{11} photons·s^{-1}·mm^{-2}.

[c] Copper concentration was 2 mM. This series was measured at a different time with slightly lower peak flux density.

[d] Pseudo first-order rate constant. Estimated standard deviations in the last digits of the values are given in parentheses.

The methods that are used to protect XAS samples against photoreduction have recently been reviewed[4] and include such measures as moving the sample so that the beam interrogates a fresh part of the sample with each sweep, and using photon shutters to ensure that the sample is only exposed when data collection is active. An alternative to using alcohol-based glassing agents in XAS is to freeze the sample sufficiently rapidly that diffracting ice crystals cannot form. Freezing in liquid nitrogen is slow because of the Leidenfrost effect in which a cushion of vapor insulates the sample from direct contact with the cryogen. Although much more rapid freezing can be obtained by using a cryogen for which the sample temperature is below the Leidenfrost point, such as a partly-frozen slurry of isopentane at about 120 K, this method does not always fully protect against ice diffraction artifacts. Diffraction artifacts in XAS occur when energy dispersive solid-state detectors, used to detect the X-ray fluorescence, become count-rate saturated when struck with a diffracted beam. The use of high resolution crystal analyzers[29] to monitor X-ray fluorescence and measure XAS should reliably abrogate diffraction artifacts, although such detector optics are specialized and are not a standard part of most XAS experiments.

With MX the use of cryoprotectants such as PEG is important for obtaining the high resolution structures that are the foundation of modern structural molecular biology. Our results show that these same cryoprotectants may be responsible for unwanted photochemistry that could lead to erroneous active site structures of metalloproteins. Many proteins contain additional redox-active groups, such as disulfide linkages, or other redox-active cofactors (e.g. flavins, molybdopterin or ubiquinone) which may likewise be susceptible to photoreduction. MX beamlines typically have small focused beams and hence can have around 500 fold higher flux densities than the XAS beamline that we employed here. Extrapolating from Table 4.2 we predict that for MX beamlines $t_{½}$ could approach 1 second for our Cu(II) system in the presence of glycerol. Protein crystals have high water contents, although lower than the aqueous solutions we employed in our experiments which should mitigate this extreme rate somewhat, but this calculation serves to illustrate that exacerbation of photoreduction rates by the cryoprotectant will be an issue in many cases. Photoreduction in metalloproteins may also be exacerbated due to Auger electrons and decay products thereof, arising from photoexcitation of elements such as Ca and Mg present as divalent ions in the sample.[30] X-ray irradiation can also generate free radicals by interacting

with the protein itself, leading to more complex reactions, and will be the subject of future work.

There is much recent interest in diffraction using pulsed X-rays from free electron lasers (FEL), such as the linear coherent light source (LCLS), which can generate X-ray pulses of femtosecond duration with extremely high intensity.[31] While the sample is destroyed following exposure to the X-ray pulse, any degradation during the duration of the pulse is thought to be negligible and hence observed diffraction is thought to have been generated by a pristine sample.[32] While the simple photoreduction kinetics presented here will may not be applicable at such short time scales, a possibly invalid but trivial extrapolation of our experiments suggests that at the flux densities of a typical LCLS pulse, $t_{½}$ should be around a femtosecond, or shorter than the FEL pulse length. However, although direct reduction by photoelectrons may be a problem[30] the FEL pulse length is sufficiently short that it may overcome the rate of photochemical generation of hydrated electrons and their mobility.[31] Thus, whether or not photoreduction is a problem for FEL diffraction data remains an open question.

In summary, our results show that in our simple model system addition of cryoprotectants intended to enhance X-ray measurements, whether improving the resolution of MX or reducing background scatter for XAS, may significantly exacerbate photoreduction of redox active transition metal ions in the sample. This may lead to erroneous conclusions concerning the active site structure and correspondingly incorrect deductions concerning the catalytic mechanism. In light of our results, it seems prudent to revisit the widespread use of alcohol or ether cryoprotectants in X-ray measurements.

REFERENCES

1) Phillips, J. C.; Wlodawer, A.; Yevitz, M. M.; Hodgson, K. O. Applications of synchrotron radiation to protein crystallography: preliminary results. *Proc. Natl. Acad. Sci. USA*, **1976**, *73*, 128–132.

2) Dauter, Z.; Jaskolski, M.; Wlodawer, A. Impact of synchrotron radiation on macromolecular crystallography: A personal view. *J. Synchrotron Radiat*. **2010**, *17*, 433–444.

3) Berman, H. M.; Westbrook, J.; Feng, Z.; Gilliland, G.; Bhat, T. N.; Weissig, H.; Shindyalov, I. N.; Bourne, P. E. The Protein Data Bank. *Nucleic Acids Res*. **2000**, *28*, 235–242.

4) George, G. N.; Pickering, I. J.; Pushie, M. J.; Nienaber, K.; Hackett, M. J.; Ascone, I.; Hedman, B.; Hodgson, K. O.; Aitken, J. B.; Levina, A.; Glover, C.; Lay, P. A. X-ray Induced Photo-Chemistry and X-ray Absorption Spectroscopy of Biological Samples. *J. Synchrotron Radiat*. **2012**, *19*, 875–886.

5) Cramer, S. P.; Tench, O.; Yocum M.; George. G. N. A 13-element Ge Detector for Fluorescence EXAFS. *Nucl. Instr. Meth. A*. **1988**, *266*, 586–591.

6) George, M. J. XAS-Collect: A Computer Program for X-ray Absorption Spectroscopic Data Acquisition. *J. Synchrotron Radiat*. **2000**, *7*, 283–286.

7) George, G. N. **2000**, http://www-ssrl.slac.stanford.edu/exafspak.html

8) George, G. N.; Garrett, R. M.; Prince, R. C.; Rajagopalan, K. V. The Molybdenum Site of Sulfite Oxidase: A Comparison of wild-type and the cysteine 207 to serine mutant using X-ray absorption spectroscopy. *J. Am. Chem. Soc*. **1996**, *118*, 8588–8592.

9) Kau, L. S.; Spira-Solomon, D.; Penner-Hahn, J. E.; Hodgson K. O.; Solomon, E. I. X-ray absorption edge determination of the oxidation state and coordination number of copper. Application to the Type 3 Site in *Rhus vernicifera* Laccase and its reaction with oxygen. *J. Am. Chem. Soc*. **1987**, *109*, 6433–6442.

10) Pickering, I. J.; George, G. N. Polarized X-ray Absorption of cupric chloride dihydrate. *Inorg. Chem*. **1995**, *34*, 3142–3152.
11) Gunter, T. E. Electron paramagnetic resonance studies of the radiolysis of H_2O in the solid state. *J. Chem. Phys*. **1967**, *46*, 3818–3829.
12) Garrett, B. C.; Dixon, D. A.; Camaioni, D. M.; Chipman, D. M.; Johnson, M. A.; Jonah, C. D.; Kimmel, G. A.; Miller, J. H.; Rescigno, T. N.; Rossky, P. J. Role of water in electron-initiated processes and radical chemistry: Issues and scientific advances. *Chem. Rev*. **2005**, *105*, 355–390.
13) El Omar, A. K; Schmidhammer, U.; Jeunesse, P.; Larbre, J.-P.; Lin, M.; Muroya, Y.; Katsumura, Y.; Pernot P.; Mostafavi, M. Time-Dependent radiolytic yield of OH· radical studied by picosecond pulse radiolysis. *J. Phys. Chem. A.* **2011**, *115*, 12212–12216.
14) Buxton, G. V.; Greenstock, C. L.; Helman, W. P.; Ross, A. B. Critical review of rate constants for reactions of hydrated electrons, hydrogen atoms and hydroxyl radicals (·OH/·O^-) in aqueous solution. *J. Phys. Chem. Ref. Data*, **1988**, *17*, 513–886.
15) Kevan, L. Solvated electron structure in glassy matrixes. *Acc. Chem. Res*. **1981**, *14*, 138–145.
16) Marsalek, O.; Uhlig, F.; VandeVondele, J.; Jungwirth, P. Structure, dynamics, and reactivity of hydrated electrons by *ab initio* molecular dynamics. *Acc. Chem. Res*. **2012**, *45*, 23–32.
17) Bonin, J.; Lampre, I.; Pernot, P.; Mostafavi, M. Solvation Dynamics of Electron Produced by two-photon ionisiation of liquid polyols III. glycerol. *J. Phys. Chem. A.* **2008**, *112*, 1880–1886.
18) Codorniu-Hernandez E.; Kusalik, P. G. Mobility mechanism of hydroxyl radicals in aqueous solution via hydrogen transfer. *J. Am. Chem. Soc*. **2012**, *134*, 532–538.
19) Billany, M. R.; Khatib, K.; Gordon, M.; Sugden, J. K. Alcohols and ethanolamines as hydroxyl radical scavengers. *Int. J. Pharm*. **1996**, *137*, 143–147.
20) Wang, W.-F.; Nien Schuchmann, M.; Bachler, V.; Schuchmann, H.P.; von Sonntag, C. Termination of ·CH_2OH/$CH_2O^{\cdot -}$ radicals in aqueous solution. *J. Phys. Chem*. **1996**, *100*, 15843–15847.

21) Jiang, D.; Barata-Vallejo, S.; Golding, B. T.; Ferrerib C.; Chatgilialoglu, C. Revisiting the reaction of hydroxyl radicals with vicinal diols in water. *Org. Biomol. Chem.* **2012**, *10*, 1102–1107.
22) Schuchmann, M. N.; von Sonntag, C. Hydroxyl radical induced oxidation of diethyl ether in oxygenated aqueous solution. A product and pulse radiolysis study. *J. Phys. Chem.*, **1982**, *86*, 1995–2000.
23) Bänsch, C.; Kiecherer, J.; Szöri, M.; Olzmann, M. Reaction of Dimethyl Ether with Hydroxyl Radicals: Kinetic Isotope Effect and Prereactive Complex Formation *J. Phys. Chem. A.* **2013**, *117*, 8343–8351.
24) Toigawa, T.; Gohodo, M.; Norizawa, K.; Kondoh, T.; Kan, K.; Yang, J.; Yoshida, Y. Examination of the formation process of pre-solvated and solvated electron in *n*-alcohol using femtosecond pulse radiolysis. *Radiat. Phys. Chem.* **2016**, *123*, 73–78.
25) Mostafavi, M.; Dey, G. R.; François, L.; Belloni, J. Transient and stable silver clusters induced by radiolysis in methanol. *J. Phys. Chem. A.* **2002**, *106*, 10184–10194.
26) Sun, C.; Lv, L.; Zhang, S. Theoretical Investigation on the Reaction Mechanism and Kinetics of Benzyl Alcohol with ·OH Radical. *Theor. Chem. Acc*. **2016**, *135*, 51.
27) Shearer, J.; Szalai, V. A. The Amyloid-β Peptide of Alzheimer's Disease Binds CuI in a Linear bis-His Coordination Environment: Insight into a Possible Neuroprotective Mechanism for the Amyloid-β Peptide. *J. Am. Chem. Soc*. **2008**, *130*, 17826–17835.
28) McDonald, A.; Pushie, M. J.; Millhauser, G. L.; George, G. N. New insights into metal interactions with the prion protein: EXAFS analysis and structure calculations of copper binding to a single octarepeat from the prion protein. *J. Phys. Chem. B.* **2013**, *117*, 13822–13841.
29) Alonso-Mori, R.; Kern, J.; Sokaris, D.; Weng, T.C.; Norldlund, D.; Tran, R.; Montanez, P.; Delor, J.; Yachandra, V. K.; Yano, J.; Bergmann, U. A multi-crystal wavelength dispersive X-ray spectrometer. *Rev. Sci. Instrum*. **2012**, *83*, 073114
30) Stumpf, V.; Gokhberg, K.; Cederbaum, L. S. The role of metal ions in X-ray-induced photochemistry. *Nature Chem*. **2016**, *8*, 237–241.

31) Pardini, T.; Aquila, B.; Boutet, S.; Cocco, D.; Hau-Riege, S. P. Numerical simulations of the hard X-ray pulse intensity distribution at the Linac Coherent Light Source. *J. Synchrotron Radiat*. **2017**, *24*, 738–743.
32) Hunter, M. S.; Segelke, B.; Messerschmidt, M.; Williams, G. J.; Zatsepin, N. A.; Barty, A.; Benner, W. H.; Carlson, D. B.; Coleman, M.; Graf, A.; Hau-Riege, S. P.; Pardini, T.; Seibert, M. M.; Evans, J.; Boutet S.; Frank. M. Fixed-Target protein serial microcrystallography with an X-ray Free Electron Laser. *Sci. Rep*. **2014**, *4*, 6026-6031.

5. X-ray Induced Photoreduction of Hg(II) in Aqueous Frozen Solution Yields Nearly Monatomic Hg(0)

5.1 Preface

Experiments conducted and described in Chapter 4, examined the photoreduction of copper (II) in samples containing various cryoprotectants. Having considered the alarming increase in photodamage observed in these photoreduction experiments, measures were introduced to ameliorate photodamage in other experiments carried out during synchrotron techniques. Samples containing mercury (II) were believed to be safe from photoreduction processes and thus were produced with glycerol included as a cryoprotectant. When photoreduction was observed in mercury (II) samples with glycerol as a cryoprotectant, a separate series of experiments were conducted to examine a chemically interesting Hg(0) species.

5.2 Manuscript Author Contributions

This chapter was published in Inorganic Chemistry and was reformatted to follow the guidelines for a manuscript style thesis.

X-ray-Induced Photoreduction of Hg(II) in Aqueous Frozen Solution Yields Nearly Monatomic Hg(0). Kurt H. Nienaber, Susan Nehzati, Julien J. H. Cotelesage, Ingrid J. Pickering, and Graham N. George. *Inorg. Chem.*, **2018**, *57* (14), 8205–8210

Kurt Nienaber took primary responsibility for initial mercury (II) experiment design, data collection and analysis, and manuscript drafting. Susan Nehzati and Julien J. H. Cotelesage assisted in sample preparation and data collection. Ingrid J. Pickering aided in experimental setup and manuscript editing. Graham N. George aided in experimental setup, and manuscript drafting and editing.

5.3 Acknowledgements

We thank Prof. Anne Summers of the University of Georgia, for providing the samples in which we initially observed photoreduction of Hg(II). This work was supported by Discovery Grants from the Natural Sciences and Engineering Research Council of Canada (NSERC, IJP

and GNG), an Innovation and Science Fund of Saskatchewan (IJP), a Canada Foundation for Innovation John Evans Leader's Fund award (IJP) and by Canada Research Chairs (IJP and GNG). KHN was funded by the Gene Expression Mapping using Synchrotron Light group grant from the Saskatchewan Health Research Foundation (Nichol, group leader) and SN acknowledges the Dr. Rui Feng Scholarship. KHN and SN were Fellows in the Canadian Institutes of Health Research-Training grant in Health Research Using Synchrotron Techniques (THRUST). Use of the Stanford Synchrotron Radiation Lightsource, SLAC National Accelerator Laboratory, is supported by the U.S. Department of Energy, Office of Science, Office of Basic Energy Sciences under Contract No. DE-AC02-76SF00515. The SSRL Structural Molecular Biology Program is supported by the DOE Office of Biological and Environmental Research, and by the National Institutes of Health, National Institute of General Medical Sciences (including P41GM103393). The contents of this publication are solely the responsibility of the authors and do not necessarily represent the official views of NIGMS or NIH.

5.4 Abstract

Here we use X-ray induced photochemistry, which is well-known to cause changes in a number of systems, to reduce Hg(II) to Hg(0) in frozen aqueous solution with added glycerol maintained at 10K. X-ray absorption spectroscopy was used to monitor the extent of the reaction and to characterize the species. Analysis of the extended X-ray absorption fine structure (EXAFS) of the photochemical product indicated a nearly monatomic Hg(0) species bound only by long weak bonds to oxygens at ~3.5 Å. The results of the EXAFS analysis agree quantitatively with the results of density functional theory calculations, using the meta-GGA approximation with the M11-L functional. This is the first structural characterization of nearly monatomic Hg(0) bound by hard ligands, similar to those expected in environmental systems. We conclude that Hg(0) is expected to exist in solution as a nearly monatomic entity.

5.5 Introduction

Structures of mononuclear zero-valent mercury (Hg(0)) complexes are not common in the chemical literature. A search of the Cambridge Structure Database shows only six different structures, in contrast with 3,181 structures of Hg^{2+} compounds.[1] The few Hg(0) complexes that have been characterized do show some common structural features. In some, Hg(0) is part of an electron-rich transition metal ion chalcogenide cluster,[2, 3] while in others Hg(0) is bound between two phosphine-coordinated Pt(0),[4] or by iodide and Mo(0),[5] or is trapped in a gold(I) metallocryptand cage complex with two metal-metal bonds.[6] In all cases thus far reported the Hg(0) is diffusely bound by very long and weak bonds to the coordinating atoms. In no cases have complexes with hard ligands such as oxygen been reported.

Elemental mercury is important in the environment, both as a primarily monatomic Hg(0) vapor in emissions from the burning of fossil fuels such as coal, and in aqueous solution where it is also presumed to be monatomic Hg(0) as part of the biogeochemical mercury cycle.[7] Elemental mercury is unusual among metals in being slightly soluble in water, with a reported maximum solubility of 0.7 μM,[8] which is of pivotal importance in its roles in the biogeochemical mercury cycle. Elemental mercury owes its unique properties to its electronic configuration; the $6s^2$ valence electrons are heavily impacted by relativistic effects and poorly screened from the nuclear charge by the filled 4f level. As a consequence, elemental mercury is reluctant to form strong bonds, resulting in its unusual liquid phase at room temperature, its presumed monatomic nature in aqueous solution, and its primarily monatomic vapor phase. Indeed, Hg(0) is the only element apart from the noble gases to be essentially monatomic in the vapor phase, while many metals form diatomic vapors.[9] Vapor phase Hg(0) from mercury amalgam dental restoratives is also a primary source exposure for human populations, because monatomic vapor phase Hg(0) is rapidly absorbed to blood via the lung, where it is oxidized to Hg(II).[10] Mercury is also present in the organic milieu of crude oil,[11] where it is again presumed to be present as solutions of Hg(0). Although the levels in crude oils are low it poses substantial problems for refiners in terms of equipment degradation, potential industrial worker health impacts, downstream poisoning of catalysts and toxic waste generation.

Photochemical modification of samples in X-ray absorption spectroscopy (XAS) is a well-recognized problem,[12] which has recently been exploited in order to study species of chemical interest.[13] Recently, we reported that addition of alcohol or polyether-based cryoprotectants leads to an increase by more than an order of magnitude in the rate of photoreduction of Cu(II) in a model system.[14] Photolysis of water very rapidly yields hydroxyl radicals (OH•) and hydrated electrons (e^-_{aq}), which subsequently can recombine to reform water and heat, or react with other components in solution. The increase in rate of photoreduction arises from the cryoprotectants acting as hydroxyl radical scavengers, which leaves an excess of highly-reducing hydrated electrons available to reduce other redox-active species in solution,[14] such as Cu(II) to Cu(I).[14] In preliminary XAS studies of solutions of Hg(II) compounds we observed shifts in the Hg L_{III} near-edge spectra that are characteristic of photoreduction. Here, we employ X-ray induced photoreduction, potentiated by a cryoprotectant, to produce Hg(0) complexes in frozen solution at concentrations that are suitable for structural study using XAS. The XAS results show a nearly monatomic Hg(0) species with long Hg–O bonds at 2.9–3.6 Å, which compares well with the results of density functional theory calculations.

5.6 Materials and Methods

5.6.1 Sample Preparation

Reagents were purchased from Sigma-Aldrich (Oakville, ON) and were of the highest quality available. Aqueous solutions of mercuric acetate with 25% v/v glycerol were loaded into 2 mm path-length poly-acetal cuvettes closed with a mylar tape window and then frozen by immersion into a partly-frozen isopentane slurry with a temperature of approximately 120 K. Samples were transported and stored at liquid nitrogen temperatures until data acquisition. A sample of elemental mercury suitable for X-ray spectroscopic measurements was precipitated from 1 mM aqueous $HgCl_2$ solution by reduction with a slight excess of sodium borohydride. The resulting gray-milky solution was then rapidly frozen prior to any mercury mirror formation by immersion into a partly-frozen isopentane slurry, followed by spectroscopic examination.

5.6.2 X-ray Absorption Spectroscopy

XAS measurements were carried out at the Stanford Synchrotron Radiation Lightsource (SSRL) using the structural molecular biology XAS beamlines 7-3 and 9-3 with the SPEAR3 storage ring containing 500 mA at 3.0 GeV. Both 7-3 and 9-3 are equipped with a rhodium-coated vertical collimating mirror upstream of a Si(220) double crystal monochromator with $\phi = 90°$. Harmonic rejection was accomplished by setting the mirror pitch to give an energy cutoff of 15 keV. Incident and transmitted X-rays were monitored using nitrogen-filled gas ionization chambers employing a sweeping voltage of 1,600 V, while X-ray absorption was measured as the primary fluorescence excitation spectrum using an array of 30 germanium detectors[15] on 7-3 and a 100 pixel Ge Monolith on 9-3 (Canberra Ltd. Meriden, CT, USA). In order to maintain detector count-rates in the pseudo-linear regime, Ga_2O_3 X-ray filters were employed to preferentially absorb scattered radiation, together with silver Soller slits (EXAFS Co., Pioche Nevada) to reject filter fluorescence. Data were collected using the XAS Collect data acquisition software,[16] with samples maintained at a temperature of 10 K using a helium flow cryostat (Oxford instruments, Abingdon, UK). Energy calibration of the monochromator was relative to the lowest-energy inflection of the Hg L_{III} edge spectrum of an Hg-Sn amalgam foil, which was assumed to be 12285.0 eV. Data reduction and analysis and was carried out as previously described[17] using the exafspak suite of computer programs.[18] Extended X-ray absorption fine structure (EXAFS) phase and amplitude functions were calculated using the program FEFF.[19,20]

5.6.3 Density Functional Theory (DFT) Calculations

DFT geometry optimizations were carried out using DMol^3 and Biovia Materials Studio Version 2017 R2[21,22] using the meta-GGA approximation employing the M11-L functional both for the potential during the self-consistent field procedure, and for the energy.[23] DMol^3 double numerical basis sets included polarization functions for all atoms with all-electron relativistic core treatments. Environmental effects were modeled using the Conductor-like Screening Model (COSMO)[24] in DMol^3, with a dielectric value representing water with 25% glycerol ($\varepsilon = 69.53$).

5.7 Results and Discussion

5.7.1 X-ray Absorption Spectroscopy

Figure 5.1 shows the progressive changes with time in X-ray absorption near-edge spectra of two samples of mercuric acetate measured on beamlines 7-3 and 9-3. These two beamlines differ substantially in terms of X-ray flux density, estimated for these experiments to be 4.0×10^{11} and 3.0×10^{12} photons/sec/mm^2 on 7-3 and 9-3, respectively. For photoreduction of frozen aqueous solutions of Cu(II) to Cu(I) we have reported that the rate is directly proportional to the photon flux density.[14] Allowing for this, the data from 9-3 are consistent with those from 7-3, with the more rapid changes on 9-3 arising from the substantially higher X-ray photon flux density (the first 9-3 sweep approximately corresponds to the 9th sweep from 7-3). The clear changes with time are indicative of photochemical changes to the state of mercury of the sample. Principal component analysis (PCA) with examination of the Malinowski indicator function[25] suggests that three components may be present, plausibly the initial material, the final product and an intermediate. The third principal component is, however, small and the data series can nearly be reconstituted with just the first two eigenvectors, suggesting only small amounts of any intermediate. In agreement with this, examination of the electron paramagnetic resonance (EPR) showed the free radicals that we have described previously[14] plus an additional weak signal near $g\approx2$ that might be due to small amounts of mononuclear paramagnetic 6s^1 Hg(I).[26] After 6 hours irradiation on 9-3, incremental sweeps become essentially invariant showing that the photochemical reaction has approached completion to yield the final photoreduced product; an average of the last three invariant sweeps is shown in Figure 5.2. This final endmember spectrum is compared with that of a sample with minimal photochemical changes, obtained on beamline 7-3 by translating the sample relative to the X-ray beam and using relatively rapid scans so that fresh sample is irradiated with each sweep.

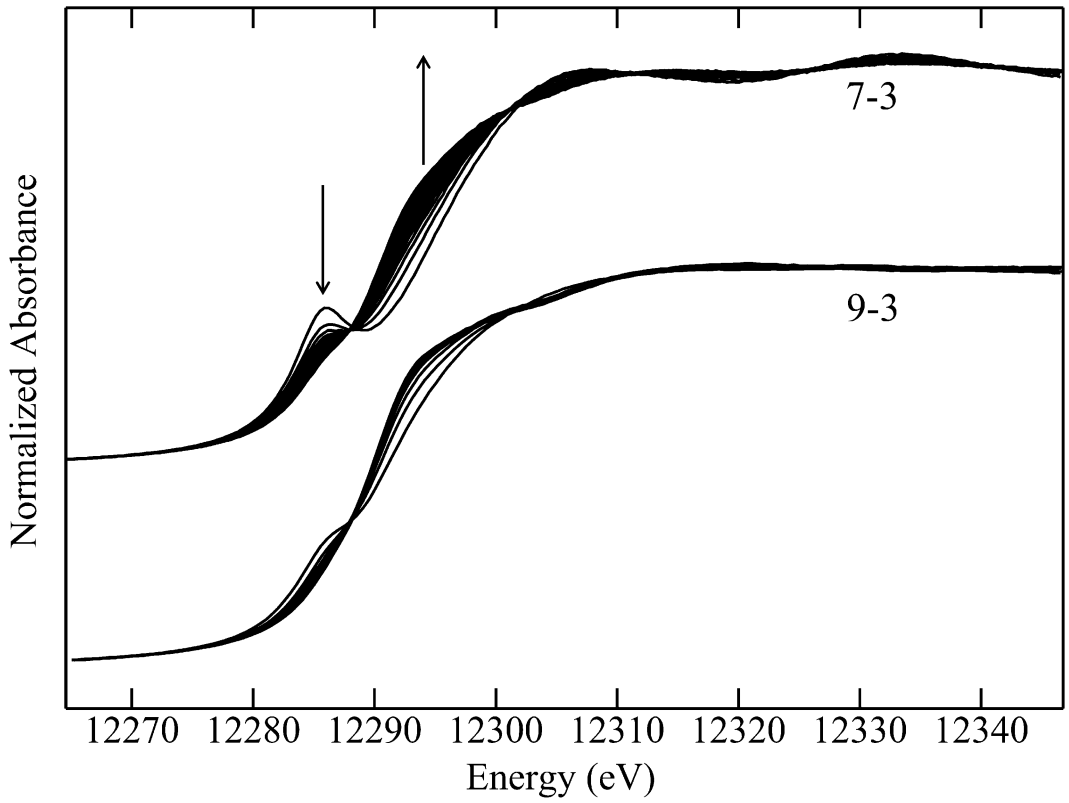

Figure 5.1 Changes with time in Hg L_{III} X-ray absorption near-edge spectra of a 1 mM aqueous solution of mercuric acetate in the presence of 25% v/v glycerol recorded on beamlines with differing flux density, estimated to be 4.0×10^{11} photons/sec/mm^2 (7-3) and 3.0×10^{12} photons/sec/mm^2 (9-3). The arrows show the direction of the change with increasing exposure time. Time between successive sweeps is 1195 sec. 19 and 8 sweeps are shown for 7-3 and 9-3 data, respectively.

The photoreduced sample is remarkable in lacking almost all spectroscopic structure, with no obvious EXAFS oscillations above the absorption edge. Figure 5.3 compares the EXAFS and corresponding Fourier transforms of both samples, together with the results of EXAFS curve-fitting analysis. The curve-fitting shows that, as expected, the initial Hg(II) sample is dominated by relatively strong EXAFS from two Hg–O bonds at 2.10 Å, with some contributions from more distant O atoms, while the EXAFS of the photochemically modified sample shows no short Hg–O bonds, with its EXAFS best fit to a combination of long Hg···O interactions at 2.94, 3.28 and 3.61 Å (Table 5.1). For the starting material, predictions of the expected solution species prior to freezing using the program MINTEQ[27] suggests a predominance of $Hg(OH)_2$, with very little acetate remaining bound to Hg.

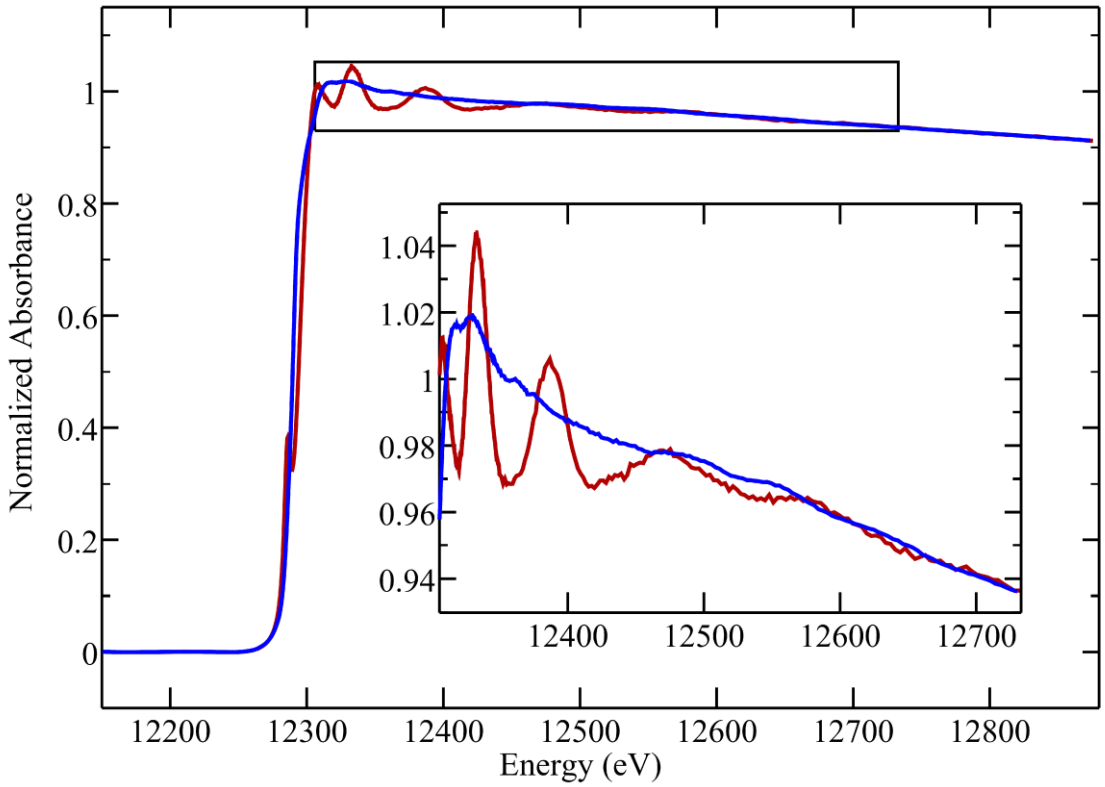

Figure 5.2 Normalized X-ray absorption spectra of Hg(II) reactant (—)photo-reduced product (—)showing the relative lack of spectral structure in the spectrum of the photo-reduced sample.

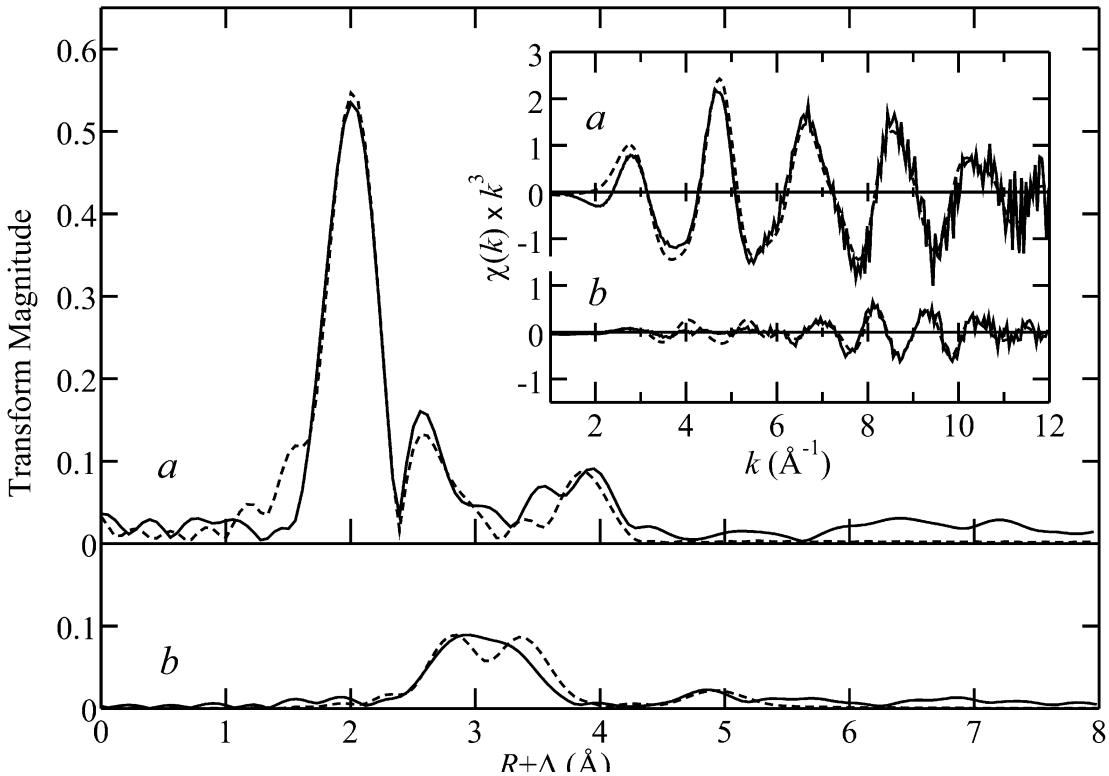

Figure 5.3 EXAFS Fourier transforms with Hg–O phase-correction of reactant (*a*) and product (*b*) (——)(solid lines) together with the results of EXAFS curve-fitting analyses (- - - -) (broken lines). The inset shows the corresponding EXAFS oscillations.

Table 5.1 Summary of EXAFS curve fitting results[a]

Reactant			Product [b]		
N	R	σ^2	N	R	σ^2
2	2.099(3)	0.0058(1)	0.6(1)	2.935(4)	0.0031(3)
1	2.784(9)	0.0069(11)	0.4(1)	3.281(9)	0.0031(3)
2	3.87(2)	0.0068(21)	1.0(1)	3.613(4)	0.0031(3)
2	4.03(10)	0.0031(12)	1	5.15(1)	0.0048(5)

a. All backscatterers reported in the table are oxygen atoms. Inclusion of other possible neighboring atoms, such as Hg, did not give reasonable fits. Coordination numbers *N*, interatomic distances *R* (Å), Debye-Waller factors σ^2 (Å^2). Because the data presented herein are of limited *k*-range and relatively poor signal to noise, the threshold energy shift ΔE_0 was fixed at a value of –11.0 eV, determined from curve-fitting analyses of a series of standard compounds. Values in parentheses are the estimated standard deviations in the last digit(s) obtained from the diagonal elements of the covariance matrix; these are precisions and are distinct from the accuracies which are expected to be larger (accuracies *ca* ±0.01-0.02 Å for *R*, and ±10-20% for both *N* and σ^2).

b. Non-integer values of *N* were floated but linked together to give a total coordination number for this distance range of 2, while common values of σ^2 were floated in the refinement as a single variable. This strategy was adopted since co-refinement of *N* and σ^2 is not considered good practice because of the high degree of mutual correlation of these two variables in the refinement, especially when the data are of limited *k*-range, as in the present case.

For the reaction product, the remarkably low EXAFS amplitude means that the data have inherently poor signal to noise, and the limited *k*-range, together with the distinct possibility of a mixture of species in the reaction product, gives rise to considerable analytical uncertainties compared with the initial species. For the photoreduction product three weak but discrete features in the Fourier transform are observed. A broad double-peak feature centered at about 3.2 Å, suggestive of more than one interaction, is weak but well above background. An additional weak feature at about 5 Å is close to the level of noise, which can be seen from the high-*R* part of the transform in Figure 5.3, and its inclusion in our fits is subject to some uncertainty. Moreover, for the remote weakly-detected ligands observed both coordination numbers and Debye-Waller factors are unknowns. In general, it is considered unwise to refine both the σ^2 value of the Debye-Waller factor and the coordination number because these variables tend to show a high degree of mutual correlation in refinements, and unreliable conclusions can result especially when the *k*-range is limited. For this reason the number of variables in the refinements was reduced by locking several Debye-Waller factors together, and floating the coordination number as a single linked variable of fixed sum, thereby reducing the number of variables to a total of 7 (Table 5.1). The broad ~3.2 Å peak is best fit with three different Hg⋯O that partly cancel, explaining the low EXAFS amplitude. If fewer interactions are included then the EXAFS shows more intensity between *k* of 2 and 6 $Å^{-1}$. Notwithstanding the problems we have discussed, the analysis clearly indicates that there are no atoms closer to Hg than 2.9 Å, and that the EXAFS is consistent with a combination of very long Hg⋯O interactions between 2.94 and 3.61 Å (Table 5.1).

Figure 5.4 compares the near-edge portion of the XAS spectra of Figure 5.2, together with the spectrum of liquid elemental mercury. The electronic configuration of Hg(0) is [Xe] $4f^{14}$ $5d^{10}$ $6s^2$ while Hg(II) is $6s^0$. The Hg L_{III} near-edge spectrum of Hg(II) is therefore expected to exhibit a distinct dipole-allowed $2p_{3/2} \rightarrow 6s$ transition, to which we attribute the pronounced peak at 12286.2 eV, with the main rise of the absorption edge centered at 12295.4 eV. The photoreduced spectrum is relatively unstructured with the main rise of the absorption edge shifted to lower energy by about 8.7 eV. The spectrum of frozen elemental liquid mercury has more structure than the spectrum of the photoreduced sample, with the main rise of the absorption edge shifted to still lower energy by an additional 1.4 eV. While the intermediate position of the photoreduced spectrum might be suggestive of photoreduction to Hg(I), that is

considered unlikely since the spectrum does not change upon further exposure, and the correspondingly relatively isolated Hg site would not be expected for a Hg(I) oxidation state. The Hg(I) oxidation state is mostly known from binuclear $[Hg_2]^{2+}$ complexes which exhibit a metal-metal bond of about 2.52 Å; mononuclear Hg(I) has not been observed in structurally characterized samples.[1] Moreover, the presence of hard ligands such as the oxygens in our samples, although bound through distant weak bonds, is expected to shift the spectrum to higher energies relative to the frozen liquid metal spectrum which will be influenced by electron-rich metal neighbors.

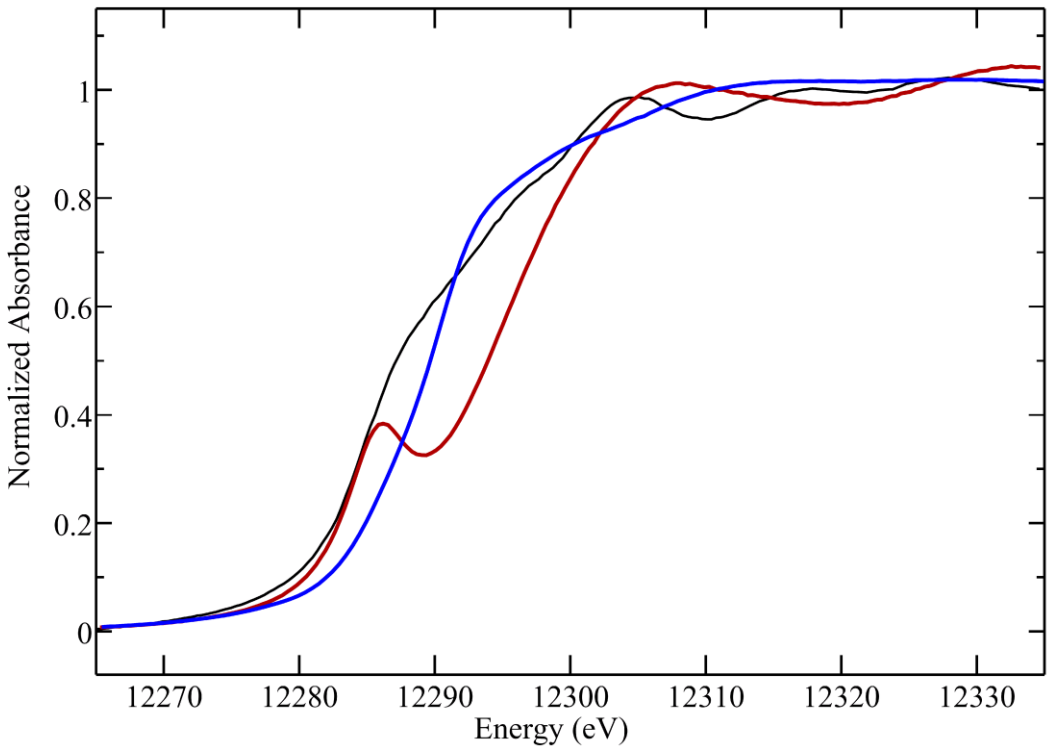

Figure 5.4 Detail of the X-ray absorption near-edge spectra of the reactant (—) and photoreduction product (—) compared with that of elemental liquid mercury (—).

5.7.2 DFT Calculations

Energy minimized geometry optimized structures were computed for Hg(II), Hg(I) and Hg(0). In initial calculations we compared calculations of mercury atoms with different oxidation states in the presence of two adjacent waters (H_2O) or hydroxyls (HO^-), with a COSMO field to approximate more remote solvent. The results of 18 different calculations for $Hg(OH)_{2-n}(OH_2)_{m+n}$ (m=0,4; n=0,1,2) with mercury in three different oxidation states are summarized in Table 5.2. Examination of the computed total energies (enthalpies) for the two-coordinate species (m=0) in the three different oxidation states, and using the computed enthalpies of isolated H_3O^+, H_2O and HO^- to balance the calculations indicated that, as expected, the most stable forms for Hg(II), Hg(I) and Hg(0) are predicted to be the neutral species $Hg(II)(OH)_2$, $Hg(I)(OH)OH_2$ and $Hg(0)(OH_2)_2$, respectively. Further calculations in the presence of six adjacent water molecules or hydroxyls (m=4) are also summarized in Table 5.2 with Figure 5.5 showing the results of these calculations. The computed Hg(II) structure contains two nearly equivalent Hg–OH bonds at 1.98 Å, with four adjacent more distant waters at 2.86 to 3.07 Å. The Hg(I) structure has a single Hg–OH bond at 2.10 Å and five $Hg\cdots OH_2$ at 2.90 to 3.54 Å, with the longest $Hg\cdots OH_2$ positioned approximately *trans* to the Hg–OH (Figure 5.5). The Hg(0) structure has six long $Hg\cdots OH_2$ at ranging from 3.32 to 3.72 Å. The calculations with six oxygens took substantially longer to converge than the simple two-oxygen computations, mainly due to the displacement convergence criteria as the more remote waters caused very small energy changes with substantial displacement. Thus, and as expected given this observation, subtly varying the starting coordinates or slightly altering the conditions of the calculation gave converged energetic endpoints that were subtly different, with altered $Hg\cdots O$ distances, for example the $Hg(0)(H_2O)_6$ converged to longer bond-lengths ranging from 3.19 to 3.77 Å when using the dielectric constant for water with the COSMO field (ε=78.54).

Moreover, preliminary calculations on the Hg(0) oxidation state using QMERA, combining a 10 Å spherical cluster of 74 water molecules treated with molecular mechanics (GULP with Drieding Forefield,[28,29] including solvent with 1.0 Å radius, and ε=69.53) with DFT for the innermost waters and the mercury, gave very similar results to our $Hg(0)(OH_2)_6$ calculations. Overall, our calculations show that the types of distances that we have observed in our EXAFS experiments are consistent with Hg(0) in an aqueous environment, and support previous suggestions of an essentially monatomic Hg(0) solvation model.

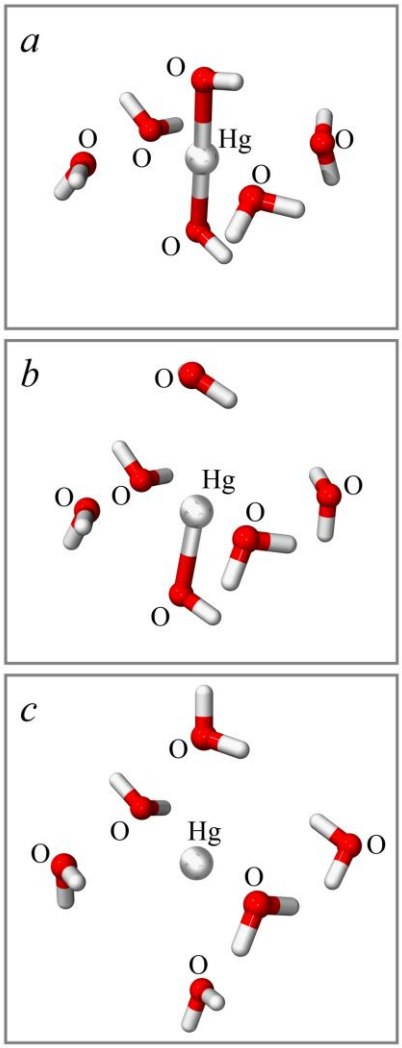

Figure 5.5 Results of density functional theory energy minimized geometry optimization calculations of mercury H_2O/HO^- complexes showing (*a*) Hg(II), (*b*) Hg(I) and (*c*) Hg(0). In each case the formal mercury oxidation state was varied by using a charge neutral calculation and by varying the number of protons bound to water.

Table 5.2 Selected Density Functional Theory Interatomic Distances[a]

	Hg(II)		Hg(I)		Hg(0)	
stoichiometry	Hg–O	Hg···O	Hg–O	Hg···O	Hg–O	Hg···O
$Hg(OH)_2$	2×1.95		2×2.17		2×2.49	
$Hg(OH)(OH_2)$	1.93,2.04		2.10	2.65	2.36	4.02
$Hg(OH_2)_2$	2×2.03		2×2.39			3.20,3.80
$Hg(OH)_2(OH_2)_4$	2×1.98	2.86–3.07	2.13,2.21	3.53–3.65	2.30	3.44–3.77
$Hg(OH)(OH_2)_5$	2.02,2.19	2.50–2.65	2.10	2.90–3.54	2.28	3.60–3.74
$Hg(OH_2)_6$	2.26,2.29	2.32–2.37	2.37	2.55–2.84		3.32–3.72

[a] Interatomic distances are given in Å.

5.8 Discussion

Our results strongly suggest that we have observed the photochemical reduction of Hg(II) in frozen solution and that the resulting product is a nearly isolated Hg(0) site with only distant neighbors. As previously discussed the maximum solubility of Hg(0) in water is close to 0.7 μM,[8] and while this solubility is high for a metal such concentrations are problematically low for many analytical methods; indeed, most studies of Hg(0) in aqueous solution use concentrations of 0.15-0.2 μM. A commonly used method of preparation of such aqueous Hg(0) solutions is to use liquid elemental mercury enclosed in silicone tubing closed with polytetrafluoroethylene (Teflon^{TM}) plugs, relying on the diffusion of Hg(0) through the silicone over a few days to produce solutions.[30] At such low concentrations, the purity of solutions and the degree of anaerobicity (if anaerobic) become major issues.[31] Plasticizers such as phthalate esters, used in commercial silicone and other polymers,[32] can leach out of the polymer into aqueous media at concentrations that are close to or exceeding those of any dissolved Hg(0). Because of these issues, experiments on aqueous Hg(0) are especially challenging, and some previously reported and chemically unexpected results may in fact be due to these complications. For example, it has been reported that organic thiol compounds can oxidize Hg(0) to Hg(II) in aqueous solutions through unknown mechanisms.[30] Thiols (RSH) are well established as reducing agents via the familiar reaction $2RSH \rightarrow RSSR + 2H^+ + 2e^-$ with neutral-pH midpoint potentials in the range –226 to –330 mV.[33] They are not known as oxidizing agents, being stable even at very low redox potentials, and the observed oxidation of Hg(0) to Hg(II) may in fact be due to difficulties related to working with such dilute solutions, despite quite stringent efforts to control the conditions.[30]

We briefly investigated possible photoreduction of frozen solutions of other Hg(II) species. We find that compounds of methylmercury (CH_3Hg–) and compounds with thiolate or halide ligands to the metal were in general less susceptible to photoreduction, whereas compounds with hard ligands, such as Hg(II) in solution with excess 1-methyl-imidazole, showed clear changes in the Hg L_{III} near-edge spectrum indicative of photoreduction. Thus, methylmercury-L-cysteineate was stable in the beam for extended periods, while methylmercury hydroxide showed some photoreduction, but much less so than did the

solutions of mercuric acetate reported here. The possibility of using X-ray induced photoreduction with other metals that like mercury only rarely show zero-valent monatomic solvated species, such as Pt(II) and Au(I), will be investigated in future work.

The work reported herein can also be criticized as being distinct from Hg(0) in a true aqueous solution. Firstly, our Hg(0) samples are produced photochemically in a glassy glycerol-water solution, and are many times more concentrated than actual solutions of Hg(0) in liquid water. Moreover, molecular motion must at some level be restricted by the use of a glassy matrix at 10 K, which may structurally affect our results because the starting material possesses two Hg–O bonds at 2.099 Å. Because of these considerations, our system cannot be considered an absolutely faithful model of Hg(0) in aqueous solution. Notwithstanding these criticisms, our results do come close to representing the conditions of aqueous solution, and we provide the only direct structural information to date on Hg(0) in an aqueous environments.

5.9 Conclusions

The work that we have presented here provides the first experimental evidence relevant to the chemical nature of Hg(0) in aqueous solutions. We find that the presumed monatomic nature of the metal is close to an accurate picture, with the metal being only weakly coordinated by long bonds to oxygen.

REFERENCES

1) Groom, C. R.; Bruno I. J.; Lightfoot, M. P.; Ward, S. C. The Cambridge Structural Database. *Acta Cryst*. **2016**, *B72*, 171–179.

2) Sokolov, M. N.; Virovets, A. V.; Dybtsev, D. N.; Gerasko, O. A.; Fedin, V. P.; Hernandez-Molina, R.; Clegg, W.; A. G. Sykes. Metal incorporation into and dimerization of M_3E_4 clusters (M = Mo, W; E = S, Se) in supramolecular assemblies with cucurbituril: A molecular model of intercalation. *Angew. Chem. Int. Ed*. **2000**, *39*, 1659–1661.

3) Fedin, V. P.; Sokolov, M.; Lamprecht, G. J.; Hernandez-Molina, R.; Seo, M-S.; Virovets, A. V.; Clegg, W.; Sykes, A. G. Preparation, structure, and properties of the corner-shared double cubes $[Mo_6HgQ_8(H_2O)_{18}]^{8+}$ (Q = S, Se) and tungsten analogues. *Inorg. Chem*. **2001**, *40*, 6598–6603.

4) Tanase, T.; Goto, E.; Takenaka, E.; Horiuchi, T.; Yamamoto, Y.; Kuwabara, J.; Osakada, K. Cage-Type Hexanuclear platinum(0) clusters with diphosphine and isocyanide ligands encapsulating two mercury(0) atoms. *Organometallics*, **2005**, *24*, 234–244.

5) Mickiewicz, M. M.; Raston, C. L.; White A. H.; Wild, S. B. Crystal structures of bis[tricarbonyl(η-cyclopentadienyl)molybdato(0)]mercury(II) and trans-dicarbonyl(dimethylphenylarsine)[iodomercurio(0)](η-methylcylopentadienyl) molybdenum(II). *Austr. J. Chem*. **1977**, *30*, 1685–1691.

6) Catalano, V. J.; Malwitza, M. A.; Noll, B. C. A linearly coordinated Hg(0) trapped in a gold(I) metallocryptand cage. *Chem. Commun*. **2001**, 581–582.

7) Soerensen, A. L.; Mason, R. P.; Balcom, P. H.; Jacob, D. J.; Zhang, Y.; Kuss, J.; Sunderland, E. M. Elemental mercury concentrations and fluxes in the tropical atmosphere and ocean. *Environ. Sci. Technol*. **2014**, *48*, 11312–11319.

8) Sanemasa, I.; Haraguchi, K.; Nagai, H. Effects of salts on the solubility of elemental mercury in water. *Bull. Chem. Soc. Jpn.* **1981**, *54*, 1040–1043.

9) Greenwood, N. N. and Earnshaw, A., Chemistry of the Elements, Second Edition. Butterworth-Heinemann, Oxford, **1984**.

10) Sandborgh-Englund, G.; Elinder C.-G.; Johanson, G; Lind, B.; Skare, I.; Ekstrand, J. The absorption, blood levels, and excretion of mercury after a single dose of mercury vapor in humans. *Toxicol. Appl. Pharmacol*. **1998**, *150*, 146–153.
11) Wilhelm, S. M.; Liang, L.; Cussen, D.; Kirchgessner, D. A. Mercury in crude oil processed in the United States. *Environ. Sci. Technol.* **2007**, *41*, 4509–4514.
12) George, G. N.; Pickering, I. J.; Pushie, M. J.; Nienaber, K.; Hackett, M. J.; Ascone, I.; Hedman, B.; Hodgson, K. O.; Aitken, J. B.; Levina, A.; Glover, C.; Lay, P. A. X-ray induced photo-chemistry and X-ray absorption spectroscopy of biological samples. *J. Synchrotron Radiat*. **2012**, *19*, 875–886.
13) Sneeden, E. Y.; Hackett, M. J.; Cotelesage, J. J. H.; Prince, R. C.; Barney, M.; Goto, K.; Block, E.; Pickering, I. J.; George, G. N. Photochemically-generated thiyl free radicals observed by X-ray absorption spectroscopy. *J. Am. Chem. Soc*. **2017**, *139*, 11519–11526.
14) Nienaber, K. H.; Pushie, M. J.; Cotelesage, J. J. H.; Pickering, I. J.; George, G. N. Cryoprotectants remarkably exacerbate X-ray induced photoreduction. *J. Phys. Chem. Lett.* **2018**, *9*, 540-544.
15) Cramer, S. P.; Tench, O.; Yocum, M.; George, G. N. A 13-element Ge detector for fluorescence EXAFS. *Nucl. Instr. Meth. A*. **1988**, *266*, 586–591.
16) George, M. J. XAS-Collect: A computer program for X-ray absorption spectroscopic data acquisition *J. Synchrotron Radiat*. **2000**, *7*, 283–286.
17) George, G. N.; Garrett, R. M.; Prince, R. C.; Rajagopalan, K. V. The molybdenum site of sulfite oxidase: A comparison of wild-type and the cysteine 207 to serine mutant using X-ray absorption spectroscopy. *J. Am. Chem. Soc*. **1996**, *118*, 8588–8592.
18) George, G. N. **2000**, http://www-ssrl.slac.stanford.edu/exafspak.html
19) Rehr, J. J.; Mustre de Leon, J.; Zabinsky, S. I.; Albers, R. C. Theoretical X-ray absorption fine structure standards. *J. Am. Chem. Soc.* **1991**, *113*, 5135–5140.
20) Mustre de Leon, J.; Rehr, J. J.; Zabinsky, S. I.; Albers, R. C. *Ab initio* curved-wave X-ray-absorption fine structure. *Phys. Rev. B.* **1991**, *44*, 4146–4156.
21) Delley, B. An all-electron numerical method for solving the local density functional for polyatomic molecules. *J. Chem. Phys*. **1990**, *92*, 508–517.

22) Delley, B. From molecules to solids with the DMol^3 approach. *J. Chem. Phys*. **2000**, *113*, 7756–7764.
23) Peverati, R.; Truhlar, D. G. M11-L: A local density functional that provides improved accuracy for electronic structure calculations in chemistry and physics. *J. Phys. Chem. Lett*. **2012**, *3*, 117–124.
24) Klamt, A.; Schüürmann, G. COSMO: a new approach to dielectric screening in solvents with explicit expressions for the screening energy and its gradient. *J. Chem. Soc., Perkin Trans.* **1993**, *2*, 799–805.
25) Malinowski, E. R. Determination of the number of factors and the experimental error in a data matrix, *Anal. Chem*. **1977**, *49*, 612–617.
26) Isoya, J.-I.; Fujiwara, S. EPR study of Cd(I) and Hg(I) Hot Ions: Effect of Surrounding Lattice, *J. Magn. Reson.* **1979**, *34*, 377–392.
27) https://vminteq.lwr.kth.se/
28) Gale, J. D.; Rohl, A. L. The General Utility Lattice Program (GULP). *Mol. Simul*. **2003**, *29*, 291–341.
29) Mayo, S. L.; Olafson, B. D.; Goddard, W. A. DREIDING: A Generic Force Field for Molecular Simulations, *J. Phys. Chem.* **1990**, *94*, 8897–8909.
30) Zheng, W.; Lin, H.; Mann, B. F.; Liang, L.; Gu, G. Oxidation of dissolved elemental mercury by thiol compounds under anoxic conditions. *Environ. Sci. Technol.* **2013**, *47*, 12827–12834.
31) Whalin, L. M.; Mason, R. P. A new method for the investigation of mercury redox chemistry in natural waters utilizing deflatable Teflon® bags and additions of isotopically labeled mercury. *Analytica Chim. Acta*, **2006**, *558*, 211–221.
32) Eckert, E.; Frank, M.; Goeen, T.; Purbojo, A.; Mueller, J.; Cesnjevar, R. Comparative study on the migration of di-2-ethylhexyl phthalate (DEHP) and tri-2-ethylhexyl trimellitate (TOTM) into blood from PVC tubing material of a heart-lung machine. *Chemosphere*, **2016**, *145*, 10–16.

33) Kemp, M.; Go, Y-M.; Jones, D. P. Nonequilibrium thermodynamics of thiol/disulfide redox systems: A perspective on redox systems biology. *Free Radic. Biol. Med*. **2008**, *44*, 921–937.

6. Mechanisms of Photoexcitation and Cryoprotectant Hydroxyl Radical Scavenging

6.1 Preface

Results from Chapter 4 demonstrated that cryoprotectants exacerbate photoreduction in samples containing metals. Having then exploited that fact to produce and study the chemically interesting Hg(0) species as described in Chapter 5, an effort was made to model the mechanisms of photoexcitation observed in these samples. Utilizing density function theory calculations (DFT), models were constructed to examine transition state energies of the radical intermediates, and specifically the photoexcitation products of water.

6.2 Manuscript Author Contributions

Kurt H. Nienaber, Ingrid J. Pickering, and Graham N. George. Mechanisms of Photoexcitation and Cryoprotectant Hydroxyl Radical Scavenging.

Kurt Nienaber took primary responsibility for experimental design, data analysis, and manuscript drafting. Ingrid Pickering took responsibility for assisting in manuscript editing and experimental consultation. Graham George took responsibility for assisting in experimental design, data analysis, manuscript drafting.

6.3 Acknowledgements

Research at the University of Saskatchewan is supported by a grant from the Chevron Energy Technology Company, the Natural Sciences and Engineering Research Council (GNG, IJP), the University of Saskatchewan and by Canada Research Chairs (GNG, IJP). Use of the Stanford Synchrotron Radiation Lightsource, SLAC National Accelerator Laboratory, is supported by the U.S. Department of Energy, Office of Science, Office of Basic Energy Sciences under Contract No. DE-AC02-76SF00515. The SSRL Structural Molecular Biology Program is supported by the DOE Office of Biological and Environmental Research, and by the National Institutes of Health, National Institute of General Medical Sciences (including

P41GM103393). The contents of this publication are solely the responsibility of the authors and do not necessarily represent the official views of NIGMS or NIH.

6.4 Abstract

Here we examine the radiation chemistry of water, and specifically the photochemical products of water interacting with cryoprotectants, using computational chemistry. An analysis of numerous computational methods, using methanol as a representative alcohol-containing cryoprotectant, revealed the carbon-centered radical to be energetically favourable. Calculations were carried out on the photochemical products of water, their interactions with cryoprotectants, direct photoexcitation of model cryoprotectants, and direct excitation of model peptides and peptide backbones. Final consideration was given to the mobility of solvated electrons and hydroxyl radicals in terms of propagating photodamage in cryogenically frozen samples.

6.5 Introduction

The field of radiation chemistry is very well established, having its origins in the pioneering works of Becquerel[1] and Curie.[2] It is a branch of physical chemistry which studies the chemical transformations of materials upon exposure to high-energy radiation of one type or another.[3] While the broader field of radiation chemistry concerns chemical manifestations of exposure to energetic photons, energetic charged particles such as electrons, positrons, protons, or heavy ions, as well as neutral particles such as neutrons, we are concerned here only with photons, and in particular with X-rays.

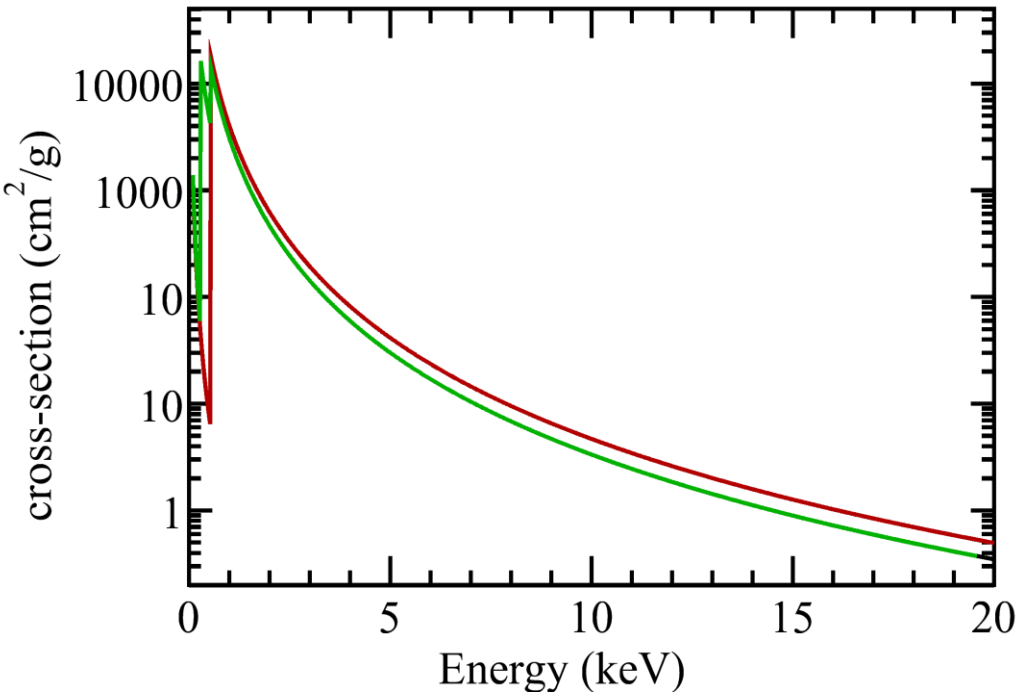

Figure 6.1: Calculated X-ray cross-section verses X-ray energy for water (red curve) and methanol (green curve). The K-absorption edges of carbon (*ca*. 277 eV) and oxygen (*ca*. 525 eV) can be seen in the far left of the plot. The cross-section can be seen to vary by more than five orders of magnitude over the energy range of the plot.

Central to quantitative radiation chemistry is the *G*-value, which is defined as the number of molecules of reactant consumed or product formed per 100 eV of radiation energy absorbed. *G*-values depend strongly upon a number of factors such as composition and temperature. The absorption can be simply calculated from the photo-absorption cross section. This is directly related to the energy of X-rays, which is why sample photodamage is often much less pronounced when using higher energy X-rays. Figure 6.1 compares the calculated X-ray cross section for water (red) and methanol (green), given in the conventional units of $cm^2 \cdot g^{-1}$. The cross-section can be seen to be very substantially higher at lower energies.

X-ray based methods, predominantly macromolecular crystallography (MX) but also, and to a lesser extent, X-ray absorption spectroscopy (XAS), have revolutionized the process of structural determination. However, these tools depend critically upon the use of ionizing radiation and the radiation chemistry arising from X-ray irradiation can induce chemical changes in samples, affecting both oxidation state and structure. These X-ray induced chemical changes give rise to potential problems in structure determination.[4] The remarkable increase in the brightness of synchrotron radiation X-ray sources has meant that X-ray-induced photochemical changes in samples are of growing concern.[5] In previous work we have shown that cryoprotectants such as polyethyleneglycol (PEG) or glycerol, that are routinely added to MX or XAS samples to maintain sample crystallinity at cryogenic temperatures or to improve data quality, respectively, can affect photoreduction.[6] We demonstrated a remarkable 10-fold exacerbation in rate of photoreduction of Cu(II) to Cu(I) when either alcohol or ether-based cryoprotectants were present,[6] and postulated that the mechanism was due to the well-known hydroxyl radical scavenging capabilities of cryoprotectants.[6]

In the present paper we use computational chemistry to explore the radiation chemistry of water and interaction of cryoprotectants with some of the photochemical products of water.[7] Using the same methods we also explore the nature of some potential photochemical products of cryoprotectants themselves, and of protein polymers.

6.6 Semi-Empirical Quantum Chemistry Calculations

These used the VAMP code, version 10.0 as implemented in BIOVIA Materials Studio Version 2018 R1. Calculations employed the neglect of diatomic differential overlap (NDDO) approximation with the PM6 Hamiltonian and Restricted Hartree-Fock (RHF) calculation of spin-state.

6.7 Density Functional Theory (DFT) Calculations

DFT geometry optimizations were carried out using DMol^3 and BIOVIA Materials Studio Version 2018 R1.[8] Apart from those discussed in section 6.8.1, most calculations used the generalized gradient approximation (GGA) and employed the Perdew-Burke-Ernzerhof (PBE) functional both for the potential during the self-consistent field procedure, and for the energy. Dmol^3 double numerical basis sets included polarization functions for all atoms with all-electron core treatments. Solvation effects, when used, were modeled using the Conductor-like Screening Model (COSMO)[9] in Dmol^3. Transition state search and optimization used the GGA/PBE functional with the linear synchronous transit/quadratic synchronous transit/conjugate gradient (LST/QST/CG) method implemented within DMol^3.

6.8 Results and Discussion

6.8.1 Comparison of Density Functional Theory Methods

As a precursor to the calculations contained in this paper, we first compared the relative performance of different computational theory alternatives for two of the radicals considered below. Table 6.1 shows a comparison of methods calculating the energy differences between two free radical entities relevant to this work; the carbon-centered methylene hydroxide radical •CH_2OH and the methoxy radical CH_3O•. The differences between energies computed using a range of different DFT and related methods are compared in Table 6.1.

Table 6.1. Comparison of Computational Methods

	Energies (Hartrees) [a]		
Method	**$CH_3O•$**	**$•CH_2OH$**	**ΔE (kJ·mol^{-1})**
NDDO/PM6	0.011525	–0.03722	–127.98
HF	–116.90575	–117.02248	–306.46
B3LYP	–121.51062	–121.53835	–72.80
LDA/VWN	–114.15987	–114.17205	–31.97
LDA/PWC	–114.15536	–114.16743	–31.70
GGA/BPE	–114.94715	–114.95831	–29.30
GGA/BLYP	–115.05389	–115.06342	–25.04
GGA/VWN-BP	–115.07748	–115.08902	–30.29
mGGA/M11-L	–115.02374	–115.02563	–4.96

All calculations were done on isolated free radical entities in a vacuum. Energies are computed as heat of formation with the semi-empirical calculations NDDO/PM6, while for Hartree-Fock (HF), DFT (LDA, GGA) and hybrid (mGGA) methods, energies are expressed as *total energy*, which is computed as the energy change upon separation of all nuclei and electrons to infinity.

All the computational methods tested gave lower energies for the carbon-centered methylene hydroxide radical (•CH_2OH) than the methoxy radical (CH_3O•). The pure DFT methods show remarkable consistency in the estimated energy difference of 25–32 kJ·mol^{-1} with the exception of B3LYP,[10] which estimated a somewhat larger energy difference. The DFT methods in general show excellent agreement with literature values for the relative stability of these species of approximately 39 kJ kJ·mol^{-1}.[11] Perhaps not surprisingly, the semi-empirical, Hartree-Fock and hybrid methods show no quantitative agreement, either with each other or with the pure DFT methods. For the remainder of the calculations presented in this paper the Generalized Gradient Approximation (GGA) and the Perdew-Burke-Ernzerhof (PBE) functional was employed, it provides a combination of reasonably fast execution speeds with lower demands on computer memory resources and reasonably accurate results.

6.8.2 Photochemistry of Water

In general, the complex chain of reactions discussed by others[12,13] are initiated by absorption of a photon by an electron, to give a photoexcited state (eq. 6.1).

$$H_2O + h\nu \rightarrow H_2O^+ + e^-_{aq} \qquad (6.1)$$

Where in eq. 6.1 the H_2O^+ is photoexcited water and e^-_{aq} signifies the hydrated or solvated electron. The electronic structure of water is $(1a_1)^2(2a_1)^2(1b_2)^2(3a_1)^2(1b_1)^2(4a_1)^0(2b_2)^0(3b_2)^0$ and the photo excited electron can, in principle, originate from any of the five occupied molecular orbitals, creating a family of different H_2O^+ photoexcited states. For example, ejection of an oxygen 1s electron $(1a_1)^2$ will create H_2O^+ photoexcited state with a 1s core-hole. This would decay either by emission of a fluorescent photon predominantly through dipole-allowed (Δl=±1) transitions to yield a less-excited radical cation, still formally H_2O^+, or by Auger electron emission to yield a further less energetic e^-_{aq} solvated electron, and the di-cationic species H_2O^{2+}, which will in turn quickly acquire a lower energy electron from the system. The energetic electrons themselves will also interact with water, losing energy and creating a cascade of radical anions and cations. For the X-ray spectroscopist it is commonplace to observe so-called beam-marks on samples, arising from color centers caused by e^-_{aq} trapped in the ice matrix plus other highly colored free radical entities; for example

HO• appears vivid blue, following X-ray irradiation in an XAS experiment at liquid helium temperatures (*ca*. 10 K). A typical sample showing a band of color corresponding to the X-ray irradiated portion is shown in Figure 6.2. Such beam marks decay upon (relatively high temperature) annealing in liquid nitrogen (77 K) which is presumed due to the radicals and solvated electrons reacting to form less energetic and less colored species. When protein solutions are taken from the low temperature (10 K) cryogenic irradiation and thawed directly, the solution will frequently foam, protein will precipitate, and an unpleasant smell resembling that of burning hair can often be detected.[14] However if the frozen solutions are first annealed at 77 K for 1-2 hours then clear protein solutions typically result upon thawing,[14] suggesting that more substantial damage occurs from the radicals and solvated electrons that are accumulated at 10 K. By the same token, X-ray crystallographers frequently observe that crystals turn very dark upon irradiation, appearing black or dark brown in color, although in this case sample temperatures are usually relatively high (*ca*. 80 K) and X-ray beams of much greater flux density, so that different species may be involved.

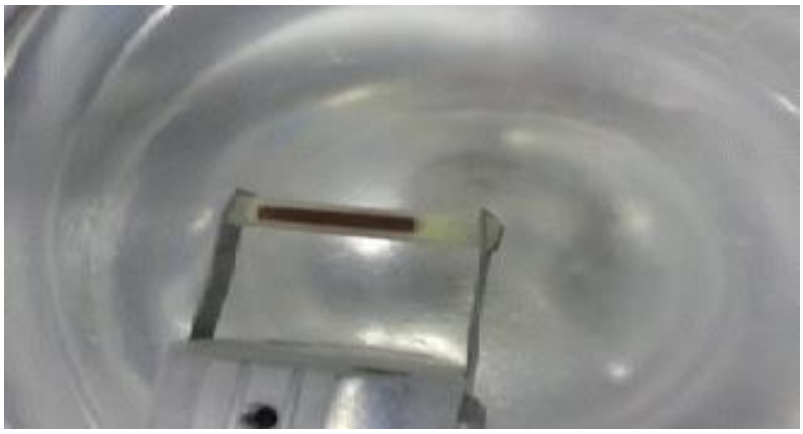

Figure 6.2: Metalloprotein sample following X-ray absorption spectroscopic measurements showing a beam mark.

A similar initial process operates for direct photoabsorption by cryoprotectants (considered below 3.4) and proteins (section 3.5). The structure of the hydrated electron has been the focus of much previous computational work, [15]–[20] with most models describing a cluster of water molecules $[(H_2O)_n]^-$ where *n* usually ranges from 4 to 6, with one or more O–H bonds in the cluster elongated to a greater or lesser degree.[15–20] Irrespective of the structure, there is widespread agreement that e^-_{aq} is an incredibly potent reductant that has the potential to affect almost any redox active species that may be present in solution. Thus, two hydrated electrons can combine with water to yield molecular hydrogen:

$$e^-_{aq} + e^-_{aq} + H_2O \rightarrow H_2 + 2OH^- \quad (6.2)$$

All of these species can proceed to interact with solvent and other components of solution. Firstly, the mono-cationic species $[H_2O]^+$ can react with hydrated electrons to regenerate water and heat (eq. 6.3),[12] with no net change in the redox capabilities of the system.

$$H_2O^+ + e^-_{aq} \rightarrow H_2O + \Delta \quad (6.3)$$

Up until this point no calculations have been possible without an accurate computation model of e^-_{aq} and related species, which is acknowledged as a complex issue that is outside the scope of this paper. From here on in, however, we will consider computationally more tractable reactions. We approximate the 9-electron radical cation H_2O^+ as the energetically lowest lying of these species, which has the free radical spin density almost entirely localized in an oxygen 3p orbital (not illustrated). This species can react with H_2O to form hydronium ions and hydroxyl radicals (eq. 6.4):

$$H_2O^+ + H_2O \rightarrow H_3O^+ + HO\bullet \quad (6.4)$$

The product, HO•, is a highly oxidizing entity, which can react through dimerization to make hydrogen peroxide:

$$HO\bullet + HO\bullet \rightarrow H_2O_2 \qquad (6.5)$$

This is a highly exothermic reaction, with an enthalpy change of more than 300 kJ·mol–1 (Table 6.2), which demonstrates how highly chemically reactive HO• radicals are.

6.8.3 Interactions of water photochemical products with cryoprotectants and glassing agents.

Of central relevance to this paper is the reaction of HO• with cryoprotectants, which, for the sake of computational simplicity, we model using simple alcohols such as methanol CH_3OH, and simple ethers such as dimethylether $(CH_3)_2O$. Hydroxyl radicals can react with alcohols such as methanol through abstraction of either carbon or oxygen-bound protons, forming methylenehydroxy radicals and methoxy radicals plus water (eq. 6.6, 6.7):

$$HO\bullet + CH_3OH \rightarrow \bullet CH_2OH + H_2O \qquad (6.6)$$

$$HO\bullet + CH_3OH \rightarrow CH_3O\bullet + H_2O \qquad (6.7)$$

As expected, the reaction forming the more stable carbon-based radical (eq. 6.6) is calculated to have the greatest reaction enthalpy (Table 6.2). The greater stability of the methylenehydroxy radical can be understood by examination of the ground state structure, which shows spin density on both carbon and oxygen, with a nearly planar sp^2–type carbon, and the presence of π bonding between oxygen and carbon indicative of a partial double bond.

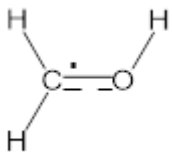

Transition state searches indicate that both reactions 6.6 and 6.7 are effectively barrierless, although introduction of intervening waters between the HO• and the proton being abstracted to form the product water, in an attempt to be more realistic, can be used to give reaction barriers of various but still small heights; we can anticipate that these reactions will proceed very quickly indeed.

As we have discussed above, •CH_2OH is more stable than CH_3O• by some 30 kJ·mol^{-1}, and it is of interest to investigate whether these species, once formed, might be able to interconvert. The results of the transition state search calculation are shown in Figure 6.3. The activation barrier $\Delta E^{\ddagger}$ is found to be substantial at 171.08 kJ·mol^{-1}, so that, once formed, the tautomers •CH_2OH and CH_3O• would not be expected to interconvert. Much of the relative stability of •CH_2OH is derived from the partial double bond character of the C–O bond, which in turn would restrict the rotational ability of the C–O bond. Enforcing C_s point group symmetry on •CH_2OH so as to restrict the orientation of the O–H to be on the mirror plane gives a decrease in the stabilization so that •CH_2OH lies only 8.98 kJ·mol^{-1} below CH_3O•, although a transition state search indicates a still substantial barrier with $\Delta E^{\ddagger}$ = 142.68 kJ·mol^{-1}. Thus, neglecting other factors, these free radicals are likely to be stable entities and once formed should be observed. Our computational results have relevance to electron paramagnetic resonance experiments on ^{60}Co irradiated frozen solutions. Extensive experiments on frozen methanol observed predominantly •CH_2OH with little CH_3O• formed.[21,22] While for methanol the C–H protons outnumber the O–H three to one, the lack of any predicted kinetic predilection for •CH_2OH over CH_3O• would argue for both being formed radiochemically, and once formed they ought to show similar stabilities. The answer may be that our calculations thus far totally neglect quantum mechanical tunneling.

Tunneling in a chemical reaction becomes important when the thermal de Broglie wavelength of a particle is of the same order of the width of an activation barrier. The thermal de Broglie wavelength λ_{th} of a non-relativistic particle of mass m is related to temperature T by eq. 7.8:

$$\lambda_{th} = \sqrt{\frac{2\pi\hbar^2}{mk_BT}} \tag{6.8}$$

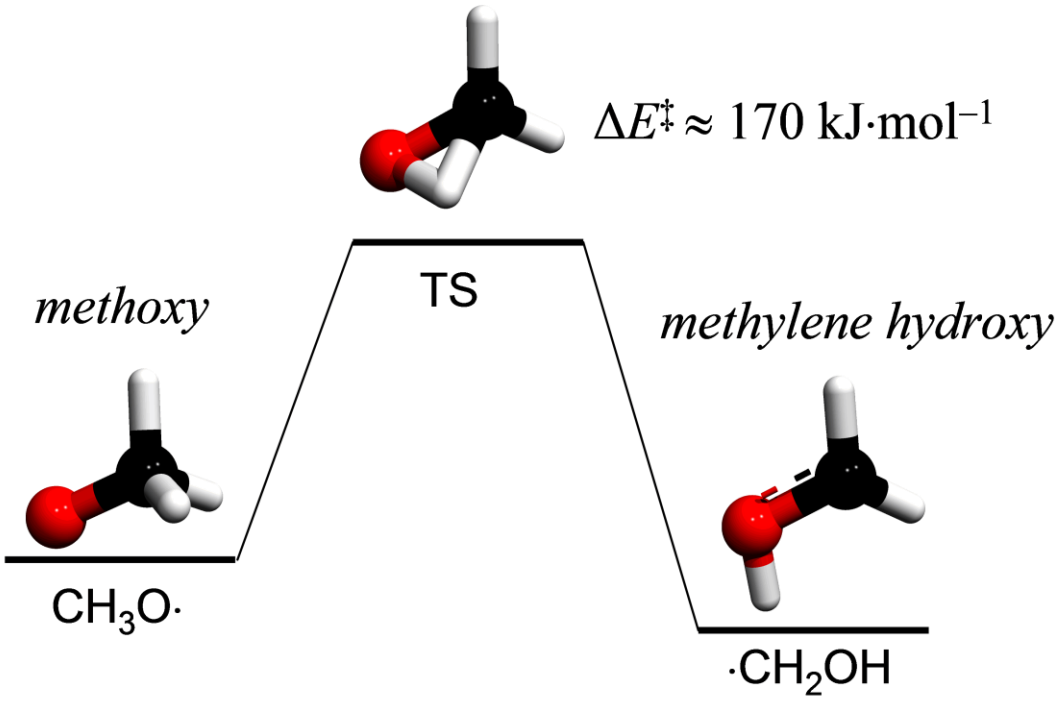

Figure 6.3: Transition state search results for interconversion of methoxy ($CH_3O\bullet$) and methylene hydroxyl ($\bullet CH_2OH$) tautomeric radical species.

In which k_B and $\hbar$ are Boltzmann's constant and the reduced Plank's constant, respectively. For a proton at 10 K and at 77 K we can compute λ_{th} values of 5.8 Å and 2.1 Å, respectively, which compares with a barrier width of ~ 1–2 Å. From elementary quantum mechanics we know that to a first approximation the probability P of a particle of mass m and energy E tunneling through a square potential energy barrier of height V and thickness δ is given by eq. 7.9:

$$P = \exp\left[-\left(\frac{2\delta}{\hbar}\right)\sqrt{2m(V-E)}\right] \tag{6.9}$$

This relationship shows that P falls dramatically with increasing m which affords rate enhancements for ^{1}H over ^{2}H and is responsible for otherwise surprisingly large kinetic isotope effects that can be observed.[23] Thus, while the >140 kJ·mol^{-1} barrier is more than adequate to prevent reaction under other circumstances, the fact that the transition state involves a translocation of a proton means that tunneling should facilitate the conversion to the more stable tautomer, •CH_2OH. This is likely the reason why only methylene hydroxyl radicals and no methoxy radicals were observed in early ESR experiments.[21,22] Carrying out the reaction in fully deuterated $C^2H_3O^2H$ should substantially inhibit any tunneling-mediated deuteron transfer chemistry, and should also facilitate observation of the deuterated methoxy radical C^2H_3O•.

Extending our calculations on alcohols first to ethanol and then to ethanediol, for ethanol one of three different protons might be abstracted by HO•, as shown in eq. 6.10, 6.11 and 6.12:

$$HO\bullet + CH_3CH_2OH \rightarrow \bullet CH_2CH_2OH + H_2O \tag{6.10}$$

$$HO\bullet + CH_3CH_2OH \rightarrow CH_3CH_2O\bullet + H_2O \tag{6.11}$$

$$HO\bullet + CH_3CH_2OH \rightarrow CH_3\bullet CHOH + H_2O \tag{6.12}$$

As expected from the above arguments, the largest reaction enthalpy gives the most stable free radical species with the free radical centered on the carbon adjacent to the oxygen atom (eq. 6.12). The next most stable product is the oxygen based radical (eq. 6.11) and the least stable is predicted to be the free radical centered on the external carbon (eq. 6.10) (Table 6.2).

For ethanediol two different types of proton can be abstracted to form water (eq. 6.13, 6.14):

$$HOCH_2CH_2OH + \bullet OH \rightarrow HOCH_2CH_2O\bullet + H_2O \quad (6.13)$$

$$HOCH_2CH_2OH + \bullet OH \rightarrow HOCH_2\bullet CHOH + H_2O \quad (6.14)$$

As before the reaction yielding the carbon-centered radical is more exothermic, in this case by some 39.5 $kJ \cdot mol^{-1}$. In the case of ethanediol, however, elimination of two waters is possible to give the vinyloxy radical or the acetyl radical (eq. 6.15, 6.16):

$$HOCH_2CH_2OH + \bullet OH \rightarrow \bullet CH_2CHO + 2H_2O \quad (6.15)$$

$$HOCH_2CH_2OH + \bullet OH \rightarrow CH_3\bullet CO + 2H_2O \quad (6.16)$$

Here the most exothermic reaction is that forming the acetyl radical ($CH_3\bullet CO$, eq. 6.16, Table 6.2), which is stabilized through spin delocalization over the C=O double bond, with substantial computed spin density on both C and O.

Finally, in this section we examine the effects of hydroxyl radical on ether based cryoprotectants, dimethylether (CH_3OCH_3) and a polyethylene glycol. For the latter we use the trimeric PEG $HO(C_2H_4O)_3H$, (2-[2-(2-hydroxyethoxy)ethoxy]ethanol) as a computationally tractable model:

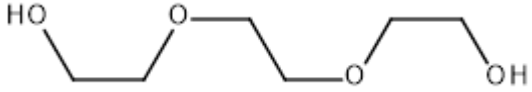

Since we seek to model the behavior of larger PEGs such as PEG 400 $HO(C_2H_4O)_9H$ we limit our calculations to abstraction of protons from a central carbon as these outnumber the hydroxyl protons eighteen to one in PEG 400.

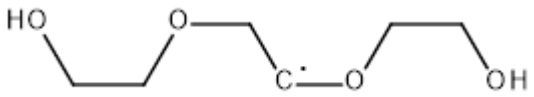

These reactions can be expressed in eq. 6.17 and 6.18:

$$CH_3OCH_3 + \bullet OH \rightarrow CH_3O\bullet CH_2 + H_2O \quad (6.17)$$

$$HO(C_2H_4O)_3H + \bullet OH \rightarrow HOC_2H_4OCH_2\bullet CHOC_2H_4OH + H_2O \quad (6.18)$$

Both are exothermic with enthalpy changes close to 100 kJ·mol–1 (Table 6.2).

6.8.4 Photoexcitation of Cryoprotectants

In many practical cases a substantial fraction of a real experimental sample will be cryoprotectant. Thus, with X-ray absorption spectroscopy, it is usual to add 15-50% v./v. of glycerol in aqueous media to prevent ice crystal formation. In protein crystallography it is normal practice to either have cryoprotectant added to the crystallization mother liquor, or to move crystals to cryoprotectant-containing media so that water in the crystal becomes replaced by cryoprotectant. Either way, a substantial fraction of cryoprotectant is present in samples prior to freezing in order to prevent damage to the soft and delicate protein crystals. Cryoprotectants such as alcohols and ethers will, like water, show initial photoexcitation through absorption of a photon by an electron, creating a highly excited radical cation and a solvated electron e^-_{solv} (eq. 6.19).

$$CH_3OH + h\nu \rightarrow CH_3OH^+ + e^-_{solv} \quad (6.19)$$

Just as the enthalpy change of the analogous reaction with water cannot be calculated without a valid DFT model of the solvated electron, the enthalpy changes involved in this reaction likewise cannot be simply computed. Also, similarly to the water case, the highly excited CH_3OH^+ 17-electron radical cation species will be able to decay by Auger electron emission to form the 16-electron CH_3OH^{2+}, releasing an electron, or by fluorescence to form a less excited CH_3OH^+ species. Our computations of CH_3OH^+ assume that this species is the least-excited ground state entity that is computed from DFT geometry optimizations. A number of reactions can be considered, either with additional methanol or with water (eq. 6.20-23).

$$CH_3OH^+ + CH_3OH \rightarrow CH_3OH_2^+ + CH_3O\bullet \quad (6.20)$$

$$CH_3OH^+ + CH_3OH \rightarrow CH_3OH_2^+ + \bullet CH_2OH \quad (6.21)$$

$$CH_3OH^+ + H_2O \rightarrow H_3O^+ + CH_3O\bullet \quad (6.22)$$

$$CH_3OH^+ + H_2O \rightarrow H_3O^+ + \bullet CH_2OH \quad (6.23)$$

The enthalpy changes computed for these reactions are shown in Table 6.2. Abstraction of a proton from CH_3OH^+ by methanol to form $CH_3OH_2^+$ plus methoxy or methylene hydroxyl free radicals, is predicted to be exothermic with an enthalpy change of –19 and –48 $kJ \cdot mol^{-1}$. One unexpected result is that eq. 6.22 and 6.23 are predicted to be endothermic reactions by +42 and +12 $kJ \cdot mol^{-1}$, respectively, and we predict that these reactions are unlikely to occur.

Table 6.2: Computed reaction enthalpies for selected reactions discussed in the text

Reaction	ΔE (kJ·mol^{-1})	Equation / notes
4	–87.56	$H_2O^+ + H_2O \rightarrow [H_3O]^+ + HO\bullet$
5	–304.06	$HO\bullet + HO\bullet \rightarrow H_2O_2$
6	–105.72	$HO\bullet + CH_3OH \rightarrow \bullet CH_2OH + H_2O$
7	–76.45	$HO\bullet + CH_3OH \rightarrow CH_3O\bullet + H_2O$
10	–67.27	$HO\bullet + CH_3CH_2OH \rightarrow \bullet CH_2CH_2OH + H_2O$
11	–87.75	$HO\bullet + CH_3CH_2OH \rightarrow CH_3CH_2O\bullet + H_2O$
12	–112.62	$HO\bullet + CH_3CH_2OH \rightarrow CH_3\bullet CHOH + H_2O$
13	–73.71	$HOCH_2CH_2OH + \bullet OH \rightarrow HOCH_2CH_2O\bullet + H_2O$
14	–113.19	$HOCH_2CH_2OH + \bullet OH \rightarrow HOCH_2\bullet CHOH + H_2O$
15	–102.88	$HOCH_2CH_2OH + \bullet OH \rightarrow \bullet CH_2CHO + 2H_2O$
16	–129.00	$HOCH_2CH_2OH + \bullet OH \rightarrow CH_3\bullet CO + 2H_2O$
17	–99.36	$CH_3OCH_3 + \bullet OH \rightarrow CH_3O\bullet CH_2 + H_2O$
18	–107.79	$HO(C_2H_4O)_3H + \bullet OH \rightarrow HOC_2H_4OCH_2\bullet CHOC_2H_4OH + H_2O$
20	–18.83	$CH_3OH^+ + CH_3OH \rightarrow CH_3OH_2^+ + CH_3O\bullet$
21	–48.09	$CH_3OH^+ + CH_3OH \rightarrow CH_3OH_2^+ + \bullet CH_2OH$
22	+41.52	$CH_3OH^+ + H_2O \rightarrow H_3O^+ + CH_3O\bullet$
23	+12.25	$CH_3OH^+ + H_2O \rightarrow H_3O^+ + \bullet CH_2OH$

6.8.5 Direct interactions with proteins and protein photoexcitation.

Finally, we turn to a consideration of the free radicals of proteins. In most protein samples, for examples, crystals, the fraction of protein is considerable, and can outweigh that of water. The amino acid side chains are various and many of these can form stable free radicals. For example, tyrosine and tryptophan form stable free radicals that have long been understood,[24, 25] and stable sulfur free radicals can be created by everyday processes such as cutting fingernails.[26] The calculation of free radical chemistry with all 20 common amino acid side chains presents a quite formidable challenge, and one that is unlikely to yield substantial returns in terms of our understanding the radiation chemistry of protein solutions. We will therefore focus on the polypeptide backbone, and for the sake of simplicity we once again turn to a small, computationally tractable model for our calculations; that of glycylglycine, the simplest peptide.

We first consider the relative stabilities of free radicals created by abstraction of a Cα proton with those created by abstraction of a NH proton from the peptide bond:

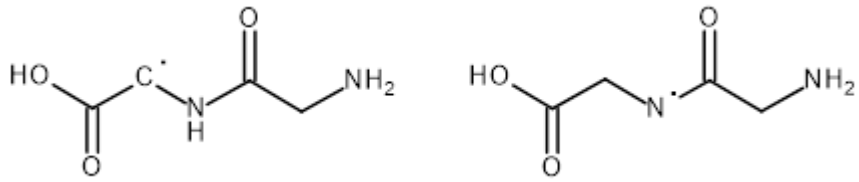

Geometry optimization gives computed energies of the free radicals considered, showing that the Cα based radical is predicted to be more stable by 113.93 $kJ \cdot mol^{-1}$, with a planar structure and highly delocalized spin density extending over both nearby carbonyl groups that explains the relative stability of this species.

DFT calculations of the excited state entity [glycylglycine]+ gave structures with spin density localized on the N-terminal of the dipeptide, which we considered to be less accurate as a model of a real protein, because there is only one such nitrogen per peptide. To better model the radical cationic excited state we therefore replaced the terminal amino with a methyl group to give glycl-N-propionate ester, $HO_2CCH_2NHCOC_2H_5$:

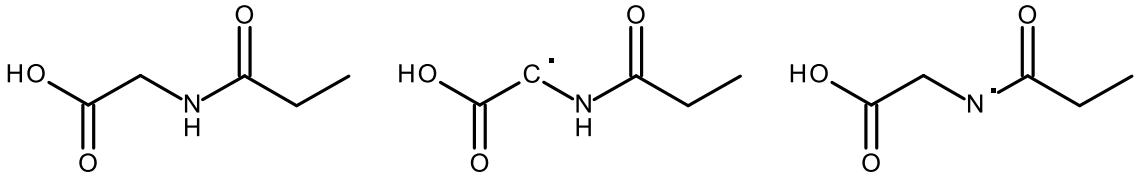

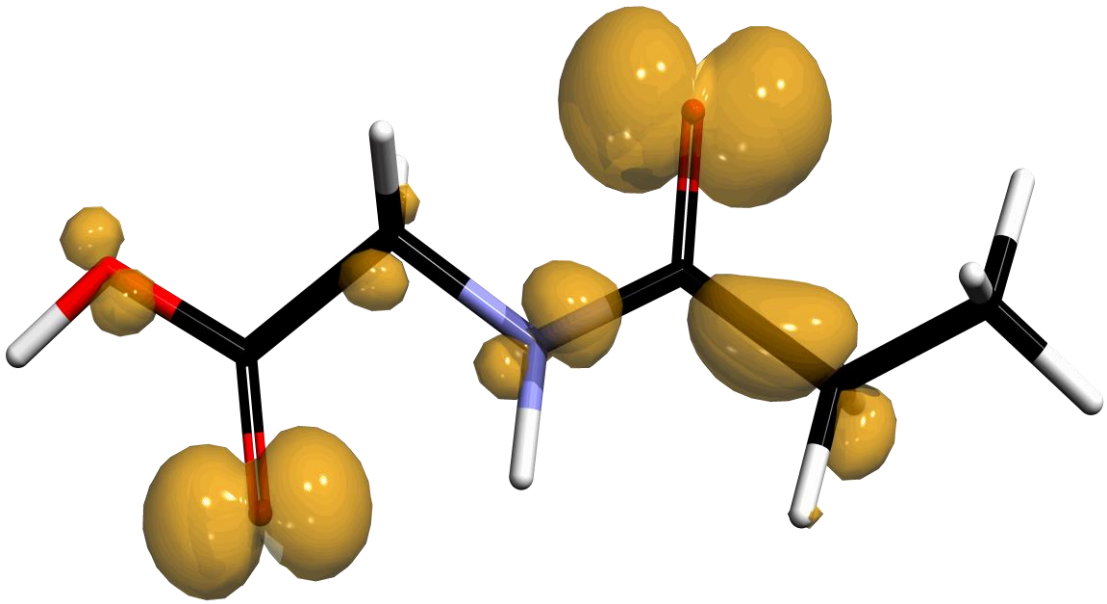

Figure 6.4: Spin density isosurface for the glycl-N-propionate ester radical cation. The spin density isosurface is mapped at 0.03 spins/a.u.^{3} and shows extensive spin delocalization over the peptide bond central to the molecule.

As expected, the carbon and nitrogen centered radicals of this species gave relative energies that were similar to that for glyclglycine, with the carbon centered radical predicted to be more stable by 112.78 kJ·mol^{-1}. We next used the glycl-N-propionate ester as a small molecule analogue to model the photoexcited cationic state that might be generated by the action of ionizing radiation on a peptide backbone. We find that the radical cation of glycl-N-propionate ester $HO_2CCH_2NHCOC_2H_5^+$ shows considerable delocalization of the spin density over the peptide portion of the molecule, with a corresponding high level of stabilization. Figure 6.4 shows the spin density iso-surface of $HO_2CCH_2NHCOC_2H_5^+$. Computations for larger peptide fragments are time consuming, but we computed geometry optimizations for cyclo-hexa-glycine,[27] which in the crystal structure shows hydrogen-bonding between C=O and H–N of stacked cyclo-hexa-glycine molecules in the unit cell, but computationally an isolated ring folds to form a short stretch of a hydrogen bonded structure resembling a tilted antiparallel β–sheet structure. In this case the spin density for the radical cation is also extensively delocalized and the isosurface needed to be mapped at very low spin densities for visualization (not illustrated).

Because of the stability of the peptide radical cation, the computed reactions with H_2O abstracting a proton are extremely endothermic and are most unlikely to occur. The predicted structures of the photoexcited cation and neutral ground state are shown superimposed in Figure 6.5. The structures can be seen to be very similar, and this can be quantified using the Hodgkin index,[28] specified by eq. 6.24, where ρ is the property being considered, such as atomic position or computed charge, and in which the integration is over all space:

$$H_{AB} = 2\frac{\int \rho_A \rho_B \, dv}{\int \rho_A^2 dv + \int \rho_B^2 dv} \tag{6.24}$$

Hodgkin indices range from +1 to –1, with +1 indicating a perfect match, and –1 the worst possible match (e.g. H–F superimposed on F–H would have a Hodgkin index of –1). In our case if we neglect charges then a Hodgkin index of 0.997 is obtained, if Muliken partial fitted charges from a DFT population analysis calculation are included for each atom, then the Hodgkin index of 0.424 is obtained due to the cationic nature of the photoionized species.

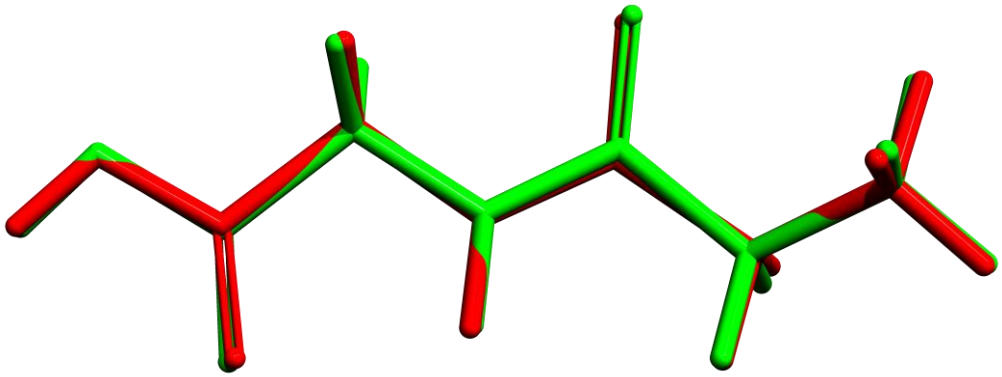

Figure 6.5: Superposition of the geometry optimized structure for glycl-N-propionate ester (green) and the corresponding radical cation (red), showing a high degree of predicted structural similarity for the two species.

Preliminary calculations of even longer photoexcited peptide chains indicates that the spin density is even more delocalized with spin densities ranging across all peptide bonds included (Figure 6.4) which would mean that the Hodgkin index would improve with longer peptide chains. These results may suggest that this stability is responsible for the success of protein crystallography in resisting photodamage. Given the potential for photodamage to delicate structures from photo-absorption of ionizing X-ray radiation, and the doses of radiation that are typically used in a modern crystallography experiment using synchrotron radiation, which can be as high as 10 MGy, it is perhaps surprising that severe damage to physical structures is not observed. Our calculations predict that radical cations arising from photoexcitation of the peptide chain will be stabilized by delocalization along the peptide bonds of polypeptides present, and it seems plausible that this stability is responsible for the success of modern X-ray crystallographic methods as applied to protein crystals.

6.8.6 Mobility of solvated electrons and hydroxyl radicals

As previously discussed, the solvated electron can be challenging to model computationally. Here, for simplicity, we restrict our considerations to water. Current models of the hydrated electron e^-_{aq} include a cluster of approximately six water molecules associated with the electron via hydrogens (Figure 6.6). Both the nature of the local solvation environment and the dynamics of e^-_{aq} in water are well-studied yet remain incompletely understood.[15–**Error! Bookmark not defined.**] The e^-_{aq} are in nature highly mobile entities; the surrounding protons shown in Figure 6.6 will set up a potential barrier but λ_{th} for electrons is of the order of 90 Å at 77 K (eq. 6.8), and quantum mechanical tunneling will be a highly effective means of electron translocation; with *a priori P* values that are some 20 orders of magnitude greater than for proton tunneling (eq. 6.9), limited primarily by rearrangement of the water molecules to form an appropriate encapsulating cavity. Figure 6.7 shows preliminary DFT calculations of e^-_{aq} in water using a

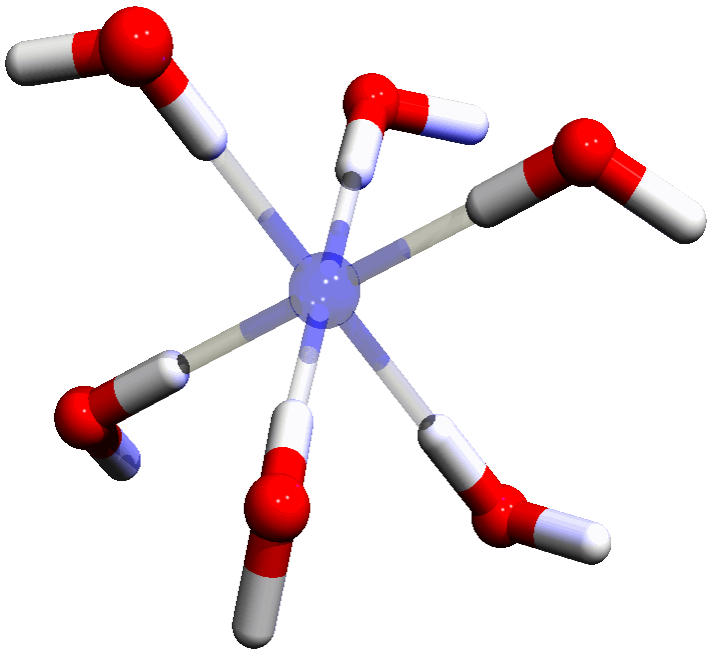

Figure 6.6: A currently accepted[15–**Error! Bookmark not defined.**] computational model of the hydrated electron e^-_{aq}, a diffuse cavity-like entity encapsulated by six water molecules (in this example). The electron (blue transparent sphere) is modelled as being located centrally by weak noncovalent bonds.

cluster of six water molecules. In agreement with the work of others, the structure can be seen to be a cavity containing substantial electron spin density, with water protons pointing inward and an oxygen-oxygen distance of 3.33 Å. Approximating the structure of water as that of ice (which is slightly less dense) this compares with an oxygen-oxygen inter-nuclear distance of 2.75 Å, and the movement of waters involved in moving the hydrated electron spin cavity from one location in an ice matrix to another will add up to a combined movement of more 2 Å . We can also subtract the total energy for $[H_2O]_6$ and that for $[H_2O]_6 - e^-_{aq}$ to compute an approximate minimum energy for e^-_{aq} which is 118.53 kJ·mol^{-1}.

Hydroxyl radicals are also expected to be highly mobile, even in frozen matrix because a minimum of nuclear motion is required with effective electron motion:

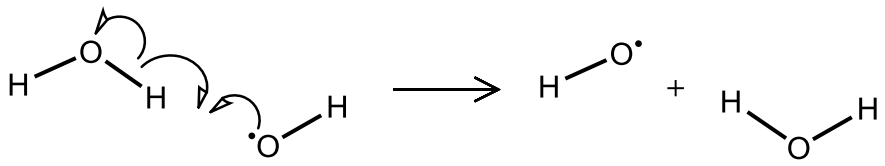

Using DFT to model this chemistry we can calculate the effective energy barrier for this reaction to be 15.12 kJ·mol^{-1}, with reactants and products being isoenergetic. Moreover, the nuclear motion in this reaction is particularly small; the proton being transferred between •OH and H_2O needs to move only 0.48 Å, and the external protons move by only 0.16 Å, because the O–H bond-length differs between •OH and H_2O. We can therefore anticipate a very fast reaction that shows substantially enhanced rates due to quantum mechanical tunneling. In this manner oxidizing equivalents could propagate along hydrogen bonded chains of water molecules in solution very rapidly indeed, and we can anticipate that this would hold true, even at very low temperatures.

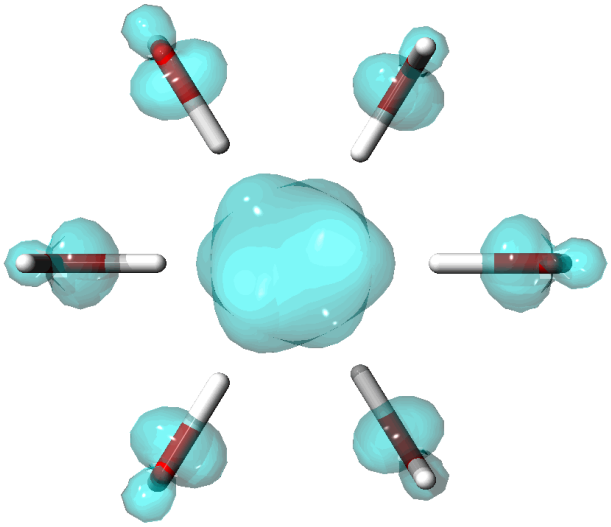

Figure 6.7: A preliminary computational model of the hydrated electron e^-_{aq}, showing a 0.03 spins per cubic a.u. spin density isosurface, indicating the diffuse cavity-like entity expected from previous work. This calculation assumed D_{3h} symmetry. Other symmetries gave similar energy minima.

Indeed, if current models of the hydrated electron e^-_{aq} (Figure 6.6) are accurate, the nuclear motion involved in moving e^-_{aq} from one site to another will be considerably greater than that required for moving •OH, and of the two entities the latter is thus expected to be very much more mobile. Hence, in a real sample, •OH could very rapidly translocate by propagation of electrons through the water hydrogen bonding network to cryoprotectant molecules, where it might react to form the products discussed section 6.8.3, leaving the hydrated electrons trapped in the ice matrix to relatively slowly reduce any redox active components of the system.

6.9 Conclusions

A computational chemistry approach to examining mechanisms of photoexcitation and cryoprotectant hydroxyl radical scavenging was employed, with specific focus on photodamage. Products of the photoexcitation of water reacting with methanol were found to give rise to predominantly a carbon-centered methylene radical over the methoxy radical, in good agreement with experimental ESR observations, due to a partial double-bond between the carbon and oxygen. The calculated activation energy between the methylene hydroxyl radical and the methoxy radical, combined with quantum tunneling considerations, and the overnumerousness of the C-H protons to O-H protons, may finally explain those early ESR observations and preference of the formation of the methylene hydroxyl radical.

Our methodology can also be used to predict likely photochemical products of direct interactions with cryoprotectants. We note that reactions with CH_3OH^+ and water forming H_3O^+ and either CH_3O• or •CH_2OH are endothermic, and thus not likely to occur. However, all of the other modelled hydroxyl radical reactions with cryoprotectants were exothermic, some markedly so. This indicates a likely and rapid progression of photochemical reactions in solutions containing these cryoprotectants once these radical species are formed. Such radical formation is obviously concerning to research being carried out on samples containing cryoprotectants that are exposed to such ionizing radiation.

Calculations were also made on models of peptides and specifically peptide backbones. The radicals formed are diffused in spin density across the nearby carbonyl groups as expected. The overall stability of the peptide backbone radical could be an indication of the overall success of protein crystallography in the context of modern X-ray techniques.

A final consideration was made regarding the mobility of solvated electrons and hydroxyl radicals. Both of these species are highly reactive, even in a cryogenic environment. The results of this study indicate extremely fast reaction rates, due to the small activation barriers and quantum tunneling effects of the solvated electrons. Hydroxyl radicals are also mobile in a frozen matrix. The total distance of proton movement is less than half an Angstrom, and due to the bond length differences between •OH and H_2O, a movement of 0.16 Å is required. Coupled with the quantum mechanical tunneling, the minute amount of movement leads to very fast reaction times. Indeed, it is the conclusion of this work that hydroxyl radicals can propagate rapidly through electrons via hydrogen bonding in real samples. This would leave the hydrated electrons free to reduce any redox reactive species in the sample.

Presented here is an examination of the radiation chemistry of water, the reaction of cryoprotectants with the products of that chemistry, and the radiation chemistry of those cryoprotectants directly. We use the radical cation H_2O^+ as a model for solvated electrons, in addition to the hydroxyl radical, to show the effects of photodamage on samples subjected to modern X-ray techniques. It is clear that as synchrotron sources of X-rays continue to increase in brightness, the need to take photodamage into account when analyzing data is of paramount importance.

6.10 Future Work

The highly reactive nature of the solvated electrons and hydroxyl radicals, described here with computational chemistry, requires a considered approach to future X-ray experiments. In addition, the cryoprotectants chosen for modern X-ray experimentation, be it spectroscopic or crystallographic, must be used with caution. In future, it may be possible to avoid some of the deleterious effects of water photoionization. Using the techniques outlined here, it may be possible to model radical scavenging by other compounds. It may also be possible to further explain the enhanced rate of photoreduction observed as described.

REFERENCES

1) Becquerel, H. J. On the Rays Emitted by Phosphorescence. *Compt. Rend. Acad. Sciences*, **1896**, *122*, 420–421.

2) Curie, M.; P. Curie, Bemont. G. On a New, strongly radio-active substance contained in pitchblende. *Compt. Rend. Acad. Sciences*, **1898**, *127*, 1215–1217.

3) Cooper, R. The History and development of radiation chemistry. *Aust. J. Chem.* **2011**, *64*, 864–868.

4) Weik, M.; Ravelli, R. B. G.; Kryger, G.; McSweeney, S.; Raves, M. L.; Harel, M. Gros, P.; Silman, I.; Kroon, J.; Sussman, J. L. Specific chemical and structural damage to proteins produced by synchrotron radiation. *Proc. Natl. Acad. Sci. USA*. **2000**, 97, 623–628.

5) George, G. N.; Pickering, I. J.; Pushie, M. J.; Nienaber, K.; Hackett, M. J.; Ascone, I.; Hedman, B.; Hodgson, K. O.; Aitken, J. B.; Levina, A.; Glover, C.; Lay, P. A. X-ray induced photo-chemistry and X-ray absorption spectroscopy of biological aamples. *J. Synchrotron Radiat*. **2012**, *19*, 875–886.

6) Nienaber, K. H., Pushie, M. J., Cotelesage, J. J. H., Pickering, I. J., George, G. N. Cryoprotectants severely exacerbate X-ray induced photoreduction. *J. Phys. Chem. Lett.*, **2018**, *9*, 540–544.

7) Jonah, C. D. A short history of the radiation chemistry of water. *Radiat. Res*. **1995**, *144* (2), 141–147.

8) Delley, B. An All-Electron Numerical Method for Solving the Local Density Functional for Polyatomic Molecules. *J. Chem. Phys*. **1990**, *92*, 508–517.

9) Klamt, A.; Schüürmann, G. COSMO: A New approach to dielectric screening in solvents with explicit expressions for the screening energy and its gradient. *J. Chem. Soc., Perkin Trans.* **1993**, *2*, 799–805.

10) Shavitt, I. Geometry and singlet-triplet energy gap in methylene: A critical review of experimental and theoretical determinations. *Tetrahedron*, **1985**, *41* (8), 1531–1542.

11) Bermudez, C.; Bailleux, S.; Cherncharo, J. Laboratory detection of the rotational-tunneling spectrum of the hydroxymethyl radical, CH_2OH. *Astron. Astrophys*. **2017**, 598–606.

12) Buxton, G. V.; Greenstock, C. L.; Helman, W. P.; Ross, A. B. Critical review of rate constants for reactions of hydrated electrons, hydrogen atoms and hydroxyl radicals (·OH/·O–) in aqueous solution. *J. Phys. Chem. Ref. Data*, **1988**, *17*, 513–886.
13) Garrett, B. C.; Dixon, D. A.; Camaioni, D. M.; Chipman, D. M.; Johnson, M. A.; Jonah, C. D.; Kimmel, G. A.; Miller, J. H.; Rescigno, T. N.; Rossky, P. J. Role of Water in Electron-Initiated Processes and Radical Chemistry: *Iss. Sci. Adv. Chem. Rev*. **2005**, *105*, 355–390.
14) George, G. N. personal communication
15) Kevan, L. Solvated electron structure in glassy matrixes. *Acc. Chem. Res*. **1981**, *14*, 138–145.
16) Hameka, H. F.; Robinson, G. W.; Marsden, C. J. Structure of the hydrated electron. *J. Phys. Chem.* **1987**, *91*, 3150–3157.
17) Ehrler, O. T.; Neumark, D. M. Dynamics of electron solvation in molecular clusters. *Acc. Chem. Res*. **2009**, *42* (6), 769–777.
18) Young, R. M.; Neumark, D. M. Dynamics of solvated electrons in clusters. *Chem. Rev.* **2012**, *112* (11), 5553–5577.
19) László, Turi. Hydrated electrons in water clusters: inside or outside, cavity or noncavity? *J. Chem. Theo. Comp.* **2015**, *11* (4), 1745–1755.
20) J. A. Walker and D.M. Bartels. A Simple ab initio model for the solvated electron in methanol. *J. of Phys. Chem. A.* **2016**, *120* (36), 7240–7247.
21) Gibson, J. F.; Symons, M. C. R.; Townsend, M. G. Unstable Intermediates. Part II. Photolysis of hydrogen peroxide in solid alcohols: some reactions of hydroxyl radicals. *J. Chem. Soc*. **1959**, 269–276.
22) Blandamer, M. J.; Shields, L.; Symons, M. C. R. Unstable intermediates. Part XXVIII. Solvated electrons: rigid organic solvents. *J. Chem. Soc*. **1965**, 1127–1131.
23) Allemann R. K.; Scrutton N. S. Quantum tunnelling in enzyme-catalysed reactions. *Ed. Roy. Soc. Chem.*, Cambridge, UK. **2009**.
24) Prince, R. C. Tyrosine radicals. *Trends Biochem. Sci.* **1988**, *13*, 286–287.

25) Prince, R.C.; George, G.N. Tryptophan radicals. *Trends Biochem. Sci.* **1990**, *15*, 170–172.
26) Chandra, H.; Symons, M. C. R. Sulfur Radicals Formed by Cutting α-Keratin. *Nature,* **1987**, *328*, 833–834.
27) Karle I. L.; Karle, J. An application of a new phase determination procedure to the structure of cyclo(hexaglycyl)demihydrate. *Acta Cryst.* **1963**, *16*, 969–975.
28) Hodgkin, E. E.; W.G. Richards, W. G. Molecular similarity based on electrostatic potential and electric field. *Intl. J. Quant. Chem.: Quant. Biol. Symp.* **1987**, *14*, 105–110.

7. Effects of Mg^{2+} on X-ray Induced Photo-reduction of Metal Ions in Aqueous Solutions

7.1 Preface

Results from experiments described in Chapter 6 established the correlation between alcohol based cryoprotectants and X-ray induced photoreduction. Following up on computational experiments described in the literature, experimental research was carried out to determine the effect of addition sources of electrons, specifically Auger electrons, to examine any additional photoreduction. Concurrent to these experiments, research was published suggesting Auger electrons from Mg^{2+} would increase the rate of photoreduction. Experiments were then carried out examining magnesium contributions in addition to arsenic from cacodylate buffer, a common macromolecular crystallographic buffer.

7.2 Manuscript Author Contributions

Effects of Mg^{2+} on X-ray induced photoreduction of metal ions in aqueous solution. Kurt H. Nienaber, Susan Nehzati, Julien J. H. Cotelesage, Ingrid J. Pickering, and Graham N. George.

Kurt Nienaber took primary responsibility for experimental design, data analysis, and manuscript drafting. Susan Nehzati and Julien Cotelesage took responsibility for assisting in experimental design and data collection. Ingrid Pickering took responsibility for assisting in experimental design and manuscript editing. Graham George took responsibility for assisting in experimental design, data analysis, and manuscript drafting.

7.3 Acknowledgements

Work carried out at the University of Saskatchewan was supported by the Natural Sciences and Engineering Research Council of Canada, with other support from Canada Research Chairs (I.J.P and G.N.G.) and the Saskatchewan Health Research Foundation (SHRF). KHN was funded by the Gene Expression Mapping using Synchrotron Light group grant from the Saskatchewan Health Research Foundation (Nichol, group leader) and SN acknowledges the Dr. Rui Feng Scholarship. KHN and SN were Fellows in the Canadian Institutes of Health

Research-Training grant in Health Research Using Synchrotron Techniques (THRUST). Portions of this research were carried out at the Stanford Synchrotron Radiation Lightsource, a Directorate of SLAC National Accelerator Laboratory and an Office of Science User Facility operated for the U.S. Department of Energy Office of Science by Stanford University. The SSRL Structural Molecular Biology Program is supported by the DOE Office of Biological and Environmental Research, and by the National Institutes of Health, National Center for Research Resources, Biomedical Technology Program (P41RR001209).

7.4 Abstract

Photochemical damage arising from the use of synchrotron sources has become increasingly more problematic as photon fluxes have increased. Adding to the problem, photoreduction is exacerbated by the use of common cryoprotectants, as we recently reported. Further computational analyses suggested the exacerbation of photochemistry via Auger electron emission from magnesium in samples. Here we report experimental photoreduction data of copper samples containing added magnesium or arsenic. The effects of magnesium on photoreduction of metals in solution are examined via X-ray absorption spectroscopy. We report here a decrease, not increase, with the addition of magnesium to cryoprotectant containing copper samples, in contrast to previous reports indicating there would be an increase in the rate of photoreduction.

7.5 Introduction

Approximately 11% of all proteins contain at least one redox-active transition metal ion.[1,2] These transition metal ions generally play key roles in the biological function of these proteins, which catalyze many of the most chemically challenging and biologically essential reactions carried out by living organisms. Relating metalloenzyme active site structure to catalytic function is a cornerstone of the field of inorganic biochemistry, and structural information plays a key role in this process. Radiation chemistry is a mature and well-established field, and its importance in relation to X-ray crystallography and X-ray spectroscopy, especially with regard to X-ray induced photoreduction of redox-active transition metal ions, is increasingly being realized.[3,4] In many cases, reported X-ray

crystal structures of initially oxidized enzyme crystals are actually of enzymes that contain metal active sites that have become photoreduced during crystallographic data acquisition. For example, for the molybdenum enzyme sulfite oxidase almost all reported crystal structures are of photoreduced enzyme,[5-7] with the only *bona-fide* oxidized structures being site-directed mutants[7] that are very difficult to reduce.[8] Moreover, the assumption that photoreduced sites correspond to a physiologically relevant reduced form is not necessarily valid, because in some cases the structures of photoreduced metal sites can differ from the structures of chemically reduced species. Thus, we have previously reported that chemically reduced copper-bound prion peptide has a linear-digonal Cu^{+} geometry, but Cu^{+} deriving from photoreduction of Cu^{2+} has a trigonal-planar type geometry.[9] Recently, we reported that addition of alcohol- and ether-based cryoprotectants increases the rate of photoreduction of Cu^{2+} in a model system by more than an order of magnitude.[4] This observation can be explained by considering the known radiochemistry of these solutions.[4] Photolysis of water very rapidly yields hydroxyl radicals (•OH) and hydrated electrons (e_{aq}^{-}), which can subsequently recombine to reform water and heat, or can react with other components in solution. The observed increase in rate of photoreduction arises from the fact that alcohol and ether cryoprotectants are highly effective hydroxyl radical scavengers, leaving an excess of highly-reducing hydrated electrons which are then available to reduce other redox-active species in the frozen solution.[4]

Stumpf *et al.*[10] have recently suggested another mechanism by which photochemical modification of metal sites in proteins might be exacerbated. Biological samples frequently contain species such as Mg^{2+} which possess X-ray absorption edges that are below the energy of the incident X-ray beam, and hence will become excited. Stumpf *et al.* have used computational methods to study the consequences of this for a model $[Mg(OH_2)_6]^{2+}$ system, representing solvated Mg^{2+}.[10] The core-hole created by K-edge X-ray absorption will decay either by release of X-ray fluorescence, or by emission of Auger electrons. In the soft X-ray regime, the latter mechanism predominates, creating an Mg^{4+} state. Stumpf *et al.* predict that this should decay by a complex chain of very rapid relaxation steps involving both intra- and intermolecular processes, ending with the metal in its original Mg^{2+} state. They also predict

that after Mg K-shell X-ray absorption has occurred the immediate environment of the magnesium would have large concentrations of radicals and slow electrons.[10]

While this work provided a theoretical foundation for potential problems deriving from the presence of species such as Mg^{2+}, experimental evidence for or against these effects has yet to be offered. In the present work we use our previously employed photoreduction kinetic experimental model[4] to investigate the effects of dissolved Mg^{2+} on the kinetics of photoreduction of Cu^{2+}. We also examine the effects of cacodylic acid, an arsenic-containing buffer that has been used for approximately 5% of the structures in the protein data bank,[11] as the L-edge absorption energies of arsenic are very similar to the K-edge of magnesium, and the Auger electron yield is somewhat higher.[12]

7.6 Materials and Methods

7.6.1 Sample Preparation

All reagents were purchased from Sigma-Aldrich (Oakville, ON) and were of the highest quality available. Solution samples were prepared by dissolving anhydrous $CuCl_2$ in deionized water and loading into 2 mm path-length poly-acetal cuvettes closed with a mylar tape window and were frozen by immersion into a partly-frozen isopentane slurry with a temperature of approximately 120 K. Samples were transported and stored at liquid nitrogen temperatures until data acquisition.

7.6.2 X-ray Absorption Spectroscopy

XAS measurements were carried out at the Stanford Synchrotron Radiation Lightsource (SSRL) using the structural molecular biology XAS beam line 7-3 with the SPEAR3 storage ring containing 500 mA at 3.0 GeV. 7-3 is equipped with a Si(220) double crystal monochromator, and harmonic rejection was accomplished by detuning the second monochromator crystal to 60% of peak intensity. Incident and transmitted X-rays were monitored using nitrogen-filled gas ionization chambers employing a sweeping voltage of 1,600 V, and X-ray absorption was measured as the Cu K_α X-ray fluorescence excitation spectrum using an array of 30 germanium detectors[13] (Canberra Ltd. Meriden, CT, USA) equipped with nickel filters to preferentially reject scattered radiation in order to maintain the

detector in a non-saturating count-rate regime, together with silver Soller slits (EXAFS Co., Pioche Nevada) to reject filter fluorescence. XAS data were collected using the XAS Collect data acquisition software,[14] and samples were maintained at a temperature of 10 K using a helium flow cryostat (Oxford instruments, Abingdon, UK). Data reduction and analysis employed the EXAFSPAK suite of computer programs (http://ssrl.slac.stanford.edu/exafspak.html) and was carried out as previously described.[15]

7.7 Kinetic Experiments

X-ray spectroscopic acquisition to explore photoreduction kinetics used an essentially identical procedure to that previously described.[4] In brief, a scan rate was selected that was sufficiently more rapid than the rate of observed changes and giving adequate signal to noise, with sufficient data range for normalization and background removal. The time of each scan was taken to be the time stamp of the point at the onset of the structured region of the near-edge spectrum (at ~8983 eV) which was ~1.0 min. after the sequence of scans were started. Each individual scan took a total of 5.43 min. from the time stamp of the first point to the time stamp of the first point of the subsequent scan. Time series spectra were fit to a linear combination of the two end members, specifically the first sweep of the glycerol series, corresponding to a nearly pure Cu^{2+} spectrum, and the last sweep of the plus glycerol series corresponding to a nearly pure photoreduced Cu^{+} species, by non-linear optimization to the simple pseudo first-order kinetics; $[Cu^{2+}]/[Cu] = e^{-k_{eff}t}$, where k_{eff} is the pseudo first-order rate constant and t is time.

7.8 Results and Discussion

Figure 7.1 shows progression of photoreduction of 2 mM Cu^{2+} in the presence of 50 mM Mg^{2+} added as MgF_2 in the presence of 25% v/v glycerol. The progressive changes in the spectra are similar to those previously described,[4] and are indicative of photoreduction of Cu^{2+} to Cu^{+} in the frozen solution. We have previously shown that X-ray induced photoreduction in our model system behaves with simple pseudo-first order kinetics, and that the effective rate constant is directly proportional to the photon flux density at the sample. For the new experiments reported here our flux density was 2.38×10^{11} photons·s^{-1}·mm^{-2},

whereas previously it was nearly double this value, at 4.57×10^{11} photons·s^{-1}·mm^{-2}.[4] This is because our previous work was conducted with the monochromator fully tuned and using a rhodium-coated vertically collimating mirror pitched to reject harmonics, whereas with the work reported here the monochromator was detuned and the mirror absent from the beam path.[4] By accounting for the loss of incident photons, we are able to show a rate of photoreduction nearly identical to that previously reported for identical samples with a rate of 5.6 hr^{-1} compared to 5.7 hr^{-1} in our previous experiments.[4]

The kinetic parameters are summarized in Table 7.1. Allowing for the different flux densities, the observed pseudo-first order rate constants are quantitatively consistent with our previous studies for samples prepared in the absence of Mg^{2+}. With 2mM $CuCl_2$ and water alone, a relatively low rate of photoreduction Cu^{2+}, k_{eff}= 0.54 hr^{-1}, is observed. As found previously,[4] a ten-fold increase in rate is observed when glycerol is added. Because the Mg K-edge and the As L-edge are very close in energy (1303 and 1324 eV, respectively), and because salts of cacodylic acid, containing penta-valent arsenic as $[(CH_3)_2AsO_2]^-$ or dimethylarsinate, are commonly used as buffers in crystallographic experiments, we examined the effects of adding both magnesium as MgF_2, and arsenic as cacodylate, to copper to examine their effects on the rate of Cu photoreduction. The effects that any slow electrons deriving from Auger emission should also be slightly more pronounced for arsenic than magnesium, because the arsenic L-edge electron yield is slightly higher than that for the magnesium K-edge.[12] According to Stumpf *et al.*[10] the presence of Mg^{2+} should increase the rate of photoreductive reactions.

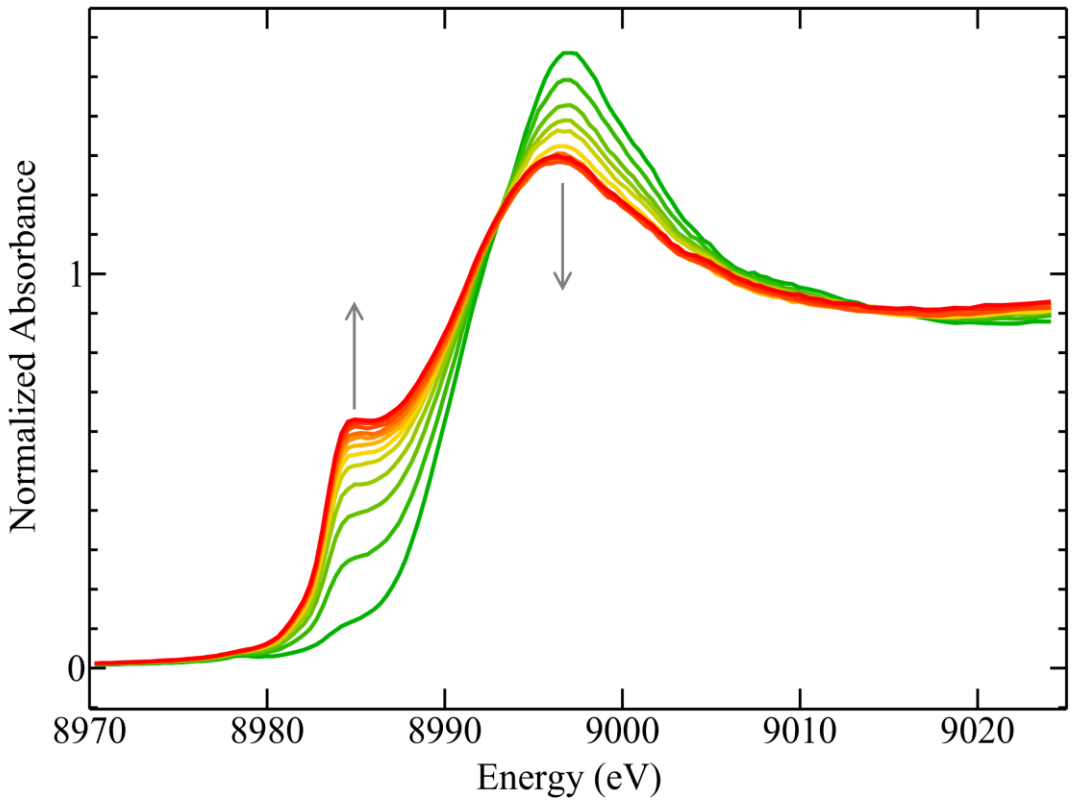

Figure 7.1 Time-series of X-ray absorption near-edge spectra showing cumulative changes with time in the frozen aqueous solution due to photoreduction from the initial Cu^{2+}(green) to Cu^{+}(red). The sample initially contained 2 mM Cu^{2+} added in the form of $CuCl_2$ plus 50 mM MgF_2 and 25% v/v glycerol. Arrows indicate the progression of changes with increasing exposure to X-rays.

Table 7.1. Kinetics of Cu(II) photoreduction in aqueous solution[a]

Sample	*% glycerol v/v*	k_{eff} (hr^{-1})
No additions	0	0.54(1)
50 mM MgF_2	0	0.085(2)
25 mM cacodylate	0	0.067(5)
No additions	25	5.60(2)
50 mM MgF_2	25	5.12(7)
25 mM cacodylate	25	5.34(4)

a. In these experiments the Cu^{2+} concentration was 2 mM, using $CuCl_2$, and the photon flux density was 2.38×10^{11} photons·s^{-1}·mm^{-2}

Initial experiments were conducted with 50 mM $MgCl_2$ as the source of magnesium. The copper near edge of the XAS experiments showed changes consistent with chlorine binding. We observe that excess chlorine is capable binding copper in solution and affecting the rate of photoreduction. As shown in Figure 7.2, samples containing 2 mM $CuCl_2$ are alike to those containing CuF_2, indicating full dissociation of chlorine from copper. Those samples containing 50 mM and 100 mM Cl show changes attributed to the copper recombining with aqueous chlorine. We also note an increase in the rate of photoreduction associated with chlorine binding to copper (data not shown).

Due to the complication of chlorine binding to the aqueous copper, an effort was made to eliminate as much chlorine as possible. Thus, $MgCl_2$ was replaced with MgF_2 for analysis of Mg as a source of extra electrons exacerbating photoreduction. By replacing $MgCl_2$ with MgF_2, we were able to isolate the effects of excess electrons originating from magnesium and avoid the complications of chlorine binding and the effects on the rate of photoreduction from said Cl binding to copper.

We observe that the rate of photoreduction of aqueous Cu^{2+} is not substantially increased by addition of 50 mM MgF_2. Moreover, we observe that the rate of photoreduction is substantially lower in the presence of both Mg and cacodylate buffer so that $k_{eff} = 0.085$ hr^{-1} and 0.067 hr^{-1} respectively. As we have previously reported, addition of glycerol also increases the rate of photoreduction substantially, with 25% v/v giving rise to an effective rate constant 5.6 hr^{-1}.

Magnesium K-edge photoexcitation will give a very short-lived formal Mg^{3+} state with a 1s core hole, with a lifetime of ~0.9 fs,[16] and Auger emission a number of different Mg^{4+} states,[10] all of which are expected to decay by throwing off water ligands as excited H_2O^+. The energetic photoelectrons and Auger electrons will be a source of reductive chemistry, whereas the H_2O^+ radical cations are expected to react with water to form hydroxonium cations and oxidizing hydroxyl radicals.[17]

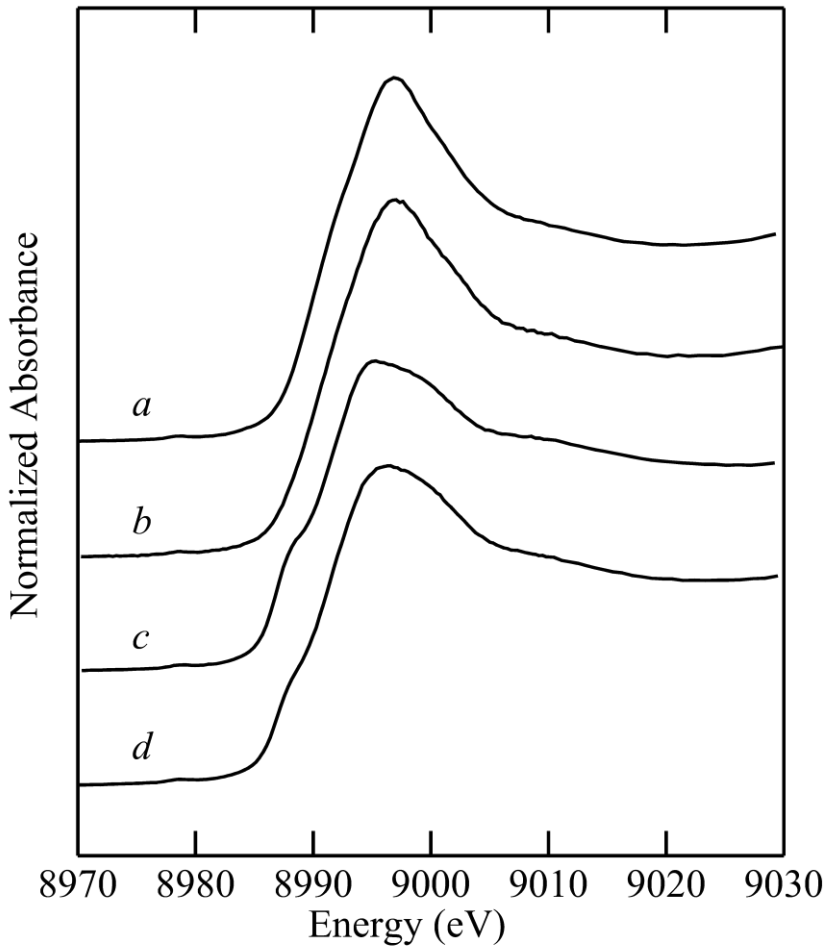

Figure 7.2 Near edge spectra of a) 2 mM $CuCl_2$, b) 2 mM CuF_2, c) 2 mM $CuCl_2$ + 100 mM LiCl and d) 2 mM $CuCl_2$ + 50 mM $MgCl_2$. The copper spectra shown in a) and b) indicate dissociated hexaquo copper. The spectra in c) and d) show chlorine dissociated from the LiCl and $MgCl_2$ binding to copper.

$$H_2O^+ + H_2O \rightarrow H_3O^+ + OH\bullet \quad (7.1)$$

The scavenging of oxidizing hydroxyl radicals by glycerol will leave a reductive excess,[4] and thus enhance the observed photoreduction of Cu^{2+} to Cu^+. According to the mechanism proposed by Stumpf [10], the primary decay pathways for photoexcited Mg^{2+} proceed through Mg^{3+} and form, via Auger electron emission, Mg^{4+}. We also note this hypervalent Mg^{4+} state will lead to an increase in excited H_20^+ molecules. As noted in Equation 7.1, these excited water molecules can recombine with water to form hydroxonium ions and hydroxyl radicals, the latter of which will be oxidizing in solution.

The proposed mechanism of extra electrons involves the generation of water ligands as excited H_2O^+ molecules. For a hexaquo Mg molecule, the bound waters may be excited and propagate out from the metal centres. For the case of cacodylic acid, there are no bound waters for the photoelectrons to excite and generate photoexcited progeny from. The lack of bound water molecules makes cacodylic acid less prone to propagating Auger electrons as described by Stumpf [10]. The mobility of H_2O^+ ions may also limit the ability of Auger electrons to influence the observed rate of photoreduction in these experiments.

We note that the levels of Mg^{2+} that we have used in the present work are substantially higher than those that would be present in samples of a biological molecule, as prepared for an X-ray crystallography experiment, which would normally contain an effective concentration of 1-5 mM, depending upon how large the crystallographic unit cell is. On face value, this would indicate that issues with Mg^{2+} will be only minimal, because of the relatively low concentrations. Nevertheless, Mg^{2+} is frequently bound at a site of substantial interest, often in association with adenosine triphosphate (ATP), and given that it could give rise to foci of free radicals and local photodamage may be significant. Examination of the protein data bank indicates that some 16% of X-ray crystal structures contain magnesium.

7.9 Conclusions

The evidence presented here suggests that the addition of Mg^{2+} to solution will not lead to an increase in photoreduction of copper samples via Auger electron emission. This is in contrast to previous reports stating that the emission of electrons from Mg^{2+} would lead to photochemical changes in samples with both magnesium and redox active metals.[10] To the contrary, our data indicate a decrease in the rate of copper photoreduction in the absence of hydroxyl radical scavenging by cryoprotectants. The slower rate of copper photoreduction observed with magnesium, in the absence of cryoprotectants, is found to be 6 to 8 times slower than that of $CuCl_2$ in water. Thus, we conclude that magnesium added as a source of extra electrons will lower the rate of copper photoreduction, not increase it.

Experimental data presented here also indicates that chlorine will also contribute to the phenomenon of photoreduction. While MgF_2 showed no increase in the rate of photoreduction in copper samples with glycerol, the addition of $MgCl_2$ nearly doubled the rate of photoreduction. The presence of Mg in both samples further illustrates that magnesium alone is not contributing to photoreduction via Auger electron emission, contrasting with previous reports. However, chlorine binding to copper will change the redox potential, and thus alter the kinetics of photoreduction. The evidence here also shows that arsenic present in cacodylate, possessing L-edge absorption energies similar to Mg K-edge, does not contribute to photochemistry.

REFERENCES

1) Cotelesage, J. J. H.; Pushie, M. J.; Grochulski, P.; Pickering, I. J.; George, G. N. Metalloprotein active site structure determination: Synergy between X-ray absorption spectroscopy and X-ray crystallography. *J. Inorg. Biochem*. **2012**, *115*, 127–137.

2) Pushie, M. J.; Cotelesage, J. J. H., George, G. N. Molybdenum and tungsten oxygen transferases – structural and functional diversity within a common active site motif" *Metallomics*, **2014**, *6*, 15–24.

3) George, G. N.; Pickering, I. J.; Pushie, M. J.; Nienaber, K.; Hackett, M. J.; Ascone, I.; Hedman, B.; Hodgson, K. O.; Aitken, J. B.; Levina, A.; Glover, C.; Lay, P. A. X-ray induced photo-chemistry and X-ray absorption spectroscopy of biological samples. *J. Synchrotron Radiat.* **2012**, *19*, 875–886.

4) Nienaber, K. H.; Pushie, M. J.; Cotelesage, J. J. H.; Pickering, I. J.; George, G. N. Cryoprotectants severely exacerbate X-ray induced photoreduction, *J. Phys. Chem. Lett.* **2018**, *9*, 540–544.

5) Pushie, M. J.; George, G. N. Spectroscopic studies of molybdenum and tungsten enzymes. *Coord. Chem. Rev.* **2011**, *255*, 1055–1084.

6) George, G. N.; Pickering, I. J.; Kisker, C. X-ray absorption spectroscopy of chicken sulfite oxidase crystals. *Inorg. Chem.* **1999**, *38*, 2539–2540.

7) Qiu, J. A.; Wilson, H. L.; Pushie, M. J.; Kisker, C.; George, G. N.; Rajagopalan, K.V. The structures of the C185S and C185A mutants of sulfite oxidase reveal rearrangement of the active site. *Biochemistry*, **2010**, *49*, 3989–4000.

8) George, G. N.; Garret, R. M.; Prince, R. C.; Rajagopalan, K. V. Coordination chemistry at the molybdenum site of sulfite oxidase: Redox-induced structural changes in the cysteine 207 to serine mutant. *Inorg. Chem*. **2004**, *43*, 8456–8460.

9) McDonald, A.; Pushie, M. J.; Millhauser, G. L.; George, G. N. New insights into metal interactions with the prion protein: EXAFS analysis and structure calculations of copper binding to a single octarepeat from the prion protein. *J. Phys. Chem. B.* **2013**, *117*, 13822–13841.

10) Stumpf, V.; Gokhberg, K.; Cederbaum, L. S. The role of metal ions in X-ray-induced photochemistry. *Nature Chem*. **2016**, *8*, 237–241.
11) Berman, H. M.; Westbrook, J.; Feng, Z.; Gilliland, G.; Bhat, T. N.; Weissig, H.; Shindyalov, I. N.; Bourne, P. E. The protein data bank. *Nucl. Acid. Res*., **2000**, *28*, 235–242.
12) Krause, M. O. Atomic radiative and radiationless yields for K and L shells. *J. Phys. Chem. Ref. Data*, **1979**, *8*, 307–327.
13) Cramer, S. P.; Tench, O.; Yocum, M.; George, G. N. A 13-element Ge detector for fluorescence EXAFS. *Nucl. Instr. Meth. A*. **1988**, *266*, 586–591.
14) George, M. J. XAS-Collect: A Computer program for X-ray absorption spectroscopic data acquisition *J. Synchrotron Radiat*. **2000**, *7*, 283–286.
15) George, G. N.; Garrett, R. M.; Prince, R. C.; Rajagopalan, K. V. The molybdenum site of sulfite oxidase: A comparison of wild-type and the cysteine 207 to serine mutant using X-ray absorption spectroscopy. *J. Am. Chem. Soc*. **1996**, *118*, 8588–8592.
16) Krause, M. O.; Oliver, J. H. Natural widths of atomic K and L levels, Kα X-ray lines and several KLL Auger lines. *J. Phys. Chem. Ref. Data*, **1979**, *8*, 329–338.
17) Garrett, B. C.; Dixon, D. A.; Camaioni, D. M.; Chipman, D. M.; Johnson, M. A.; Jonah, C. D.; Kimmel, G. A.; Miller, J. H.; Rescigno, T. N.; Rossky, P. J.; Xantheas, S. S.; Colson, S. D.; Laufer, A. H.; Ray, D.; Barbara, P. F.; Bartels, D. M.; Becker, K. H.; Bowen, K. H. Jr.; Bradforth, S. E.; Carmichael, I.; Coe, J. V.; Corrales, L. R.; Cowin, J. P.; Dupuis, M.; Eisenthal, K. B.; Franz, J. A.; Gutowski, M. S.; Jordan, K. D.; Kay, B. D.; LaVerne, J. A.; Lymar, S. V.; Madey, T. E.; McCurdy, W.; Meisel, D.; Mukamel, S.; Nilsson, A. R.; Orlando, T. M.; Petrik, N. G.; Pimblott, S. M.; Rustad, J. R.; Schenter, G. K.; Singer, S. J.; Tokmakoff, A.; Wang, L.S.; Wittig, C.; Zwier, T. S. Role of water in electron-initiated processes and radical chemistry: Issues and scientific advances. *Chem. Rev*. **2005**, *105*, 355–389.

8. Protective Effects of Ketone Groups on X-ray Induced Photoreduction

8.1 Preface

Having clearly established that cryoprotectants exacerbate photoreduction in samples containing redox active metal ions, described in Chapter 4 and Chapter 5, experiments were carried out to examine other contributing factors to this phenomenon. Work with sources of extra electrons, specifically magnesium and arsenic, showed a decrease, not increase, in the rate of photoreduction of copper in the absence of cryoprotectants, as described in Chapter 7. Based on literature reports of ketone functional groups protecting against free radical damage, a series of experiments was designed to examine the rate of photoreduction of copper in the presence of ketones.

8.2 Manuscript Author Contributions

Kurt H. Nienaber, Ingrid J. Pickering, and Graham N. George. Protective Effects of Ketone Groups on X-ray Induced Photoreduction.

Kurt Nienaber took primary responsibility for experimental design, data analysis, and initial manuscript drafting. Ingrid Pickering took responsibility for assisting in manuscript editing and experimental consultation. Graham George took responsibility for assisting in experimental design, data analysis, and final preparation of the manuscript.

8.3 Acknowledgements

Research at the University of Saskatchewan is supported by a grant from the Chevron Energy Technology Company, the Natural Sciences and Engineering Research Council (GNG, IJP), the University of Saskatchewan and by Canada Research Chairs (GNG, IJP). Use of the Stanford Synchrotron Radiation Lightsource, SLAC National Accelerator Laboratory, is supported by the U.S. Department of Energy, Office of Science, Office of Basic Energy Sciences under Contract No. DE-AC02-76SF00515. The SSRL Structural Molecular Biology Program is supported by the DOE Office of Biological and Environmental Research, and by the National Institutes of Health, National Institute of General Medical Sciences (including P41GM103393). The contents of this publication are solely the responsibility of the authors and do not necessarily represent the official views of NIGMS or NIH.

8.4 Abstract

As modern beamlines have produced increased flux densities a corresponding increase in photochemistry can be observed in both X-ray absorption spectroscopy and macromolecular crystallography experiments. We have demonstrated previously that there is a direct correlation between increased flux density and the rate of photoreduction in copper samples. This photoreduction was further exacerbated by the presence of common cryoprotectants like glycerol and polyethylene glycol, with the alcohol and ether groups acting as hydroxyl radical scavengers leaving hydrated electrons to reduce the metal centres in the samples. Ketone groups have been reported to scavenge hydrated electrons and were thus examined to determine if their presence can mitigate the photoreduction being exacerbated by hydroxyl radical scavengers. Here we report the inclusion of acetone and benzoquinone to XAS samples as being successful in reducing cryoprotectant exacerbated photoreduction.

8.5 Introduction

Structural methods employing X-rays have proved essential for developing our understanding of the structure of metal-containing active sites in a range of complex biological molecules.[1,2] Modern synchrotron radiation sources, which provide X-ray beams of ever increasing brilliance, have revolutionized studies using the methods of macromolecular crystallography (MX) and X-ray absorption spectroscopy (XAS). However, the availability of ever smaller X-ray beams, enabling studies of ever smaller samples, means that problems with X-ray induced photochemistry are an increasing concern. X-ray induced photoreduction can change metalloprotein active site structures, and in some cases the only structural information available is that from photo-reduced samples. X-rays can cause scission of chemical bonds, with the concomitant formation of free radical species. Thus, X-ray irradiation ($h\nu$) of water in aqueous samples causes photoionization with liberation of hydrated electrons e_{aq}^- and formation of the H_2O^+ radical cation:

$$H_2O + h\nu \rightarrow H_2O^+ + e_{aq}^- \qquad 8.1$$

The H_2O^+ radical cation breaks down through scission of an H–O bond to liberate a proton (H^+) which, combines with water to produce hydroxonium ions, and hydroxyl radicals (•OH):

$$H_2O^+ + H_2O \rightarrow H_3O^+ + \bullet OH \qquad 8.2$$

Hydrated electrons are highly potent reductants, and hydroxyl radicals are strongly oxidizing. These species can recombine in effectively the reverse of reactions 8.1 and 8.2 to yield water and heat, which is thought to be a predominant reaction.[3,4] In previous work.[5] we have shown that cryoprotectants such as alcohols and ethers effectively prevent this recombination by scavenging hydroxyl radicals, leaving a surfeit of hydrated electrons, and consequently increasing the rate of photoreduction of reducible transition metal ions, such as Cu^{2+}.[6]

In the present work we investigate the effects of scavengers of hydrated electrons, and whether their presence can mitigate the exacerbation of photoreduction caused by the presence of hydroxyl radical scavengers. Early work has shown that organic compounds containing ketone functionalities are highly effective at scavenging hydrated electrons e_{aq}^-. In particular, acetone has been termed "an excellent scavenger for hydrated electrons"[7].

8.6 Materials and Methods

Reagents were purchased from Sigma-Aldrich (Oakville, ON) and were of the highest quality available. Anhydrous CuCl2 was dissolved in water with and without 25% v/v glycerol. 25% v/v acetone and benzoquinone were then added to separate copper samples with and without glycerol. Control samples containing 2 mM CuCl2 and 25% glycerol were also prepared to compare to previously established photoreduction rates. Samples were loaded into 2 mm path-length poly-acetal cuvettes closed with a mylar tape window. All samples were then frozen in a partly-frozen isopentane slurry with a temperature of approximately 120 K. Samples were transported and stored at liquid nitrogen temperatures until data acquisition.

Cu K-edge XAS measurements were carried out at the Stanford Synchrotron Radiation Lightsource (SSRL) using the structural molecular biology XAS beam line 7-3. Beamline 7-3 is designed for biological samples and the energy range most utilized is problematic for photoreduction. Harmonic rejection was accomplished by setting the mirror pitch to give an energy cutoff of 12 keV. Incident and transmitted X-rays were monitored using nitrogen-filled gas ionization chambers employing a sweeping voltage of 1,600 V, and X-ray absorption was measured as the primary fluorescence excitation spectrum using an array of 30 germanium detectors[8].

8.7 Results and Discussion

The results of kinetic analysis are given in Table 8.1. The results of the kinetic experiments were as expected, with the acetone and benzoquinone completely abrogating any photoreduction. As shown, the rate of photoreduction is unchanged when glycerol is added to the acetone containing sample. The rate of photoreduction for the benzoquinone sample is similar to the acetone sample and the rates may be considered unchanged within error when glycerol is added.

The rate of photoreduction in the control samples was also observed to be consistent with previous works.[7] It is noted that the rate of photoreduction was observed to decrease to a level below that previously observed in samples containing only copper and water with no additional glycerol. This demonstrates the ability of ketones to mitigate photoreduction and that photons alone are capable of producing photodamage in aqueous samples.

Density functional theory calculations give insights into the nature of the interactions. Addition of one electron (a hydrated electron) to acetone gives rise to the radical anion through $[(CH_3)_2CO]^{\bullet -}$ this species is stabilized by spin delocalization over the carbonyl group, as shown in Figure 8.1.

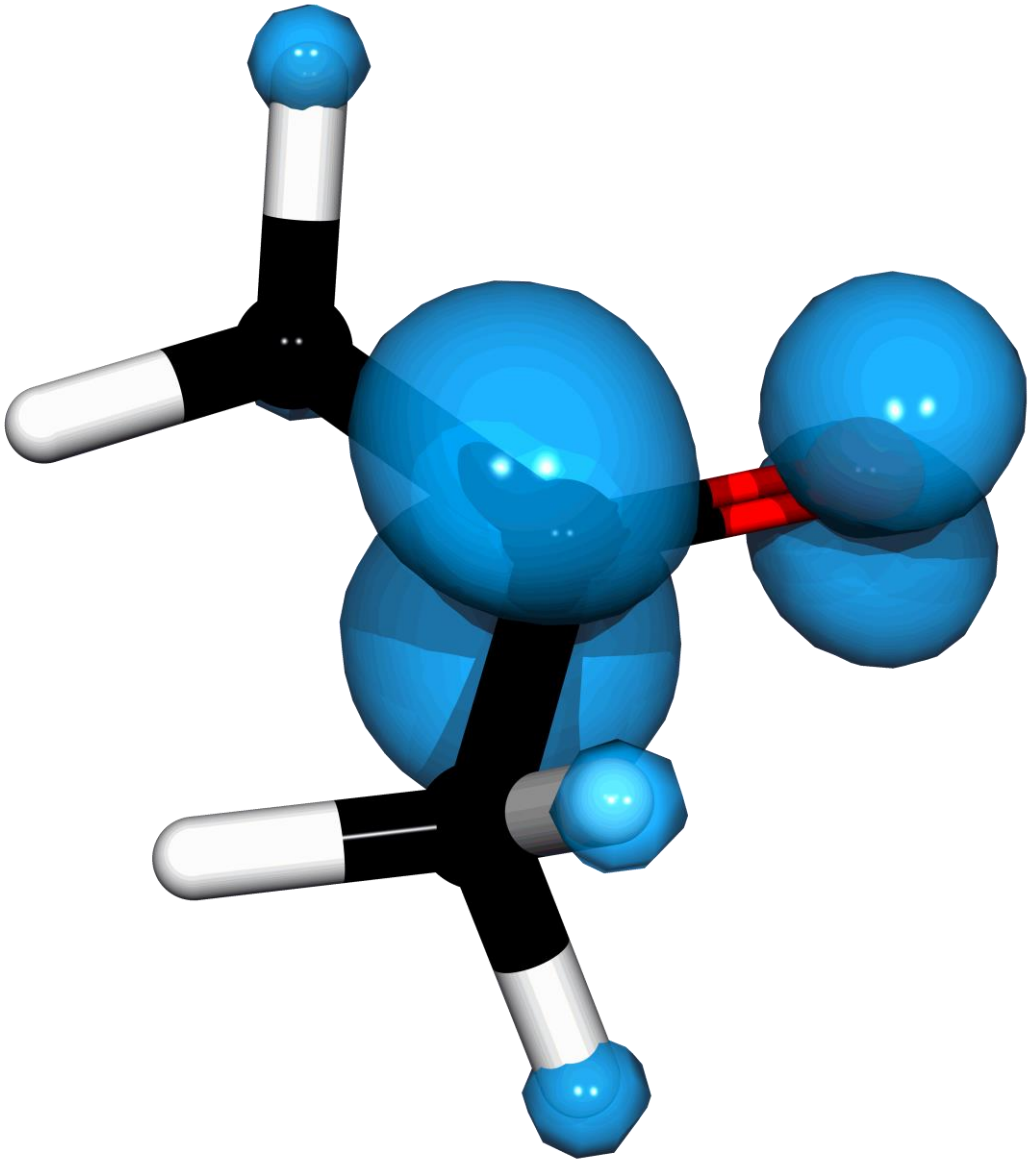

Figure 8.1 Spin density isosurface of the acetone radical anion. The spin density isosurface is mapped at 0.05 spins/a.u.^{3} and shows extensive spin delocalization over the ketone functional group.

Table 8.1. Kinetics of Cu(II) photoreduction in aqueous solutions with ketones[a]

Sample	*% glycerol v/v*	k_{eff} (hr^{-1})
No additions	0	0.54(1)
25 mM acetone	0	0.027(6)
25 mM benzoquinone	0	0.028(5)
No additions	25	5.60(2)
25 mM acetone	25	0.028(7)
25 mM benzoquinone	25	0.028(2)

In these experiments the Cu(II) concentration was 2 mM, using $CuCl_2$, and the photon flux density was 2.02×10^{11} photons$\cdot s^{-1} \cdot mm^{-2}$

Although much less of a problem than photoreduction, X-ray induced photooxidation can also be observed. For example, aqueous solutions of arsenite in the absence of glycerol can be oxidized to arsenate. Just as alcohols and ethers serve to promote photoreduction we anticipate that ketones would serve to exacerbate such photooxidiation. Moreover, just as ketones mitigate the exacerbation of photoreduction caused by glycerol, such glycerol and other hydroxyl radical scavengers are expected to mitigate any exacerbation in photooxidation rate caused by ketones or other hydrated electron scavengers. These effects will be examined in future work.

REFERENCES

1) Grossweiner, L. I.; Usui, Y. The role of the hydrated electron in photoreduction of cystine in the presence of indole. *J. Photochem. Photob.*, **1970**, *11*(1), 53–56.

2) Kisker, C.; Schindelin, H.; Pacheco, A.; Rajagopalan, K. V.; Enemark, J. H.; Rees, D. C. Molecular basis of sulfite oxidase deficiency from the structure of sulfite oxidase. *Cell*. **1997**, *91*(7), 973–983.

3) Kevan, L. Solvated electron structure in glassy matrixes. *Acc. Chem. Res.*, **1981**, *14*(5), 138–145.

4) Marsalek, O.; Uhlig, F.; VandeVondele, J. Jungwirth, P. Structure, dynamics, and reactivity of hydrate electrons by ab initio molecular dymnamics. *Acc. Chem. Res.*, **2012**, *45*(1), 23–32.

5) Nienaber, K. H.; Pushie, M. J.; Cotelesage, J. J. H.; Pickering, I. J.; George, G. N. Cryoprotectants remarkably exacerbate X-ray induced photoreduction. *J. Phys. Chem. Lett.*, **2018**, *9*, 540–544.

6) Nienaber K. H.; Nehzati, S.; Cotelesage, J. J. H.; Pickering, I. J; George, G. N. Effects of Mg^{2+} on X-ray induced photo-reduction of metal ions in aqueous solution. In publication

7) Riesz, P. The Radiolysis of acetone in air-free aqueous solutions. *J. Phys. Chem*., **1965**, *69*(4), 1366–1373.

8) Cramer, S. P.; Tench, O.; Yocum M.; George. G. N. A 13-element Ge Detector for Fluorescence EXAFS. *Nucl. Instr. Meth. A*, **1988**, *266*, 586–591.

9. Conclusions and Future Directions

9.1 Photoreduction Phenomenon

The most important finding of these works is that photoreduction is not only occurring with increased regularity in MX and XAS samples, but also it is being exacerbated many-fold by the simple cryoprotectants added to these samples to protect from cryogenic effects. It is industry standard in both crystallography and X-ray absorption spectroscopy to add PEG or glycerol primarily to remove water and prevent ice formation that may damage the sample or interfere with the actual data collection. The findings presented here show that the data must be carefully examined in any samples containing both these common cryoprotectants and redox active metals. The possibility of drawing erroneous conclusions from experiments where photoreduction is occurring and not being accounted for is high. These works show that research using both MX and XAS techniques is vulnerable to photoreduction and care must be taken when collecting data. To elucidate the mechanism of cryoprotectant involvement in photoreduction, samples were prepared with 2 mM $CuCl_2$ and 0 to 50% glycerol (v/v). And to understand the effect of copper concentration on the effective rate of photoreduction, samples were also prepared with 25% glycerol and 0.25 mM to 5 mM $CuCl_2$.

The results of this study demonstrate that a concentration of 25% glycerol is sufficient to mediate the photoreduction reaction and additional glycerol has no effect on rate of conversion as 50% glycerol shows a slower effective rate at 0.106(1) min^{-1} compared to 25% glycerol at 0.121(1) min^{-1} . A correlation with lower amounts of glycerol is observed as 10% glycerol resulted in a reduction in photoreduction with an effective rate constant of 0.081(1) min^{-1}. This indicates the glycerol mediation of photoreduction in the sample is dependent on glycerol concentration, but that there is an upper limit on how much glycerol can be introduced to a sample before the lack of water starts to inhibit free radical formation and thus limit photoreduction.

Modern beamlines have increasingly high flux densities, are capable of delivering more photons, and thus more flux density. The drive to produce new even brighter beamlines represents a major effort. For example, the newest synchrotron radiation source in North

America, NSLS-II, had construction costs exceeding $1.2B CAD, and can produce unprecedented flux densities. The APS upgrade is now approved and will be even more remarkable. Our findings that rates of photoreduction of Cu^{2+} to Cu^{+}, in the presence and absence of hydroxyl radical scavengers depended directly upon flux density are therefore particularly important. It is also of note that beamline upgrades typically increase the photons flux density, and that it is already impossible to collect Cu^{2+} data at some existing beamlines due to photoreduction. The findings presented here show that even on existing, lower flux density beamlines, cryoprotectant choice can also lead to the same problems as increased flux, and copper in particular is sensitive to being photoreduced, whether it is noticed by the researchers or not.[1]

During the course of our series experiments we sought to determine whether the sample changed in the absence of X-rays after an initial exposure. This might occur through mobilization of free radicals generated in the initial exposure within the frozen sample. We found no difference in the kinetics of continuously exposed samples and samples for which the beam had been shut off after an initial exposure, following restoration of the X-ray beam. This showed that detectible photoreduction did not occur from radicals generated in the initial X-ray exposure and that cryocooling was sufficient to prevent free radical movement in the sample.

9.2 Chelation Effects

EDTA was added to observe any effects of chelating the free copper in solution with and without glycerol present. A nearly 10 fold increase in photoreduction was observed when 25% glycerol was added to EDTA chelated copper over a sample containing EDTA, copper, and no glycerol. This finding demonstrates that even chelating the copper does not abrogate the effects of hydroxyl radical scavenger mediated photoreduction.

9.3 Ketone Functional Group Effects

Both acetone and benzoquinone showed the ability to negate the effect of glycerol on effective photoreductive rates. DMSO, a cryoprotectant, showed protection from

photoreduction, and even showed a slower rate of conversion than $CuCl_2$ alone. DMSO is capable of denaturing proteins and can cause the loss of iron-sulfur clusters for example.[2] The combination of these effects does not make DMSO particularly useful as a cryoprotectant but may aid in preventing photoreduction in samples where DMSO is the only solvent capable of dissolving the metal binding compound of interest (*e.g.* clioquinol, a copper chelating drug of interest in Alzheimer's research). DMSO is also more X-ray opaque than water, glycerol, PEG, or sucrose, which can make data collection more difficult.

9.4 Overall Conclusions

It is the conclusion of this work that the scavenging of hydroxyl radicals by organic alcohol groups in cryoprotectants or other sources exacerbates photoreduction. This novel finding has implications for both XAS and MX experiments alike. Photoreduction has already been observed without additional cryoprotectants, even under cryogenic temperatures, 80 - 85 K for protein crystallography, 10-12 K for X-ray absorption spectroscopy.[3] Cytochrome *c* peroxidase experiments show that Fe^{3+} can be reduced to Fe^{2+} in as little as 60 minutes of beam exposure.[4] Even engineering an enzyme to specifically avoid photolysis of a methyl-cobalt bond was insufficient to avoid photodamage during experimentation.[5] The photoreduction of free and protein bound B_{12} factors via X-rays is more fully discussed in the literature as well. [6] Any redox-active element in any sample that is exposed to X-rays and/or has a cryoprotectant added is more prone to be photoreduced due to this scavenging mechanism. The evidence for photoreduction occurring in X-ray experiments is clearly widespread in the literature, whether it is acknowledged or not.[1]

The implications of such rapid photoreduction are many; however, the most immediate is that photodamage is occurring and erroneous enzyme mechanisms are being proposed. Damage incurred on protein crystals at beamlines is known to occur but is often disregarded due to the short exposure times. Previous work has shown that photoreduction of iron in the active site of superoxide reductase follows pseudo-first order kinetics[7], in good agreement with the findings presented here.

The results of the photoreduction experiments presented here indicate that as little as four or five minutes of X-ray beam exposure on a SSRL 7-3, which has low to moderate X-ray flux density, are all that is necessary to substantially reduce redox active metals present in a sample. It is also very likely that many reported structures for metalloproteins may actually contain photoreduced metal sites, and erroneous conclusions about enzymatic reactions may have been drawn.

Using these works as a warning, it would benefit researchers in both fields of MX and XAS to limit their use of cryoprotectants where possible. In XAS, it is possible to freeze samples, as discussed in Section 5.7, using an isopentane slurry for rapid freezing that avoids most ice crystal formation, which can interfere with data collection. For MX experiments, the use of free radical scavengers, possibly biological in nature like α-tocopherol, in the cryoprotectant mixture may help ameliorate some of the photoreduction that can occur.

9.5 Future Work

Any further examination of copper and X-ray induced photoreduction should begin with a hexa-aquo copper complex, such as diethylenetriaminepentaacetic acid (DTPA). Chlorine from the $CuCl_2$ did not fully dissociate and thus influenced the rate of photoreduction of the central copper. In addition, chelation effects from the glycerol and PEG itself cannot be ruled out of having an affect on photoreduction.

Further photoreduction experiments may begin to look at other redox active metals, including iron and manganese, to examine other biologically important and prevalent cofactors. The work presented in this thesis has shown that photoreduction can be a problem for numerous experimental setups, including those containing metal ions that were previously believed to be exempt from photodamage like mercury. The addition of cryoprotectants to nearly every XAS and MX sample means exposure to the exacerbation of photoreduction by these compounds. It is important to carry on examination of these other redox active metal ions to ensure accurate structural information is being reported in the literature.

An effort should also be made to try to protect samples from the photoreductive effects of the cryoprotectants that have been examined in this thesis. The protective effects of ketone

groups have been examined in Chapter 8, but there may be reservations about exposing more delicate protein samples to compounds with these chemical properties. Future experiments should focus on free radical scavengers that may be more amenable to use in biological samples. The protective effects of ascorbic acid, α-tocopherol, beta-carotene, and cholecalciferol would be a good starting point for these investigations.

REFERENCES

1) Kisker, C.; Schindelin, H.; Pacheco, A.; Rajagopalan, K. V.; Enemark, J. H.; Rees, D. C.; Molecular basis of sulfite oxidase deficiency from the structure of sulfite oxidase. *Cell*, **1997**, *91*(7), 973–983.

2) Beinert, H.; Emptage, M. H.; Dreyer, J.; Scott, R. A.; Hahn, J. E.; Hodgson, J.; Thomson, J.A. Iron-sulfur stoichiometry and structure of iron-sulfur clusters in three-iron proteins: Evidence for [3Fe-4S] clusters. *Proc. Nat. Acad. Sci*., **1983**, *80*, 393–396.

3) George, G. N.; Pickering, I. J.; Kisker, C. X-ray absorption spectroscopy of chicken sulfite oxidase crystals. *Inorg. Chem.*, **1999**, *38*(10), 2539–2540.

4) Latimer, M. J.; Ito, K.; McPhillips, S. E.; Hedman, B. Integrate instrumentation for combined polarized single-crystal XAS and diffraction data acquisition for biological applications. *J. Synchrotron Rad.* **2005**, *12*(Pt 1), 23–27.

5) Datta, S.; Koutmos, M.; Pattridge, K.; Ludwig, M.; Matthews, R. A disulfide-stabilized conformer of methionine synthase reveals an unexpected role for the histidine ligand of the cobalamin cofactor. *Proc. Nat. Acad. Sci.* **2008**, *105*(11), 4115–4120.

6) Champloy, F.; Gruber, K.; Jogi, G.; Kratky, C. XAS spectroscopy reveals X-ray-induced photoreduction of free and protein-bound B12 cofactors. *J. Synchrotron Rad.* **2000**, *7*, 267–273.

7) Clay, M. D.; Jenney, F. E.; Hagedoorn, P. L.; George, G. N.; Adams, M. W.; Johnson, M. K. Spectroscopic studies of Pyrococcus furiosus superoxide reductace: implications for active-site structures and the catalytic mechanism. *J. Am. Chem. Soc.* **2002**, *124*, 788–805.